VALERIA FANTI

APPLICATION OF SNL-SWAN MODEL ON THE EFFECT OF WAVE FARMS IN THE WAVE PROPAGATION

UNIVERSIDADE DO ALGARVE
FACULTADE DE CIÊNCIAS E TECNOLOGIA
2019

VALERIA FANTI

APPLICATION OF SNL-SWAN MODEL ON THE EFFECT OF WAVE FARMS IN THE WAVE PROPAGATION

Master in Marine and Coastal Systems

Work performed under the supervision of:

Conceição Juana Fortes, Laboratório Nacional de Engenharia Civil

José Jacob, Universidade do Algarve

UNIVERSIDADE DO ALGARVE
FACULTADE DE CIÊNCIAS E TECNOLOGIA
2019

Application of SNL-SWAN model on the effect of wave farms in the wave propagation

Declaração de autoria de trabalho

Declaro ser o(a) autor(a) deste trabalho, que é original e inédito. Autores e trabalhos consultados estão devidamente citados no texto e constam da listagem de referências incluída.

Declaration of authorship of work

I declare to be the author of this work, which is original and unpublished. Authors and works consulted are duly cited in the text and are included in the list of references.

27th September 2019

Copyright

Table of Contents

Index of Figures

Index of Tables

Nomenclature

B-OF	Bottom-fixed Oscillating Flap
IEA	International Energy Agency
LCOE	Levelized Cost of Energy
OES	Ocean Energy System
OWC	Oscillating Water Column
OWSC	Oscillating Wave Surge Converters
RCW	Relative Capture Width
SWAN	Simulating WAves Nearshore
SNL	Sandia National Laboratories
SNL-SWAN	Sandia National Laboratories - Simulating WAves Nearshore
WAM	WAve Modelling
WEC	Wave Energy Converter

List of symbols

B	WEC characteristic dimension [m]
c	wave speed [m/s]
COV	coefficient of variation
CW	capture width [m]
c_x, c_y	propagation velocities in the geographical x-y space [m/s]
c_σ, c_θ	propagation velocities in the spectral space
Dir	mean wave direction [°]
$Dir\ diff$	wave direction percentage change [%]
E	energy spectral density [m^2s]
f	wave frequency [Hz]
$[f\_high]$	lowest frequencies [Hz]
$[f\_low]$	highest frequencies [Hz]
g	gravity acceleration [m/s^2]
h	water depth [m]
H_{inc}	incident wave height [m]
H_{lee}	lee wave height [m]
H_s	significant wave height [m]

$H_s\ diff$	significant wave height percentage change [%]
k	wave number
K_t	transmission coefficient
m_n	nth-order spectral moment
$[msc]$	number of frequencies
N	wave action density [s/m]
P	energy flux per wave front length [kW/m]
$P_{0,tot}$	power absorbed by a flap in power matrix [kW]
P_{abs}	absorbed wave power [kW]
P_{inc}	incident wave power [kW/m]
$P_{i,tot}$	power absorbed by the ith flap [kW]
$PkDir$	peak wave direction [°]
$P(t)$	power time series [kW/m]
q	WECs interaction factor
q_i^{mod}	modified q-factor
r	correlation coefficient
RCW	relative capture width
$RMSE$	root mean square error
s	standard deviation [kW/m]
S	wave spectrum
S_{bot}	wave-bottom interactions [kW/m^2]
S_{db}	depth-induced breaking [kW/m^2]
S_{dis}	dissipation source [kW/m^2]
SI	scatter index
S_{in}	wind-wave interactions source [kW/m^2]
S_{ln}	linear wind-input [kW/m^2]
S_{nl}	nonlinear wave-wave interactions [kW/m^2]
S_{tot}	total sources [kW/m^2]
S_{tr}	triad wave-wave interactions [kW/m^2]
t	time [s]
T_e	energy period [s]
T_{m01}	mean absolute wave period [s]
T_{m02}	mean absolute zero-crossing period [s]
$T_{m01}\ diff$	mean period percentage change [%]

T_p	peak period [s]
x, y	geographic coordinates [m]
X	measured value
Y	simulated value
Δf	wave frequency resolution [Hz]
θ	wave propagation direction [°]
λ	wavelength [m]
μ	mean power [kW/m]
ρ	water density [kg/m^3]
σ	relative frequency

Acknowledgments

This research was made possible by support from the National Laboratory of Civil Engineering (LNEC) of Lisbon. The information given by Prof. Taveira Pinto and Prof. Paulo Santos from FEUP are also acknowledged.

This work was made under the framework of the project OWC-Harbour - *Harbor Protection with dual chamber oscillating water column devices* and of the project To-SEAlert - Wave overtopping and flooding in coastal and port areas: Tools for an early warning, emergency planning and risk management system, Ref. PTDC/EAM-OCE/31207/2017.

Special thanks to Kelley Ruehl from the Sandia National Laboratories for removing the bug in the formulation of OBCASE 3 and 4 in SNL-SWAN and solving the issue suggested during the present work.

Dedication

I would first like to thank my supervisor Conceição Juana Fortes, my co-supervisor José Jacob and Eric Didier for all their support and help through the learning process of this master thesis. Thanks also to my Professor and Master course coordinator Óscar Ferreira from the University of Algarve for always being so availabile.

I dedicate this thesis to my family. To the enthusiasm of my mum, to the positivity of my dad, to the smile of my sister, to the strength of my grandparents. Thank you for always believing in me and being with me in the good and bad moments, nevertheless the distance.

A special thanks also to all the friends that this life gave me, to the ones I met in the water and those I met behind a school desk. Most of all, thanks to the dream team for all the laughs.

And thanks to Andrea, for making me discover the beauty of the waves, I wouldn’t be here without you.

Abstract

Wave farms are a promising way to harness wave power and produce clean energy, but it is important to develop better modelling tools to understand their impact on nearshore wave climate.

The main objective of the present work was to evaluate the effect of wave farms in the wave propagation along a coastline stretch of the Portuguese coast, by using numerical modelling. The exact study area was Almagreira beach in Peniche, north of Lisbon, a selected area for wave farms installation, where a WaveRoller oscillating wave surge converter was tested since 2007. The SNL-SWAN (Sandia National Laboratories, Simulating WAves Nearshore) numerical model was used since it is a third-generation spectral wind-wave propagation model that integrates into its algorithms the automatic calculation of the transmission coefficients of obstacles on the wave propagation given the device's power matrix or relative capture width curve.

First, a sensitivity analysis of the model was performed, then the wave transformation and propagation were analyzed in the presence of a different number (from 10 to 100) and positions of wave energy converters (WECs) for six selected most common and energetic incident wave conditions and for 19 years (from 2000 to 2018) of real sea states. A wave farm of 40 WaveRoller type of WECs was then compared with a wave farm of 40 Bombora's mWave pressure differential WECs.

As a result of the simulations, the differences in significant wave height, wave period and wave direction before and after the installation of the wave farms were identified. The percentage decrease in significant wave height resulted to be strictly related to the power matrix and the device with higher power absorption potential showed a greater impact in the lee of the wave farm.

Key-words: Wave energy extraction, renewable energy, wave farm, SNL-SWAN, numerical wave modelling, Peniche, WECs, WaveRoller, Bombora's mWave

Resumo

Os campos de conversores de energia das ondas representam uma forma promissora de aproveitar a energia das ondas e produzir energia de uma forma limpa, mas é de fundamental importância desenvolver ferramentas de modelação para entender melhor o seu impacto no clima de ondas nas regiões costeiras.

O principal objetivo do presente trabalho é avaliar o efeito de campos de conversores de energia das ondas na propagação de ondas ao longo de um trecho da costa portuguesa, usando modelação numérica. A área exata de estudo foi a praia de Almagreira, em Peniche, a norte de Lisboa, uma área selecionada para instalação de campos de conversores de energia das ondas, onde um Conversor Oscilante de Translação de Ondas WaveRoller foi testado desde 2007.

Utilizou-se o modelo numérico SNL-SWAN (Sandia National Laboratories, Simulating WAves Nearshore), que é um modelo espectral de terceira geração de propagação de ondas geradas pelo vento, que integra nos seus algoritmos o cálculo automático dos coeficientes de transmissão de obstáculos na propagação de ondas, dada a matriz de potência do dispositivo ou curva de largura de captura relativa. Primeiro, realizou-se uma análise de sensibilidade do modelo, depois analisou-se a transformação e a propagação das ondas em função do número (de 10 a 100) e das posições dos conversores de energia das ondas (Wave Energy Converters, WEC’s), usando uma seleção de seis condições de onda incidente mais comuns e energéticas, para 19 anos (de 2000 a 2018) de estados de mar realistas. Finalmente, fez-se uma comparação entre um campo de conversores de energia das ondas com 40 WEC’s, do tipo WaveRoller, e um campo de 40 WEC’s baseados na diferença de pressão, mWave, em Bombora.

Como resultado das simulações, foram identificadas as diferenças na altura significativa, período e direção das ondas antes e depois da instalação dos parques de ondas. A diminuição relativa da altura significativa das ondas mostrou estar estritamente relacionada com a matriz de potência e o dispositivo com maior potencial de absorção de energia mostrou um impacto maior na zona a sotamar do parque de ondas.

Palavras-chave: extração de energia das ondas, WECs, energia renovável, fazenda de ondas, SNL-SWAN, modelagem numérica de ondas, Peniche, WaveRoller, Bombora

Resumo alargado

O presente trabalho tem como objetivo aplicar o modelo de propagação de ondas SNL-SWAN na avaliação do impacto no litoral de um campo de conversores de energia das ondas (*wave energy converters, WECs*). O modelo SNL-SWAN permite a incorporação de características específicas do conversor, como a matriz de potência e a curva de largura de captura relativa. A região de estudo é a zona ao largo da praia da Almagreira, em Peniche (Portugal), que já é uma área de teste piloto para teste de protótipos de conversores

As condições de fronteira para as ondas no domínio do modelo foram determinadas a partir da base de dados do Centro Europeu de Previsões do Tempo a Médio Prazo *(European Centre for Medium-Range Weather Forecasts, ECMWF*), para um período de 9 anos (2010-2019). Os resultados das simulações do modelo SWAN com um domínio de três malhas encaixadas foram validados com dados *in situ* provenientes da bóia Nazaré Costeira. As estatísticas de desempenho do modelo calculadas mostraram uma boa concordância entre os dados do modelo e os dados medidos.

Depois da validação do modelo, realizou-se uma caracterização das ondas e da potência das ondas. O modelo SNL-WAN foi executado para um período de 19 anos (2010-2018) de dados do ECMWF, para obter o regime de ondas na região ao largo da praia da Almagreira. A partir dessa caracterização, foram identificados seis estados de mar mais comuns e energéticos ao largo da praia de Almagreira: H_s = 2 m e T_p = 10 s (caso A); H_s = 2 m e T_p = 12 s (caso B); H_s = 2 m e T_p = 14 s (caso C); H_s = 3 m e T_p = 14 s (caso D); H_s = 4 m e T_p = 14 s (caso E); H_s = 3 m e T_p = 16 s (caso F).

Para esses seis estados de mar, realizou-se um estudo de sensibilidade do modelo SNL-SWAN na presença de 10 WECs do tipo WaveRoller. Na execução destes testes usou-se um domínio de duas malhas encaixadas. Como a gama de frequências recomendada pelo manual do utilizador do SWAN (Ruehl *et al.*, 2014) em áreas costeiras deu resultados incorretos, foi necessário definir diferentes gamas de frequência para os seis estudos de caso, dependendo do período de pico de entrada do SNL-SWAN.

Foram então avaliados as cinco formas de representação de dispositivos de energia das ondas que se encontram incorporados no modelo SNL-SWAN, designados por OBCASE 0 a 4. OBCASE 0 é igual ao modelo SWAN nativo, os OBCASEs 3 e 4 não funcionarem devido a um erro no código da versão SNL-SWAN usada no presente trabalho e o OBCASE 1 conduziu a maiores reduções relativas da altura significativa das ondas e mais absorção de energia que o OBCASE 2.

Como o objetivo do presente trabalho era examinar os efeitos dos disponitivos de aproveitamento de energia das ondas na hidrodinâmica da zona próxima e distante a sotamar dos dispositivos, escolheu-se o OBCASE 1 porque representa o pior cenário em termos de mudanças na altura significativa das ondas.

Considerando a representação OBCASE 1 e os seis estados do mar selecionados, realizaram-se simulações com o modelo SNL-SWAN para examinar os efeitos da variação das características dos campos de dispositivos de aproveitamento de energia das ondas (configuração dos campos de WEC, espaçamento dos dispositivos WEC dentro do conjunto, número de dispositivos WEC do campo) nas condições de onda dos campos próximo e distante a sotamar dos dispositivos WEC.

Para avaliar o efeito de interação de uma configuração de vários WECs na potência extraída, foi utilizado o fator de interação (-fator). Neste estudo de caso, a configuração com os WECs alinhados ao longo de uma única linha resultou no fator q mais alto, que é o melhor em termos de desempenho. No entanto, para ter um número maior de dispositivos numa área confinada próximo da costa, escolheu-se uma configuração mais compacta com os dispositivos alternados em mais linhas. O espaçamento ideal entre dois dispositivos na mesma linha foi de 50 m, enquanto entre dois dispositivos em linhas diferentes foi de 20 m.

Com essa configuração, estudou-se a propagação de ondas na presença de um campo de ondas de 10 a 100 WECs para os seis estados de mar, para ondas de 315°. O impacto do campo de ondas na altura significativa, período médio e direção da onda foi avaliado em termos de variação relativa a partir de uma base de referência, em que esta corresponde aos resultados do modelo na ausência de WECs. Pode-se observar que, quando o número de WECs aumenta, a área de influência aumenta e a altura das ondas a sotamar do campo de ondas diminui. Em particular, a altura significativa das ondas diminuiu até 60% entre as condições de base de referência e as modeladas para 10 WECs e até 80% para 100 WECs, o que corresponde a uma diferença na altura significativa de mais de 3 m. As mudanças no período de pico foram insignificantes, enquanto o período médio aumentou a sotamar do campo de ondas e diminuiu próximo da costa.

As mudanças na direção das ondas foram negativas no vértice superior direito do campo de ondas, o que significa que as ondas rodam no sentido horário, e positivas no vértice inferior esquerdo, o que significa que as ondas rodam no sentido anti-horário em torno do campo de ondas. Todas as diferenças relativas entre o cenário base de referência e todos os conjuntos de WEC simulados estão dentro de ± 4%, correspondendo a uma variação de ± 10 ° na direção média da onda.

Para estudar o comportamento de um campo de ondas em condições de estado de mar reais, foram estudados 50 WECs do tipo WaveRoller durante 19 anos (de 2000 a 2019) de clima de ondas. Observou-se que há uma variabilidade na altura significativa das ondas maior numa base mensal do que numa base anual.

Em seguida, comparou-se um campo WaveRoller com um campo mWave em Bombora, que é um dispositivo de diferença de pressão submerso. Com o dispositivo do tipo WaveRoller houve maiores reduções nas alturas das ondas a sotamar do conjunto WEC devido ao seu potencial para capturar mais energia do que com o dispositivo do tipo mWave de Bombora. Isto deve-se ao facto da matriz de potências do WaveRoller ter valores maiores do que a matriz de potências mWave de Bombora. Portanto, deve-se prestar muita atenção na obtenção dos valores corretos da matriz de potência elétrica da empresa específica que planeia implantar um determinado dispositivo ou dos estudos de laboratório e testes de campo em curso. Pode-se concluir que, dada uma matriz de potência confiável ou uma curva de largura de captura relativa e o comprimento do dispositivo, o modelo SNL-SWAN pode ser um bom instrumento para comparar o impacto de diferentes tipos de dispositivos WEC.

1 | Introduction

1.1 Motivation

Due to the increase in population and urbanization processes the world energy consumption is rising. According to the World Energy Outlook (WEO) of 2017 by the International Energy Agency (IEA), the global energy needs will rise 30% in 2040 compared to nowadays (International Energy Agency, 2017). To be able to supply the enormous amount of energy required, since the beginning of the industrial revolution in the second half of the 18th, fossil fuels have been consumed at an ever-increasing rate. As a consequence of the human activities using fossil fuels, a gigantic amount of greenhouse gases has been generated which is contributing to the acceleration of global warming (Quadrelli & Peterson, 2007).

With that, environmental issues are arising and a “low-carbon energy revolution” (Pearson & Foxon, 2012) is required to mitigate climate changes and ensure energy security. In this context, the renewable energy industry is emerging with several sustainable and pollutant-free technologies. In the last thirty years, efforts have been made in the development of solar and wind energy generation. However, the marine energy is another source with high energy potential that is slowly beginning to establish itself (e.g., Borthwick, 2016; Hussain *et al.*, 2017; Magagna & Uihlein, 2015).

As reported by the annual International Energy Agency (IEA, 2018), renewable energy will grow, providing almost 30% of power demand in 2023, up from 24% in 2017. During this period, renewables are forecast to reach more than 70% of global electricity generation growth (IEA, 2018). Hydropower is still the largest renewable source, 16% of global electricity demand by 2023, followed by wind (6%), solar photovoltaic (4%) and bioenergy (3%). Hydropower sources includes rivers, oceans or lakes. In particular, ocean wave energy that is leading to a growing interest from the scientific community in the recent years, especially in Europe, although it is still immature compared to other renewable technologies (e.g., Aderinto & Li, 2018; Dalton, 2009; López *et al.*, 2013).

The first generation of renewable energy technologies in Europe has now reached competitive levels, but the electricity supply still needs to be further diversified to meet the 2050 policy objective of reducing greenhouse gas emissions to 80 – 95% below 1990 levels by 2050 (European Commission, 2012). An increase in energy generation from renewable sources is a ‘no-regrets option’ for meeting these objectives according to the European Commission. Wave and tidal energy are the next generation of renewable energy technologies that can help Europe to meet its decarbonization targets (SI Ocean, 2014).

One of the biggest advantages of the ocean waves over other renewable energies is the capacity to cover several coastlines in the world, and several studies addressed the exploitability and distribution of the energy contained within the waves (e.g., Cornett, 2014; Reguero *et al*., 2011; Reikard *et al*., 2017), that is free to be harnessed. Thus, marine energy is consistent, predictable (especially in the case of tidal energy) and abundant since oceans cover about three-quarters of the earth's surface. Also, sea waves have the highest energy density among renewable energy sources (Clément *et al*., 2002) and worldwide the estimated energy production potential for ocean wave energy is around 100000 TWh/year (de Melo Veloso & Castro, 2014).

To extract energy from the ocean's waves several wave energy converters (WECs) have been developed since the late 1940s. However, the current status of the technologies in most of the cases is still in the experimental stage and none of the different conversion technologies got to a large commercial stage. Some companies are taking the next step and implementing their devices in offshore ocean waters but there are still multiple challenges associated with the construction, operation, maintenance of the energy converters and with the wave energy farm optimization, return on investments, lifecycle costs, environmental issues and socio-economic issues. Thus, compared with other renewable energy technologies, such as wind and solar, WEC devices are still at a nascent stage. Even the most successful capturing device (Pelamis) to date has not achieved the same levelized cost of energy as wind and solar energy (Aderinto & Li, 2018). Where the levelized cost of energy measures the average total cost to build and operate a power-generating device over its lifetime divided by the total energy output of the device over that lifetime, therefore it allows to compare different technologies.

Therefore, more research on ocean waves technology is required, to better understand the complexity of wave energy spatial and temporal variability and the best placement of WEC devices so that a higher efficiency in energy capture methods can be obtained. Also, to improve the efficiency a focus on arrays of wave energy converters (wave farm) is required because they can increase the total power output (Falcão, 2010; Nader *et al.*, 2012). A good review of the status of WEC arrays in Europe, USA and Australia can be found in De Chowdhury *et al.* (2015) and Rusu & Onea (2018).

However, their presence can alter significantly the wave propagation patterns (Chang *et al.* 2016; Rusu & Guedes Soares, 2013), and so, it is fundamental to preview their impact in the nearshore wave climate. In fact, the presence of the devices remove energy from the waves at an offshore or nearshore site and consequently alters the wave characteristics (height, period, power etc.) as they propagate further towards the coast (e.g., Millar *et al*., 2007; Palha *et al*., 2010; Smith *et al*., 2012). These modifications can have impacts on the shoreline hydrodynamic and morphodynamic, which has to be evaluated previously to minimize any subsequent problems.

To evaluate the potential environmental impact of WECs in the coastline numerical modelling is a widely used and important tool. In the specific case of Portugal, the first investment on wave energy was the Pico Oscillating Water Column (OWC) wave energy converter on the island of Pico in the Azores (Falcão, 2000), followed by three-wave energy investments: two at Aguçadoura (AWS, 2000-2004 and Pelamis, 2007-2008), a parish near Póvoa de Varzim (north of Porto), and the WaveRoller at Peniche (north of Lisbon) in 2007 (OES, 2017). The Pico Central was still operational until April 2018. The Aguçadoura Wave Farm was the world's first wave farm to be installed, with 3 Pelamis WECs and a capacity of 2.25 MW. It was officially opened on September 2008 but shut down two months after due to technical and financing problems. This evidences the fact that a technology adjusted to the natural conditions of the Portuguese offshore is not yet available.

The Finnish company AW Energy demonstrated interest in Almagreira beach in the north of Peniche (Figure 1.1) to install a WEC device. The peculiarity of this area is that is close to the Nazaré Canyon, the biggest submarine canyon in Europe. Its head is situated near the shore, which causes a significant influence on the hydrodynamic and sediment transport processes. The AW Energy company installed a first 1:4 scale WaveRoller prototype in 2007. Then, a 1:2 scale grid connected WaveRoller prototype (3 modules of 100 kW each) was in operation periodically from 2012 to 2015. The company goal for 2018-2020 is to have a full-scale grid-connected and fully operational wave farm. At present, the pilot phase has been completed and right now the Peniche site is fully licensed. Funding and support are being arranged.

Previous studies have already focused on the potential effects of WaveRoller devices on the marine environment (Cruz et al. 2015; Rocha, 2016), but the wave farm effects in the site of Almagreira still needs to be better studied and characterized.

In this framework, the evaluation of the impact of a WaveRoller, or other kind of wave converter, in the nearshore wave climate at the Almagreira beach in Peniche is an interesting research. Moreover, the study of different types, number and positions of wave converters of a wave farm, at Almagreira site, as well as their impact on the nearshore wave climate is also important.

The approach of this study will help, through different numerical simulations, to understand the impact of WEC farms on the wave climate at the specific area of Almagreira beach, in Peniche. Accurate information regarding the behaviour of the waves in the presence of obstacles (WECs) can be useful to the AW-Energy company, the Eneólica company or other future WEC companies interested in implementing devices in this site, as valuable data to contribute to the location of the WaveRoller or other WEC devices.

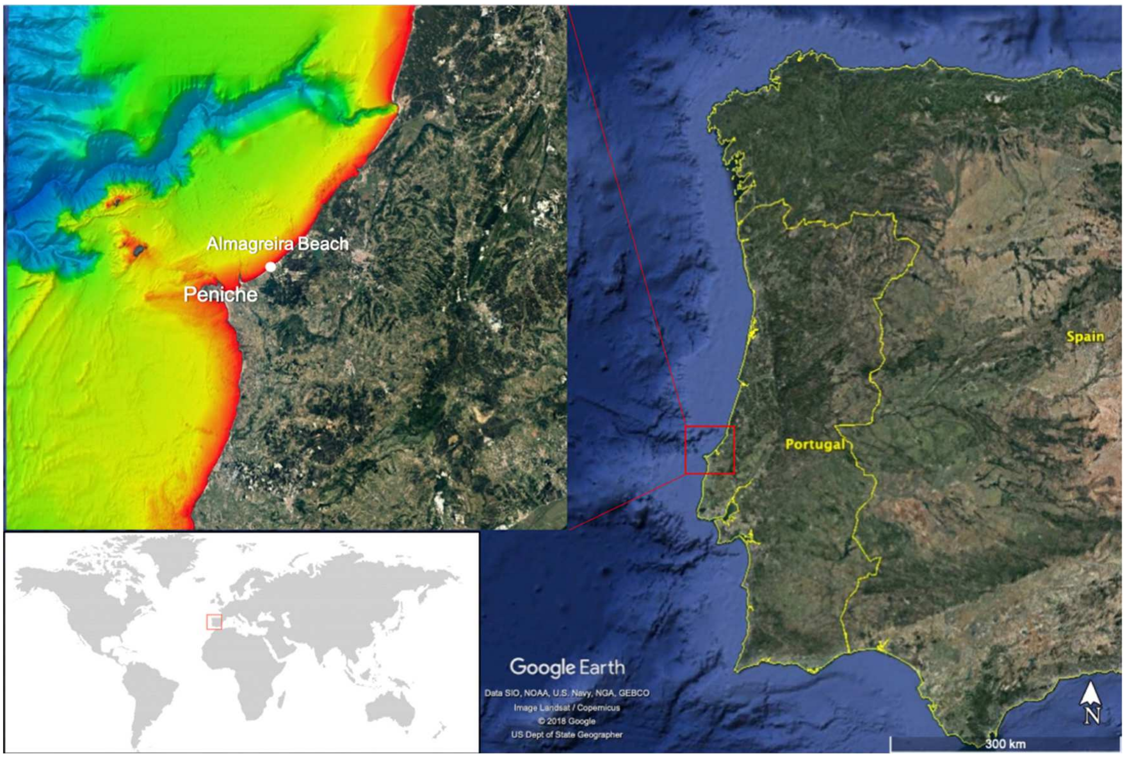

Figure 1.1 Study area location and bathymetry (from EMODNet): Almagreira beach (Peniche), Portugal. Source: Google Earth.

1.2 Main goals

The main objective of the present work was to study, by using numerical modelling, the impact of wave farms on the wave patterns near the coastline. The wave propagation model SNL-SWAN is used and it allows to incorporate device-specific WEC characteristics. The study area is the nearshore Almagreira beach in Peniche, a Portuguese coastal town that is already a pilot test area.

The wave propagation and transformation are analyzed considering the presence of different number, positions and types of wave energy converters for several incident wave conditions that were decided depending on their frequency and energetic potential.

In detail, the present work aimed at accomplishing the following steps:

1. Characterise the wave resource offshore and nearshore Almagreira beach in Peniche, with reference to the potential power available and identify the most common and energetic sea states;
2. Perform model sensitivity analysis on SNL-SWAN, a spectral third-generation numerical model which allows the incorporation of device-specific WEC characteristics. This allows to

examine the effects of different parameters on the model and define the optimal set-up before applying SNL-SWAN in the presence of wave farm;

3. Perform numerical simulations of the wave propagation and transformation from offshore to inshore of Almagreira beach to assess the impact of WECs characteristics on near-field and far-field wave conditions in the lee of the farm. Different WEC characteristics are tested: number of WECs, spacing within the WECs array and type of WEC;
4. Compare between two different kind of WECs, a bottom-fixed oscillating flap (similar to the WaveRoller) and a submerged pressure differential device (similar to the Bombora's mWave), to evaluate the differences in terms of wave energy extraction and on the wave climate near the Almagreira coastline.

1.3 Methodology

The methodology used in the present work aims at applying the SNL-SWAN wave model to evaluate the impact of a farm of WaveRoller type of WECs in the coastline north of Peniche, in terms of the wave parameters (significant wave height, peak and mean period and mean wave direction).

A preliminary literature review was performed on wave energy conversion, on the type of devices available nowadays and on the numerical wave model selected for this study (chapter 2 |). Then the study area, located off the Almagreira beach (39.37° N, 9.31° W), was characterized and the SNL-SWAN model has been applied without (chapter 3 |) and with the presence of a WECs farm (chapter 4 |).

The first step was to download the bathymetric data of the area from the EMODNet (European Marine Observation and Data Network) Bathymetry portal (http://portal.emodnet-bathymetry.eu). The second step was to validate the SNL-SWAN model results against the "Nazaré Costeira" buoy data.

After that, it was necessary to characterize the offshore and nearshore wave climate of the study area, and especially to choose the main representative sea states, that means the most common and energetic. Those were inferred from the analysis of the data obtained from 19 years (from 2000 to 2018) of wave climate simulated with SNL-SWAN without the presence of WECs.

The probability of occurrence of wave sea states was defined, characterized by the significant wave height, peak period and mean wave direction. From that, it was possible to calculate the average annual energy per unit crest length and to define the sea states with the higher mean annual energy that were used for the simulations.

Once the wave climate was characterized, a model sensitivity analysis was performed to understand the SNL-SWAN model behaviour under different set-ups. In particular, SNL-SWAN has five options called “OBCASEs”. A model verification allowed to compare the results from the native SWAN with the results from SNL-SWAN OBCASE 0. The other OBCASEs 1 and 2 were evaluated as well but due to a bug in the formulation of OBCASEs 3 and 4 at the time when this work was performed, it was not possible to evaluate them. However, after contacting the developers of SNL-SWAN the bug has now been resolved and in the latest version of the model (available at https://github.com/SNL-WaterPower/SNL-SWAN).

SNL-SWAN estimates wave transmission through a line-structure such as a breakwater, that affects the wavefield in two ways: it reduces the wave height locally all along its length and it causes diffraction and reflection around its end(s). Obstacles are usually modelled as a line if they have a transversal area that is too small to be resolved by the bottom grid in SNL-SWAN (SWAN, 2018). In the present study, the WEC obstacle implemented into the SNL-SWAN model is similar to a WaveRoller.

To analyze the effects of the wave farm on the coastline, two types of simulations with the SNL-SWAN model were performed: one without the WECs and the other in the presence of a farm of 10 to 100 WECs. For the latter, the wave transformation and propagation were analyzed in the presence of a different number and positions of wave energy converters. Also, the interaction and influence of a single device on the surrounding WECs was analyzed to identify the optimal configuration for energy extraction. As a result of all the simulations, it was possible to identify the differences in significant wave height, wave direction and wave period before and after the installation of a wave farm.

Previous studies have already focused on the potential effects of WaveRoller devices on the marine environment (Cruz *et al*. 2015; Rocha, 2016), but the wave farm effects in the site of Almagreira still needs to be better studied and characterized. Under the same scope, a comparison between the results obtained with the devices similar to the WaveRoller and the devices similar to the Bombora’s mWave was performed.

2 | Literature review

2.1 Early stages of wave energy exploitation

Wave energy is related to the energy radiated by the sun, like most renewable sources: the heating of the earth releases a great amount of energy on the air-sea interface and this generates wind and capillary waves. Under favorable wind conditions, those waves can grow and become more consistent surface gravity waves (swell) with a high energy density, that is what interest the WECs industry.

Therefore, the dominant factors in wave formation are the wind speed, the water distance on which the wind blows (fetch), the depth and topography of seafloor (in case of nearshore and inshore devices). The power in a wave is proportional to the square of the amplitude and to the period of the motion. For instance, waves with long periods (7–10 s) and large amplitude (2 m) have energy fluxes commonly averaging between 40 and 70 kW per m width of incoming wave (Clément *et al.*, 2002).

Thus, waves are a regular and unlimited source of renewable energy that can be predicted several days in advance and once created they can travel thousands of miles without significant energy losses until they approach the coast (de Melo Veloso & Castro, 2014). For example, the storms originated from the western side of the Atlantic Ocean can travel until the western coast of Europe with little energy loss.

In the early 1980s, the petroleum price declined and wave-energy funding was drastically reduced (López *et al.*, 2013). Thus, until the early 1990s, most of the activities remained at a theoretical level because of the complex hydrodynamic of wave energy absorption. Only in 1991, the situation changed when wave energy was added to the European Commission's JOULE (Joint opportunities for Unconventional or Long-term Energy Supply) program for the development of renewable energies. In 1994 the research programs of the Commission on wave energy effectively started with the forth Framework Program.

Since then, most of the research and development (R&D) activities related to wave energy has been taking place in Europe (Falcão, 2010), including a series of European Wave Energy Conferences and the biennial International Conference on Ocean Energy. In 2001, the International Energy Agency (IEA) established an Ocean Energy System (OES) Implementation Agreement to facilitate the coordination of ocean energy studies between countries (OES, 2014). In the IEA-OES annual reports it is possible to find surveys of ongoing activities in wave energy worldwid. In particular, the Annual Report published in 2017 by the Executive Committee of OES presents an overview of the worldwide activities in the ocean energy sector (OES, 2017).

Today, many diverse research institutes and private companies are working on the improvement of the WECs. Most of those are established around Europe, USA, China, Japan, and Australia (Antonio Falcão, 2014). There are several reviews of the current activities in the wave energy sector in Europe and in the world (e.g., Aderinto & Li, 2018; Clément *et al.*, 2002; Drew *et al.*, 2009; Falcão, 2010; Falnes, 2007; López *et al.*, 2013; Melikoglu, 2018; Rusu & Onea, 2018; Uihlein & Magagna, 2016).

2.2 Advantages and disadvantages of harnessing wave energy

From the studies above mentioned, the wave energy results to have several advantages if compared to other renewable energies (Akar & Akdoğan, 2018):

1. It is sustainable, as it combines economic, environmental, ethical and social factors;
2. Its energy density and deployment potential are higher than the wind and solar energy. It is estimated that wave energy power has a density of 2–3 kW/m^2 while solar energy has a density of 0.1– 0.2 kW/m^2 and wind energy of 0.4–0.6 kW/m^2 (López *et al.*, 2013). Also, wave energy converters can theoretically generate power up to the 90% of the time, while the percentage is 20–30% for wind and solar devices (Drew *et al.*, 2009). Furthermore, wave energy has a good correlation between resource and demand because about 38% of the population in the world lives 20 km distant from the coastline (Small & Nicholls, 2003);
3. Wave energy has minor negative environmental impacts and the production amount of the wave energy is predictable (usually more than 48 h in advance);
4. It is an energy source that can be installed at multiple locations, from the shoreline to offshore;
5. It has little environmental interference and from modelling studies, WEC farms located nearshore have been found to act as coastal defence elements due to wave energy absorption and dissipation induced by the obstacles (Bergillos *et al.*, 2018; Ruol *et al.*, 2011; Zanuttigh & Angelelli, 2013).

On the other hand, the disadvantages must be mentioned as well. The main two reasons why wave energy industry is struggling to reach the same level of viability as wind and solar energy are survivability and Levelized Cost of Energy (LCOE) (Sandberg *et al.*, 2016). The LCOE is a parameter used to evaluate the viability of a WEC system and it is based on the total life cycle costs and the total energy generated throughout the lifespan of the system. When WECs are deployed at offshore locations, they can be affected by extreme wave heights more than six times greater than the prevailing operating conditions at the same location. It is technically possible to allow a WEC to survive the very high loads in these extreme conditions, but the costs increase. A viable WEC solution must compensate for the high cost of over-engineering the WEC to survive harsh conditions by increasing power production.

Funding is another important barrier. Even though waves are an energy source with great potential and with several advantages that make them an attractive option, they have to compete against more mature technologies where the investment is already done. In addition, WEC developers must overcome challenges like environmental impacts (changes in habitat and hydrological conditions), social acceptance, regulatory obstacles, interference with commercial and recreational operations, impact on coastal ecosystems (such as acoustic and electromagnetic noise) and power integration (e.g., Dalton, 2009; Langhamer *et al.*, 2009; Tiron *et al.*, 2015; Witt *et al.*, 2012).

2.3 World wave energy resource

To develop those wave energy technologies and to select suitable sites for wave farms, it is necessary to know the available wave climate and to estimate the wave power. In this regard, several papers already showed the existing wave power worldwide (e.g., Arinaga & Cheung, 2012; Barstow *et al.*, 2009; Cornett, 2008; Cruz, 2008; Reguero *et al.*, 2011; Rusu & Onea, 2017). From these works resulted that the highest wave energy zones in the world are on the western coasts of the continents, especially between 40º and 60º latitude in each hemisphere (Rusu & Onea, 2017). There the distribution of the mean wave power density ranges between 40 and almost 130 kW/m, as can be seen from the map in Figure 2.1 and previous analysis of mean wave power density. The data are reanalyzed from the European Centre for Medium-Range Weather Forecasts (ECMWF) database. Annually, the highest wave energy levels in the Northern Hemisphere are off the west coast of the British Isles, Iceland and Greenland, with lower energy levels in the Western Coast of Canada, USA, and Mexico, as well, in the coast of Portugal, France, and Spain. The Southern Hemisphere highest wave energy levels are in Chile, South Africa and the southern coastline of Australia and New Zealand.

Defining the average wave energy resource is not enough to characterize a possible site where to implement wave farms. It is also necessary to consider the effect of the variability of this resource on the WEC performance, which can be restricted in the case of highly energetic sea-states. When the excess wave power in sea-states is larger than a threshold power level it is not exploitable because after a certain incident wave power level there is no increase in power capture. This threshold depends on the WEC, however, a criterion has been established: the threshold at which wave power is not exploitable due to high energetic sea states is defined as four times the average incident wave power (Folley & Whittaker, 2009). With this assumption, the wave power in the North Atlantic is exploitable until 60 kW/m (López *et al.*, 2013).

Another important parameter to characterize and evaluate the world wave energy resource is its variability. Sites with an unsteady energy flux are less reliable because the extreme wave conditions (e.g. during storms) can damage the WECs. Also, the efficiency of WEC devices is maximum for a range of wave heights and periods but also it can depend on waves direction for some type of WECs. Since there can be daily, weekly, monthly and seasonal variabilities, a coefficient is generally used to describe this temporal variability. Given a wave power time series, the coefficient of variation (COV) is defined as the standard deviation (s) of the power time series $P(t)$ over the mean power (μ) (Cornett, 2008):

$$COV(P) = \frac{s(P(t))}{\mu(P(t))} \tag{1}$$

From the global distribution of COV(P) in Figure 2.2 can be seen that the temporal variability of wave resources is lower near the equator in the Atlantic, Pacific and Indian Oceans, and it increases at higher latitudes. Small values of COV(P) means that the wave resources are stable.

Therefore, due to the high and stable energy wave climate along the western coast of Europe, most of the researches on wave energy have been performed in the United Kingdom, Portugal, Ireland, Norway, Sweden and Denmark. The Atlantic Coast of Europe is one of the most important marine renewable energy resources in the world (Gleizon *et al*., 2017) with 50% of WECs developed there (Antonio Falcão, 2014). The reason is that the North Atlantic weather system is governed by the North Atlantic Oscillation, therefore by the presence of westerly winds that generate swells that travel more than 3000 km before reaching the European coast. Thus, due to its extensive coastline and high energy potential Portugal is a great location for wave energy extraction. Its coast has privileged conditions for the development and utilization of wave energy, with an average annual value of wave power density of about 40 kW/m (de Melo Veloso & Castro, 2014).

A detailed wave energy resource assessment of Portugal has already been published (Pontes *et al*., 2005) and several projects have been carried out over the years. The first one was the pilot Oscillating Water Column plant designed and constructed in the Island of Pico (Azores) between 1995 and 1999. Followed by the AWS pilot plant in Viana do Castelo in 2002, the Pelamis wave farm in Aguçadoura in 2008 and by the WaveRoller in Peniche, tested since 2007. At the present moment, Portugal has a National Ocean Strategy (NOS 2013-2020) to develop its maritime potential and in 2017 the Portuguese Government approved the Industrial Strategy for Oceanic Renewable Energies (EI-ERO) with a set of measures for wave energy.

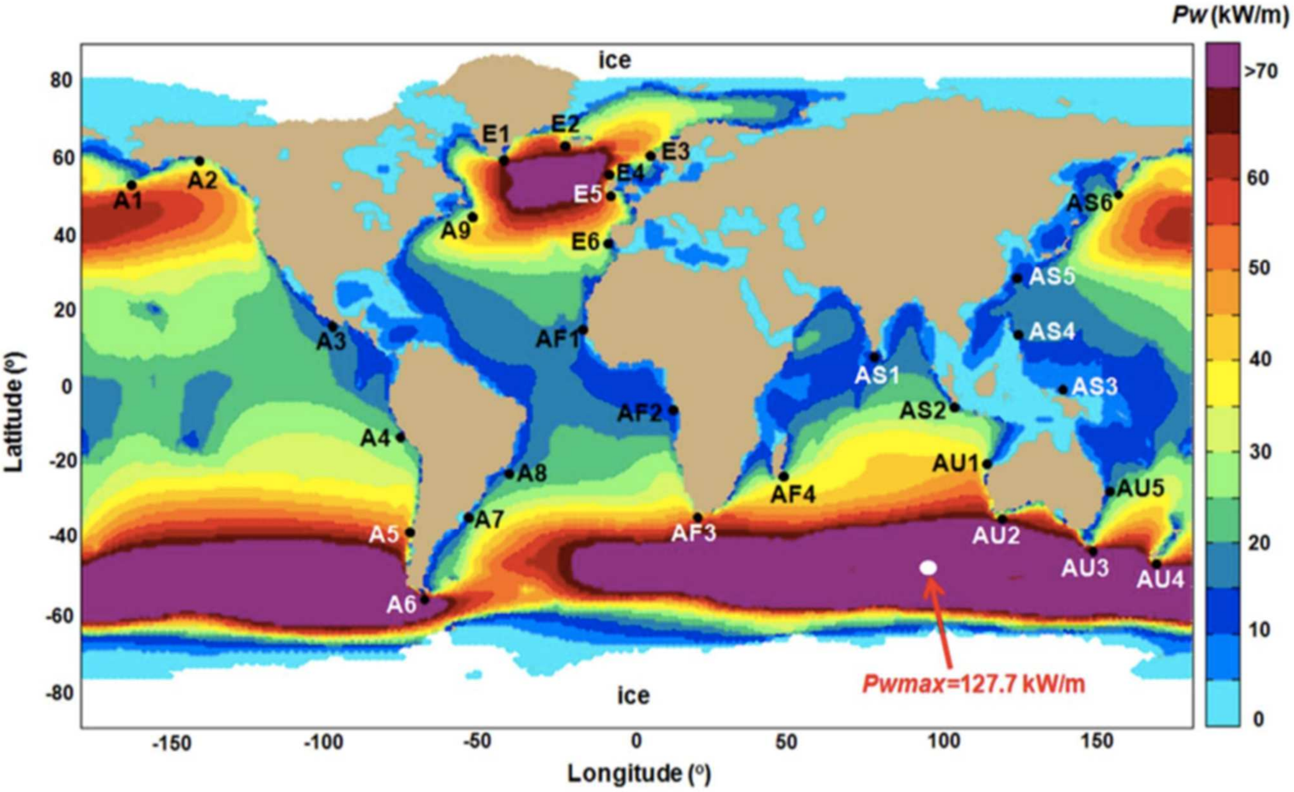

Figure 2.1 Map of the mean wave power density (in kW/m) for 15-year interval (January 2000-December 2014). Data were taken from the European Centre for Medium-Range Weather Forecasts (ECMWF) database and reanalysed by the ERA-Interim project. Source: L. Rusu & Onea (2017).

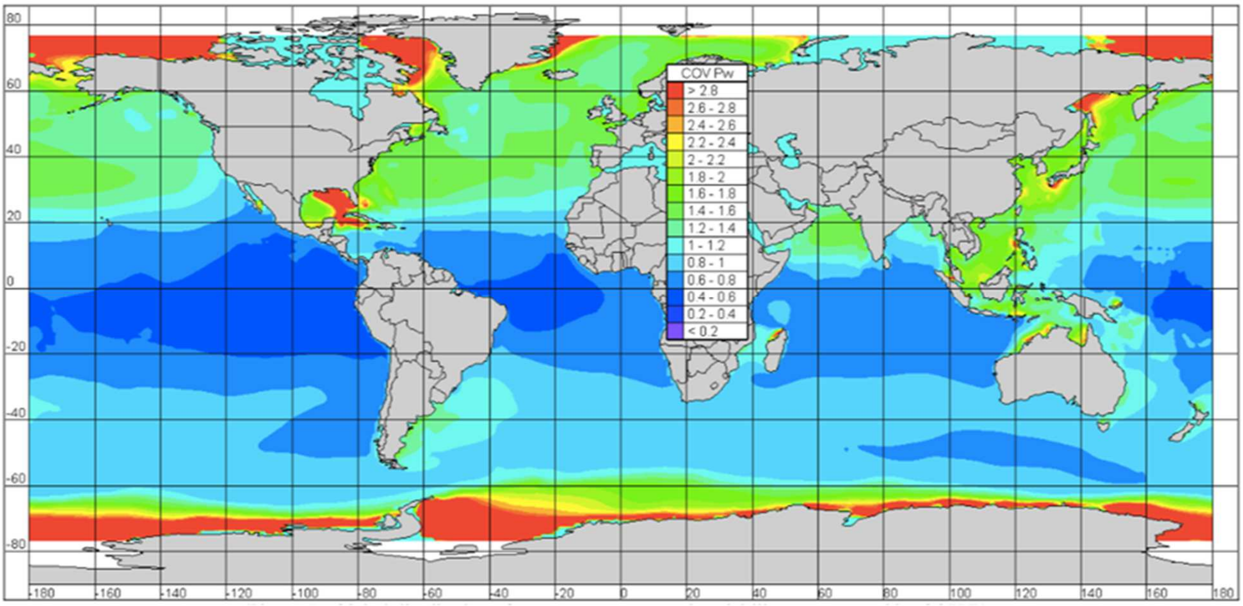

Figure 2.2 Map of global distribution of wave power temporal variability, represented by the COV(P). The results are obtained from an analysis of the NOAA WAVEWATCHIII-Global wave climatology every 3 hours over 10 years (1997-2006). Source: Cornett (2008).

2.4 WEC devices

2.4.1 History

Extracting wave energy implies the use of WECs to transform it, first in mechanical energy, then in electricity. Thus, the idea of extracting ocean's energy has been considered since more than two hundred years ago. It started in 1799 when the French inventor Girard obtained a patent for a machine designed by him and his son to mechanically capture the energy from waves (Clément *et al.*, 2002). Another early application of wave power was a device constructed in 1910 by the French Bochaux-Praceique to light and power his house in Royan.

After that, thousands more patents followed (some documented by Leishman and Scobie in 1976) and several books and reports on wave energy conversion were written. Since the beginning, the WEC industry has had many ups and downs, with almost 150 projects (either conceptual or operational). An overview of the current status of wave energy conversion can be found in (Antonio Falcão, 2014).

The pioneer for modern wave energy and of the Oscillating Water Column (OWC) system is Yoshio Masuda that started to work with ocean energy devices in the late 1940s. He developed the first example of floating OWC: a navigation buoy powered by wave energy and equipped with an air turbine. Later in 1976, he promoted the construction of a larger device testing platform composed by several OWCs equipped with different types of air turbines.

With the oil crisis of 1973 wave energy got a new interest and intensive research and development study began. In 1974 a paper published in *Nature* by Stephen Salter brought the wave power technology to the attention of the international scientific community (Salter, 1974). He also started the experimental development of a WEC in the wave flume of the University of Edinburgh. In the same period, Kjell Budal pioneered this technology in Europe developing a phase-controlled point absorber power buoy (Budal & Falnes, 1974) while Michael E. McCormick was the first academic to work with this technology in America (McCormick, 1981).

Some prototype applications have been developed in wave tanks in Trondheim (Norway), Wageningen (Netherlands) and Nantes (France) and some in the sea. Just to mention some first projects, in 1985 two full-sized (350 and 500 kW rated power) shoreline prototypes were constructed at Toftestallen in Norway. In 1990 two OWC prototypes were constructed in Asia, a 60 kW converter at the port of Sakata, Japan and a bottom-standing 125 kW plant at Trivandrum, India. In 1991 a small (75 kW) OWC shoreline prototype was deployed at the island of Islay, Scotland (Falcão, 2010). In

1992 the OWC Pico Power Plant project started in the Azores and the construction of a full-scale testing facility was concluded in 1999.

2.4.2 Types of devices

A wide variety of WECs have been developed along the years and the number of wave energy companies existing nowadays is more than 200. A list of the existing technologies and the leading companies can be found in the European Marine Energy Center (EMEC) website (http://www.emec.org.uk/marine-energy/wave-developers/, last updated: 8th August 2019). WEC devices can be classified according to location, size and working principle. About the location, they can be found onshore (in shallow waters), nearshore (few hundred meters from the shore at a depth of 10-25 m) or offshore (waters deeper than 40 m).

If, instead, we consider the WECs working principle the following main eight types of devices (Figure 2.3) have been identified by EMEC (Rusu & Onea, 2018): attenuators, point absorbers, oscillating water columns, overtopping/terminator devices, submerged pressure differential, bulge wave, rotating mass and oscillating wave surge converters.

The attenuators (Figure 2.3A) are floating devices oriented along the wave direction with a long structure concerning the wave direction. They are composed by a series of cylindrical sections connected together by flexible joints that allow each individual section to rotate relatively to the others. Thus, they gradually generate energy as the wave passes through the system length and "attenuate" the amplitude of the wave. An example is the Pelamis prototype converter from UK (Henderson, 2006).

Point absorbers (Figure 2.3B) are floating structures similar to a buoy, in which the active part moves on a vertical axis. They absorb the wave energy in all directions through their movements at the water surface and convert into electrical power the motion of the buoyant top relative to the base. They have small dimensions compared to the typical wavelength, tending to have a diameter of a few meters. An example of point absorber is the OPT PowerBuoy (Chen *et al.*, 2013).

The Oscillating Water Columns (OWCs, Figure 2.3D) can be located on the shoreline or near shore and they are based on the same principle of the previously described devices. The movement of the waves raises and lowers the level of water inside a semi-submerged chamber open at the bottom. This causes an internal volume of air to move and a turbine to rotate. This technology has been applied in the Limpet power plant in UK (Heath, 2000) and the Pico power plant in Azores, Portugal (Falcão, 2000). Floating structures are based on a floating body that is moved by the waves and the oscillatory movement used by the device can be vertical, horizontal, pitch or a combination of those. An example is the WaveStar WEC (Marquis *et al*., 2012).

Overtopping devices (Figure 2.3E) have a structure that due to waves increases its potential energy and/or kinetic energy. The water is forced to pass over this structure that is a reservoir above the sea level and then is released back to sea through turbines. A typical overtopping device is the Wave Dragon in Wales and Denmark (Kofoed *et al*., 2006) and the SSG Wave Energy Converter in Norway (Vicinanza *et al*., 2012). Terminators are also long structures similar to attenuators. However, these are placed perpendicular to the predominant direction of wave propagation and they "terminate" the wave action. One example of the terminator-type WEC is the Salter's Duck (Falnes, 2007).

The submerged pressure differential device (Figure 2.3F) is typically located near shore and fixed to the seabed. It is a submerged point absorber that uses the pressure difference generated between the wave crests and troughs. When the crest of the wave is over the device, this water pressure compresses the air that is inside of it and moves the device down. If the trough is over the device, the water pressure will be reduced and the device rises. An example of this type of converter is the Archimedes Wave Swing, AWS in UK (de Sousa Prado *et al*., 2006) and the Bombora's mWave (https://www.bomborawave.com) in Australia. As waves pass over the mWave (Figure 2.5), the air inside the membranes is squeezed into a duct and through a turbine that spins a generator to produce electricity. The air is then recycled to re-inflate the membranes so that they are ready for the next wave. A feasibility study was performed by Brito e Melo & Villate (2016) for a 60 MW wave farm in Peniche and in 2016 they applied for the license of a prototype there.

Bulge wave technology (Figure 2.3G) use wave-induced pressure to generate a bulge wave within a flexible tube, such as the Anaconda wave energy converter (Heller *et al*., 2010). As the bulge wave travels within the device it increases in size and speed. The kinetic energy of the bulge is used to drive a turbine at the end of the tube.

Rotating mass converters (Figure 2.3H) exploit the relative motion of waves to induce pitching and rolling in a floating body, forcing the rotation of an eccentric mass contained within the device that drives an electrical generator. An example of this device is the Penguin by Wello.

And finally, the Oscillating Wave Surge Converters (OWSC, Figure 2.3C) are articulated or flexible structures that are positioned perpendicularly to the wave direction. Thus, due to the impact of the waves, the deflector moves back and forth, such as in the Aquamarine Power Oyster in the UK (Whittaker *et al*., 2007). This is also the case of the device further considered in this study, the WaveRoller OWCS, a device that operates in nearshore areas (approximately 0.3-2 km from the shore) at depths between 8 and 20 m (Figure 2.4).

In the specific case of Almagreira beach, the location of the WaveRoller farm is around 15 m depth (Silva *et al.*, 2016). A single WaveRoller unit (one panel) is rated at between 350 kW and 1000 kW, with a capacity factor of 25-50% according to manufacturers and depending on wave conditions at the project site. A single panel absorbs 1.5-2 MW of power from the wave surge (AW-Energy, 2019). The panel spans essentially the entire depth of the water column from the seabed up to the water surface level and the back and forth movement of water driven by waves puts the composite panel into motion. As it is difficult and expensive to commission WECs in their actual operational environment, the designing of wave energy converters heavily relies on numerical simulations and small-scale experiments.

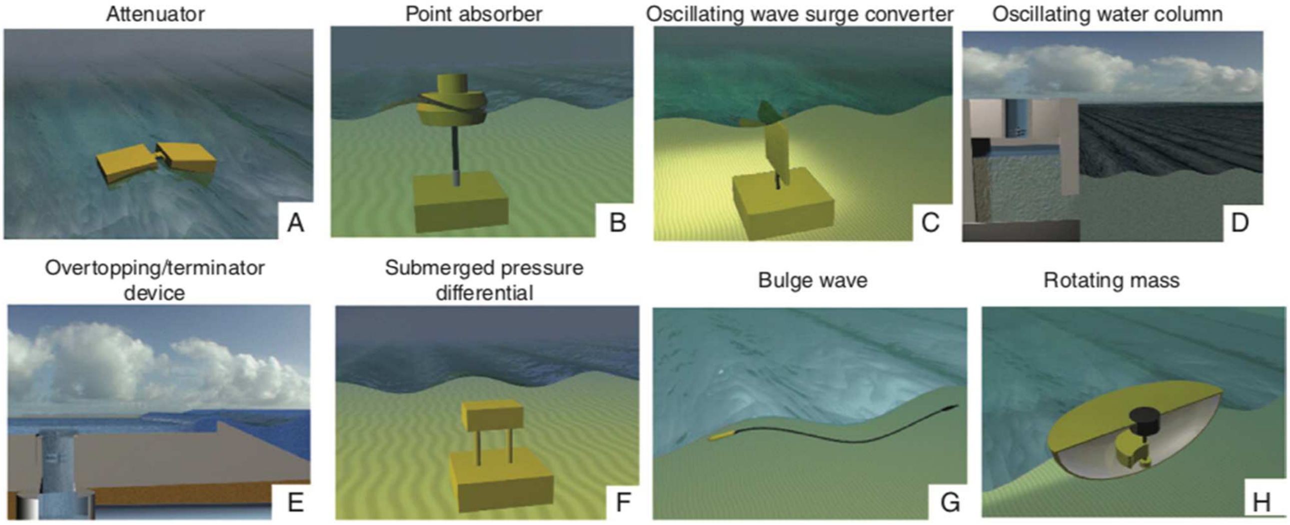

Figure 2.3 Main WECs categories identified by the European Marine Energy Centre. Source: http://www.aquaret.com.

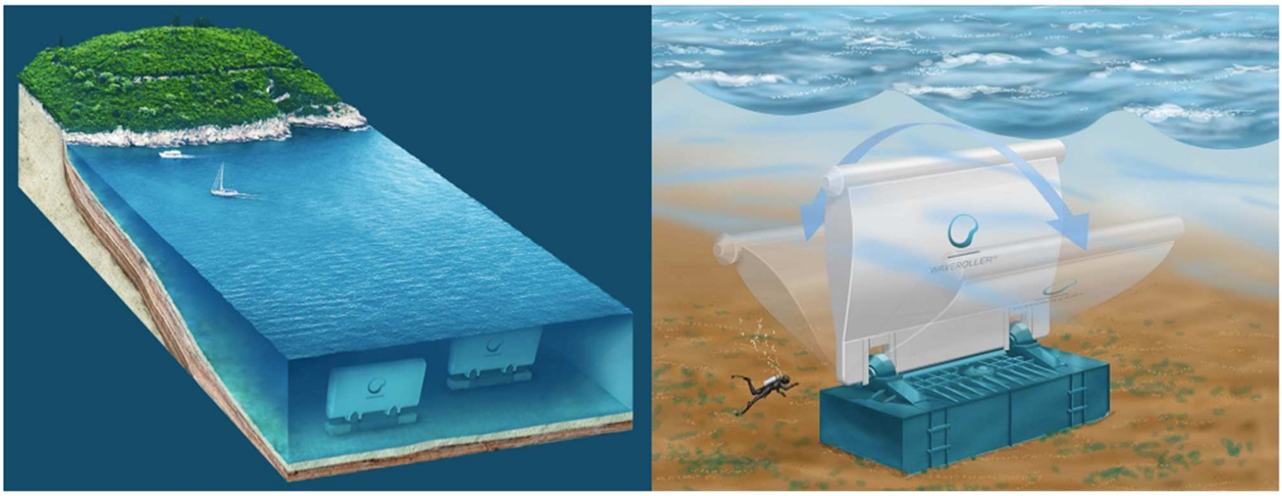

Figure 2.4 An artistic interpretation demonstrating several Oscillating Wave Surge Converter (OWSC) type WaveRoller devices installed in nearshore sub-surface environment. Source: https://aw-energy.com

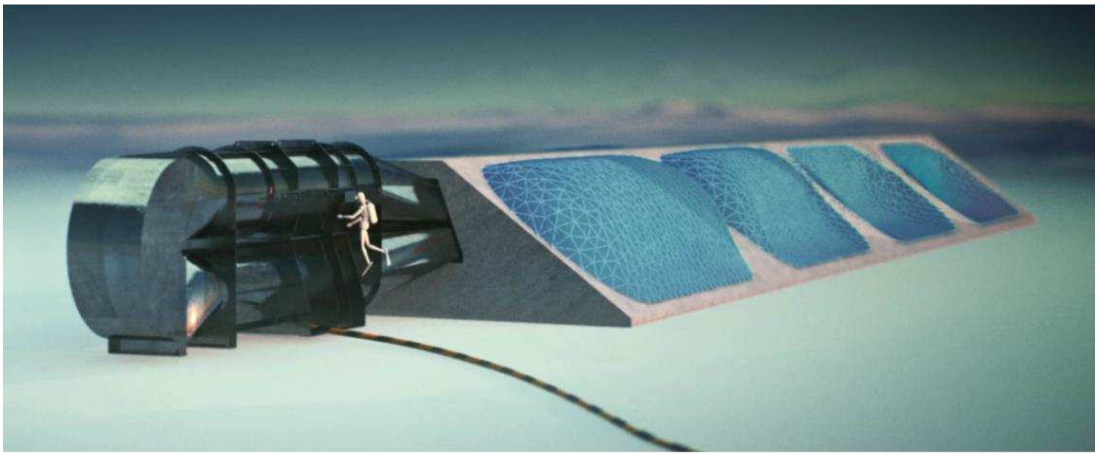

Figure 2.5 An artistic interpretation of the Bombora's mWave membranes and turbine. Source: http://www.bomborawave.com/

For most WECs, a greater annual energy production can be obtained in deep water (assuming the same degree of WEC submergence), because there the annual total incident wave energy is greater. However, the additional energy that is exploitable in deep water comes at a higher cost. Moreover, in many nearshore sites, the exploitable energy reduces by only 10% between the depths typical of offshore and nearshore sites (Folley *et al.*, 2010). The range of wave direction at nearshore locations is reduced due to refraction during shoaling. This increases the proportion of the nearshore wave climate that is exploitable for directional WECs compared to the offshore climate.

Therefore some of the advantages of nearshore devices are that: they face fewer extreme conditions, with a slightly reduced amount of exploitable energy relative to offshore sites; they have cost reduction advantages in terms of installation and maintenance since they are located in a relatively accessible region (Henry *et al.*, 2010; Wilkinson *et al.*, 2017).

2.4.3 Wave Roller and Bombora's mWave devices

A common challenge in WECs modelling is related to the performance parameters of different WEC systems, because often they are not available to the scientific community for reasons of confidentiality (Venugopal *et al.*, 2017). Thus, by reviewing power performance results available in the public literature an extensive database for the hydrodynamic performance of WECs was created by Babarit (2015).

The power matrices can be determined by using numerical models. For instance, the one considered in the present study for a bottom-fixed oscillating flap device (B-OF) was derived with a numerical Wave to Wire time-domain model (Babarit *et al.*, 2012) that solved the equation of motion. It is important to underline that is not exactly the power matrix of a WaveRoller, but of a similar kind of device. The power matrix of the Bombora's mWave device was also numerically predicted for a full-scale 8-cell prototype and was available in the literature (Algie *et al.*, 2017).

The power performance is device-dependent and can be quantified in terms of capture width (CW). The CW was first introduced in 1975 (Budar & Falnes, 1975) and is defined as the ratio of wave power absorbed by the device P_{abs} (in kW) to the wave resource P_{inc} (in kW/m):

$$CW = \frac{P_{abs}}{P_{inc}} \tag{2}$$

More than by the capture width, the hydrodynamic performance of a WEC is best reflected by the hydrodynamic efficiency. A measure of the hydrodynamic efficiency is the ratio between the capture width and a characteristic dimension B of the WEC, often the device width (25 m for the WaveRoller and 62.5m for the Bombora's mWave). This ratio is called relative capture width (RCW) and reflects the fraction of wave power flowing through the device that is absorbed by the device:

$$RCW = \frac{CW}{B} = \frac{P_{abs}}{P_{inc}B} \tag{3}$$

In the present study, the incoming power was calculated while the absorbed power was inferred from the WECs power matrices.

2.4.3.1 WaveRoller WEC type characteristics

To generate electrical power from the surrge motion of waves several wave energy converters have been proposed, including Oyster, EB-Frond, WaveRoller, and Langlee.

The WaveRoller was developed by the Finnish company AW-Energy. It consists of a submerged and movable flap, fixed to the seafloor, between 8 and 20 m depth. The oscillatory movement of the blade controls the hydraulic piston which, connected to an enclosed hydraulic circuit, causes the movement of a high-pressure fluid which is directed to a hydraulic motor, thus supplying an electric generator. The electricity produced is led by cables on the seabed to an underground substation. The entire circuit is hermetically sealed in the system and thus separated from the maritime environment.

After a sequence of tests between 2007 and 2008, in 2012 a demonstration plant with three WaveRoller units of 9 m x 10 m each was installed on the coast of Peniche (project SURGE1), with a total power potential installed of 300 kW/h.

Currently, the project is closed and new improved prototypes are planned for future applications. The total investment in the Waveroller system was € 5.7 million between 2007 and 2014, € 2.4 million of which was invested in projects on the Portuguese coast (Roteiro EI-ERO, 2016). At the moment, Lloyd's Register certified AW-Energy's WaveRoller technology and the SURGE2 project follows the successful SURGE1 project, where AW-Energy demonstrated the technology with a grid-connected device producing electricity to the Portuguese grid from a site fully exposed to the ocean storms (https://aw-energy.com). The SURGE2 project sees a single 18 x 10 m panel delivering

400kW of continuous power. Each panel can take up to 2MW of power from the wave surge, but digital smoothing feeds this out to the grid at a continuous flat rate of 400 kW.

However, since the performance parameters for the specific WaveRoller WEC are not available to the scientific community for reasons of confidentiality a similar device was considered in the present study. It is a bottom-fixed oscillating flap (Figure 2.6) and its characteristics were retrieved from the literature (Babarit *et al.*, 2012; Chang *et al.*, 2016) and summarised in Table 2.1. Also, the power matrix of this kind of device is here reported (Figure 2.7), along with the relative capture width curve (Figure 2.8). This is the reason why in the following chapters this WEC will be called “WaveRoller type”.

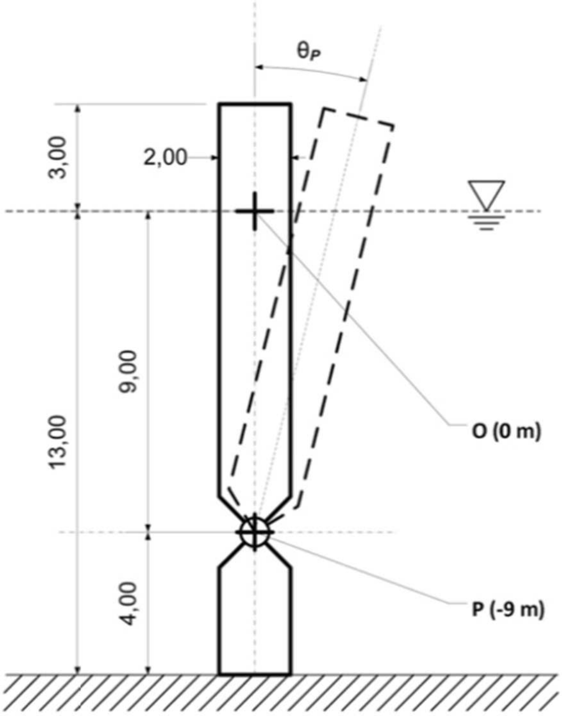

Figure 2.6 Bottom-fixed oscillating flap. Source: Babarit et al. (2012).

Property	Value
Length	25 m
Height	16 m
Width	2 m
Water depth	8-20 m

Table 2.1 Characteristics of the WaveRoller type bottom-fixed oscillating flap. Source: Babarit et al. (2012).

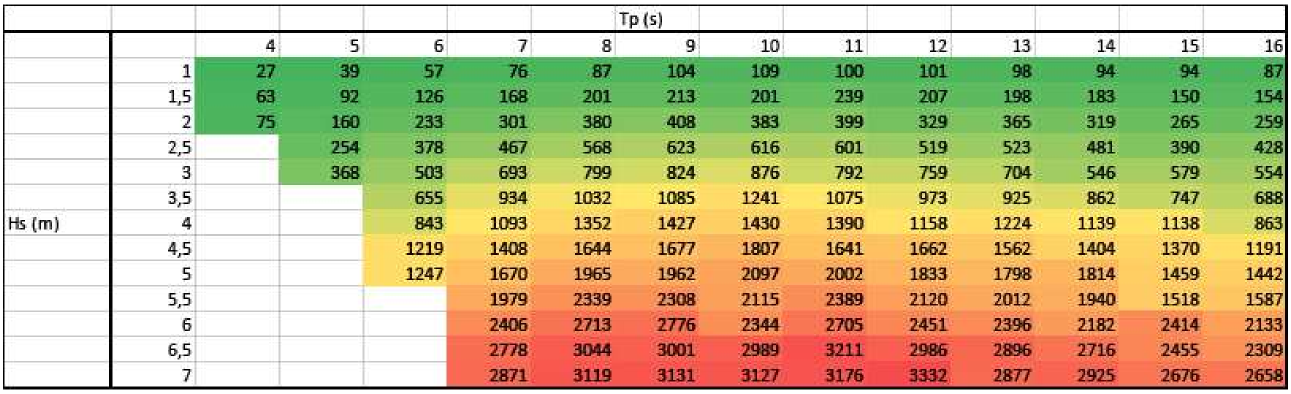

		Tp (s)												
		4	5	6	7	8	9	10	11	12	13	14	15	16
	1	27	39	57	76	87	104	109	100	101	98	94	94	87
	1,5	63	92	126	168	201	213	201	239	207	198	183	150	154
	2	75	160	233	301	380	408	383	399	329	365	319	265	259
	2,5		254	378	467	568	623	616	601	519	523	481	390	428
	3		368	503	693	799	824	876	792	759	704	546	579	554
	3,5			655	934	1032	1085	1241	1075	973	925	862	747	688
Hs (m)	4			843	1093	1352	1427	1430	1390	1158	1224	1139	1138	863
	4,5			1219	1408	1644	1677	1807	1641	1662	1562	1404	1370	1191
	5			1247	1670	1965	1962	2097	2002	1833	1798	1814	1459	1442
	5,5				1979	2339	2308	2115	2389	2120	2012	1940	1518	1587
	6				2406	2713	2776	2344	2705	2451	2396	2182	2414	2133
	6,5				2778	3044	3001	2989	3211	2986	2896	2716	2455	2309
	7				2871	3119	3131	3127	3176	3332	2877	2925	2676	2658

Figure 2.7 Power matrix (in kW) of a bottom-fixed oscillating flap device. H_s is the significant wave height (in meters) and T_p is the peak period (in seconds). Source: Babarit et al. (2012).

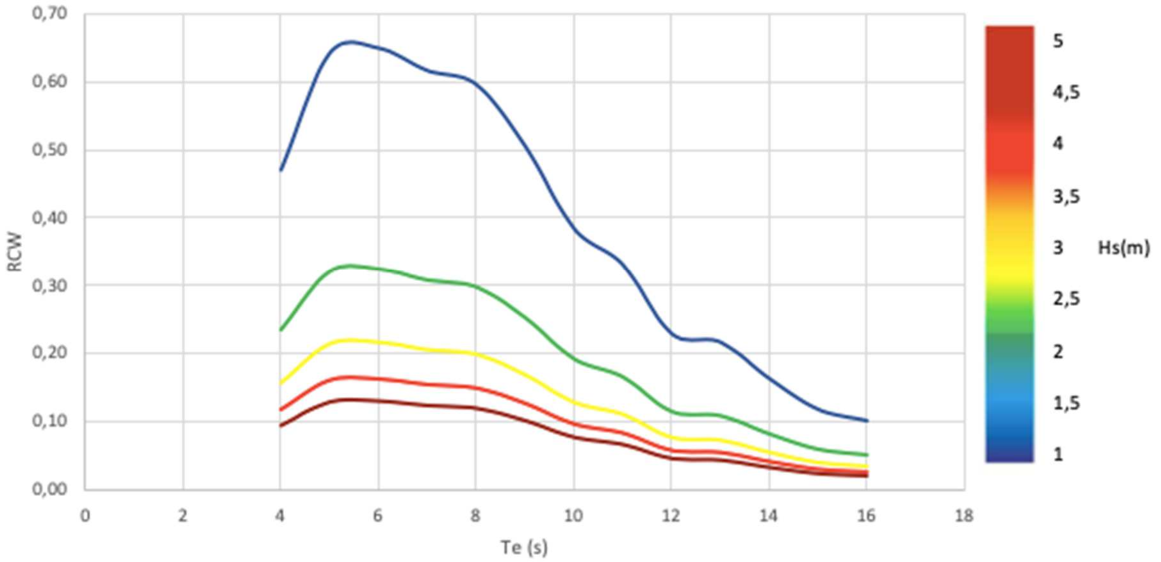

Figure 2.8 Relative capture width curves of a bottom-fixed oscillating flap device as a function of the energy period (T_e in seconds). The colour of the curves indicates the significant wave height for each curve (H_s in meters).

2.4.3.2 Bombora WEC type characteristics

The Australian company Bombora Wave Power was founded in 2012 after obtaining good results with the mWave wave energy converter whose operating concept began to be explored in 2007. The mWave is a submerged, pneumatic, flexible membrane pressure differential WEC that comprises multiple membranes mounted on the sea floor with cells filled with air (Figure 2.9). These cell membranes convert hydrodynamic wave pressure into internal cell air pressure. The differential pressure between cells is caused by wave peaks and troughs above the WEC. At any instant, those cells supply air to a high-pressure duct in the pneumatic circuit, through a set of non-return cell outlet valves. This high-pressure air flows through the turbine and returns to low-pressure cells, through a low-pressure manifold and non-return inlet valves (Algie *et al*., 2017). The electricity produced by the generator is then transported to shore by submarine cables.

The mWave is a nearshore WEC and its installation depth is determined by several factors: with submersion the power capture decrease, due to the increased attenuation of wave pressure with depth but also, prevent the exposure of the converter to high slamming loads a minimum submersion is required. For these reasons, in most long-fetch wave climates the preferred submergence is between 5 and 15 m. The model has already been tested on a small scale in wave tanks and there are several projects in the coastal areas of Scotland, Wales, Australia and Portugal.

The site assessments conducted by Bombora over the last two years confirm that the coast of Portugal is an ideal location for a mWave farm. Bombora conducted a Levelised Cost of Energy (LCOE) study for a 60 MW wave farm at Peniche consisting of 40 WECs. At the moment, Bombora is working closely with WavEC to enable an array of mWave's to be deployed in Peniche by advancing the site consenting process.

The characteristics of the device considered in the present study as a comparison with the WaveRoller type of WEC are reported in Table 2.2. The power matrix of this kind of device and the relative capture width curve are also reported (Figure 2.10 and Figure 2.11).

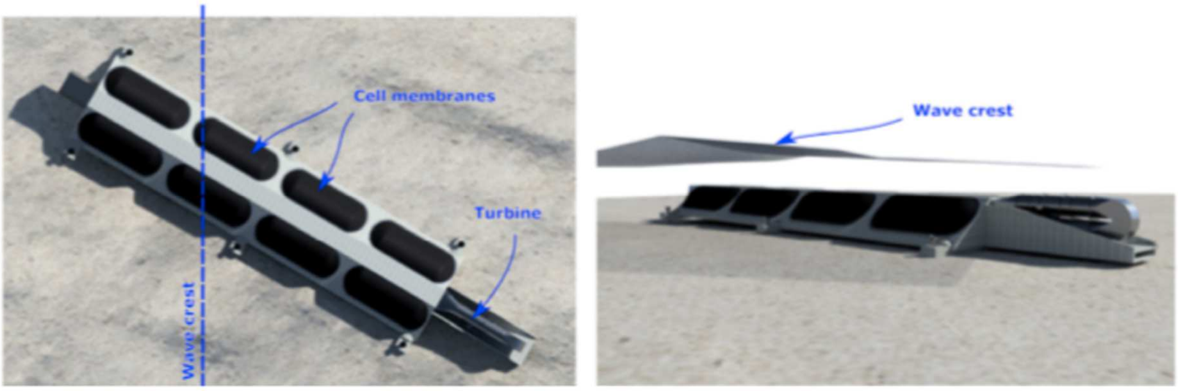

Figure 2.9 mWave prototype in (a) plan and (b) front view, with waves approaching from the left. Source: Algie et al. (2017)

Property	Value
Length	62.5 m
Height	6 m
Width	15 m
Water depth	5-15 m

Table 2.2 Characteristics of the Bombora's mWave pressure differential converter. Source: Algie et al. (2017).

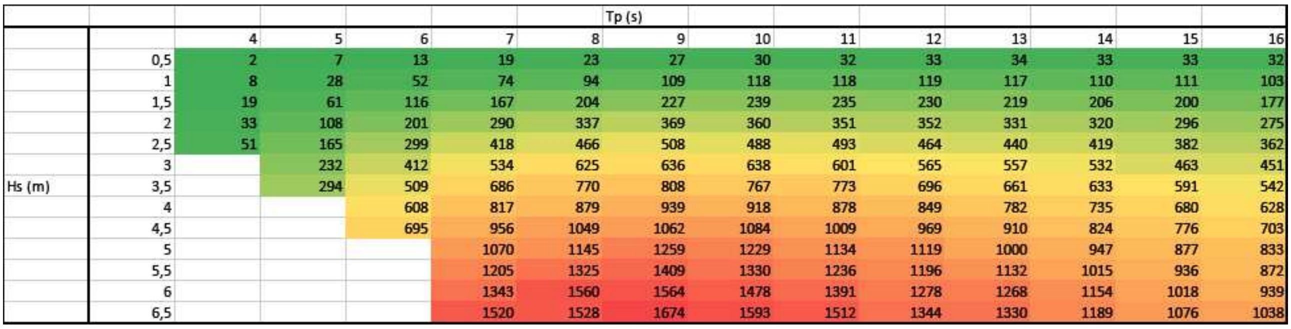

		Tp (s)												
		4	5	6	7	8	9	10	11	12	13	14	15	16
Hs (m)	0,5	2	7	13	19	23	27	30	32	33	34	33	33	32
	1	8	28	52	74	94	109	118	118	119	117	110	111	103
	1,5	19	61	116	167	204	227	239	235	230	219	206	200	177
	2	33	108	201	290	337	369	360	351	352	331	320	296	275
	2,5	51	165	299	418	466	508	488	493	464	440	419	382	362
	3		232	412	534	625	636	638	601	565	557	532	463	451
	3,5		294	509	686	770	808	767	773	696	661	633	591	542
	4			608	817	879	939	918	878	849	782	735	680	628
	4,5			695	956	1049	1062	1084	1009	969	910	824	776	703
	5				1070	1145	1259	1229	1134	1119	1000	947	877	833
	5,5				1205	1325	1409	1330	1236	1196	1132	1015	936	872
	6				1343	1560	1564	1478	1391	1278	1268	1154	1018	939
	6,5				1520	1528	1674	1593	1512	1344	1330	1189	1076	1038

Figure 2.10 Power matrix (in kW) for a prototype eight-cell mWave device. Hs is the significant wave height (in meters) and Tp is the peak period (in seconds). Source: Algie et al. (2017).

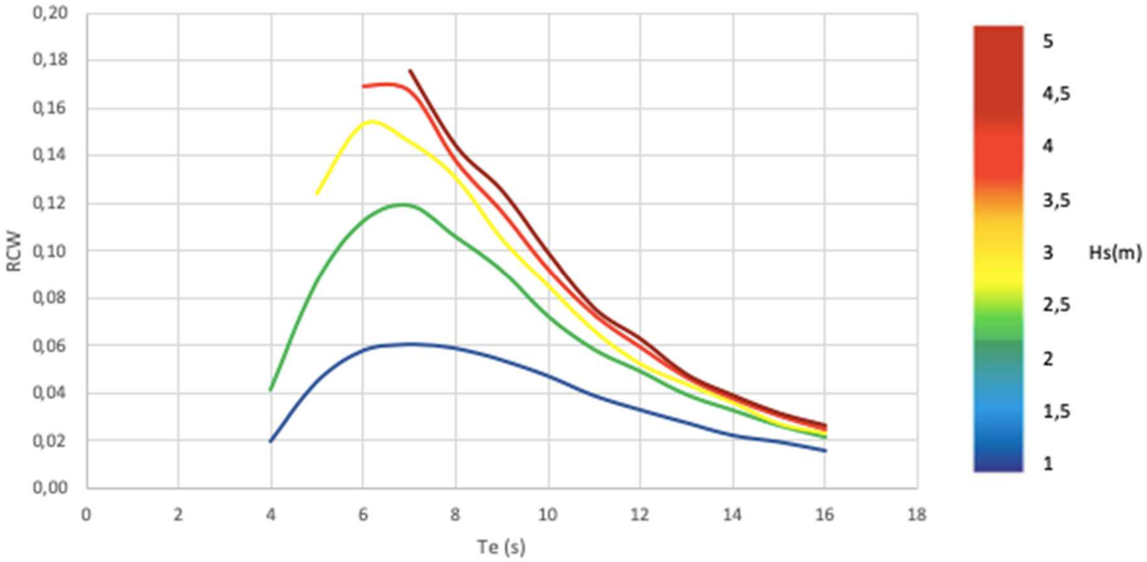

Figure 2.11 Relative capture width curves of a prototype eight-cell mWave device as a function of the energy period (Te in seconds). The colour of the curves indicates the significant wave height for each curve (Hs in meters).

2.5 Numerical modelling

To develop and design a wave energy converter the energy absorption can be studied theoretically and numerically, or by testing a physical model in a wave basin or wave flume. Numerical modelling has to be applied in the first stages of a wave energy plant design since, nowadays, it is the most powerful tool to understand first the ocean waves and then the effects of those technologies on wave characteristics (Thomas & Dwarakish, 2015). Also, models are necessary to compare and evaluate the energy resource at different locations and scales, to inform WEC project developers allowing them to select the most suitable site and achieve optimal power capture and economic performance from their installations.

Wind induced waves are among the most important subjects in coastal and ocean engineering but their random nature makes it one of the most complicated phenomena. The basic physical processes that govern the evolution of wind waves in the open ocean are the input by the wind; nonlinear interactions; white-capping or dissipation in deep-water; bottom dissipation; wave propagation in non-homogeneous media and wave-current interactions (Cavaleri *et al*., 2007).

Studies on wave prediction started in the World War II with the work of Sverdrup, Munk and Traylor (Munk & Traylor, 1947; Sverdrup & Munk, 1946), but their prediction technique was purely statistical and based on the significant wave height. Then, the concept of wave spectrum was introduced in the early 50's (Pierson & Marks, 1952) and in the late 50's the first generation of numerical wave model was developed (Phillips, 1958). Since then a lot of effort has been done to understand the wave propagation and transformation, with the new improved models following this enhanced knowledge. During the progressive development of wave modelling, periods of great theoretical advances have been followed by periods of consolidation and application. Especially with the advent of powerful computers and development of complex numerical techniques, numerical models became a very reliable, cost effective and time saving tool to solve ocean engineering issues.

Numerical models can be used both to forecast and hindcast wave parameters, that is fundamental for the construction and management of offshore structures but also to understand sediment transport processes (Gonzalez-Santamaria *et al*., 2011) and to identify the regions with exploitable wave energy (Rusu & Guedes Soares, 2009; Guedes Soares *et al*., 2014). Usually, for this kind of studies, numerical models are based on the energy balance equation (Hasselmann, 1968), here in a simplified form:

$$\frac{dS(f,x,t,\theta)}{dT} = S_{in} + S_{nl} + S_{dis} \tag{4}$$

where the wave spectrum S is defined over the geographic coordinates x and over time t; it is also depending on the frequency f and propagation direction θ of the waves. Thus, the left part of the equation represents the full derivative of the spectrum with time while on the right part are the three component of the source function: the mechanism of energy exchange between atmosphere and ocean waves, also known as wind-wave interactions source (S_{in}); the energy conservative mechanism of nonlinear wave-wave interactions (S_{nl}); the mechanism of wave energy loss related to wave-breaking processes and interaction of wave with the turbulence of the upper layer, also called dissipation source term (S_{dis}). A more detailed description of the equation used for the present study will follow.

Numerical wave models can be divided into four categories depending on their mechanism: first, second, third and improved third-generation wave models. The first-generation wave models are based on simple wind fields (S_{in}), without accounting for energy losses (S_{dis}) and nonlinear interactions (S_{nl}) among distinct frequencies, that is why they are also referred as decoupled models. A two-dimensional wave spectrum (frequency-direction) evolves when the wind forcing reaches a saturation level that is defined by a universal equilibrium distribution, and each spectral component propagates with its group velocity (Caetano & Innocentini, 2003).

The second-generation wave models are developed using varying wind fields and nonlinear interactions that are simplified and parametrized to a certain spectral distribution of energy, that is why those models are called parametric models (Hasselmann *et al*., 1976). In those models, the swell is represented explicitly by the spectrum and the wind sea by parameters. In general, the spectral shape assumed is the JONSWAP distribution (Hasselmann *et al*., 1973).

The need for a better resolution on the wave models in coastal regions lead to the development of the third-generation numerical models. They use the energy balance equation to describe the time and space evolution of the wave spectrum, that propagates freely without any imposition on its shape (Tolman & Chalikov, 1996). An example is the WAM (WAve Modelling) model (The Wamdi Group, 1988) that uses a parameterization of the non-linear transfer source function to save computational time. With time, many other wave models appeared to improve the limitations of the WAM model regarding the non-linear transfer of energy (Hasselmann *et al*., 1985). The most notable are SWAN (Simulating WAves Nearshore) (Booij, N., 1999) and WAVEWATCH III (Tolman, 1989).

In general, third-generation wave models can be divided into two types (Battjes, 1994): phase resolving and phase averaging models. Phase resolving wave models are then divided depending on the equations applied: Hamiltonians equations, Boussinesq equations or mild-slope equations. This type of models describes the sea surface as a function of space and time and are used for rapidly varying wave conditions. They can simulate the sea surface elevation with high accuracy, taking implicitly into account several physical phenomena: refraction, diffraction, quadruplets wave-wave interactions, dissipation effects (such as bottom friction and depth induced breaking effects). But, they do not consider wind as a generation process and they are computationally very demanding.

Phase averaging models describe the irregular sea surface by a spectral energy density function and are used for applications on large scale. Two methods can be applied within those models: the Lagrangian approach and the Eulerian approach. In the first approach, waves are propagated from deep to shallow waters independently by transporting the wave energy along wave rays, which makes the computation of nonlinear effects numerically inefficient. This may generate chaotic wave rays patterns that are difficult to interpret. In the second approach, the wave propagation occurs on a grid where every grid point has the information of the whole spectrum. Thus, the problem of chaotic wave patterns is avoided and the inclusion of generation, dissipation and nonlinear wave-wave interactions can be done efficiently. The earlier models for numerical wave prediction not only simplified ocean wave characteristics but also used coarse grids. That might be suitable for deep regions, but for accurately model coastal regions a finer mesh is needed. This lead to new third-generation numerical models, such as MIKE21 SW (Sørensen *et al*., 2004).

2.5.1 SWAN model

The third-generation spectral wave model SWAN (acronym for Simulating WAves Nearshore) was developed by the Delft University of Technology from the WAM model, to improve the accuracy of spectral wave modelling in the nearshore zone. The SWAN model is fully spectral in frequencies and directions (0°-360°) and it computes random, short-crested wind-generated waves in coastal regions. It is an open-source phase averaging model that uses the Eulerian approach and efficiently represent the processes of waves generation, spatial propagation, shoaling and refraction due to bottom variations. It includes additional functionalities such as triad wave-wave nonlinear interactions and depth-induced wave breaking. It is based on the action balance equation, which for small-scale simulations can be expressed in Cartesian coordinates as follows:

$$\frac{\partial N}{\partial t} + \frac{\partial}{\partial x}(c_x N) + \frac{\partial}{\partial y}\left(c_y N\right) + \frac{\partial}{\partial \sigma}(c_\sigma N) + \frac{\partial}{\partial \theta}(c_\theta N) = \frac{S_{tot}}{\sigma} \tag{5}$$

where $N(\sigma, \theta)$ is the wave action density (given by the energy spectral density $E(\sigma, \theta)$ over the relative frequency σ); t is the time; θ is the wave direction; c_x, c_y, are the propagation velocities in the geographical x-y space; and c_σ and c_θ are the propagation velocities in the spectral space (frequency and directional space).

The first term on the left is the local rate of change of action density in time; the second and third terms are the propagation of action in the geographical space; the fourth term represents the shifting of action density in frequency space due to variations in depth and currents; the fifth term reproduces depth-induced and current-induced refraction.

The source term $S_{tot}(\sigma, \theta)$ on the right side of the action balance equation accounts for the effects of energy generation and dissipation. More explicitly, the source terms in SWAN include wave energy growth by wind input S_{in}, wave energy transfer due to wave-wave non-linear interactions S_{nl} and dissipation of wave energy (S_{dis}) due to whitecapping (Komen *et al.*, 1984). The wave-wave interaction is modelled through the quadruplet mechanism (Hasselmann *et al.*, 1985) in deep waters, and of triads (Eldeberky, 1996), in shallow water. In some cases, linear wind-input S_{ln} can also be considered. In shallow waters, additional processes have to be considered, most notably wave-bottom interactions S_{bot} (Madsen *et al.*, 1989). In extremely shallow waters, depth-induced breaking S_{db} (Battjes & Janssen, 1978) and triad wave-wave interactions S_{tr} (Eldeberky, 1996) become also important. So that the net source function S_{tot} is defined by:

$$S_{tot} = S_{in} + S_{nl} + S_{dis} + S_{ln} + S_{bot} + S_{db} + S_{tr} \tag{6}$$

According to the SWAN Scientific and Technical documentation (SWAN, 2018), the following wave propagation processes are represented in the model:

- Propagation through geographic space;
- Refraction due to spatial variations in bottom and current;
- Diffraction (in an approximate way);
- Shoaling due to spatial variations in bottom and current;
- Blocking and reflections by opposing currents;
- Transmission through, blockage by or reflection against obstacles.

The following wave generation and dissipation processes are represented in SWAN:

- Generation by wind;
- Dissipation by white capping;
- Dissipation by depth-induced wave breaking;
- Dissipation by bottom friction;
- Wave-wave interactions in both deep and shallow waters.

Since diffraction is modelled in a restricted sense, the model should be used in areas where variations in wave height are large. Since the computation of diffraction in arbitrary geophysical conditions is complicated and requires considerable computing effort, a phase-decoupled approach is employed (Holthuijsen *et al.,* 2003) to obtain the same qualitative behaviour of spatial redistribution and changes in wave direction.

In any case, the model requires bathymetric information, initial conditions, boundary conditions, and possibly atmospheric forcing conditions (pressure and wind fields) and ocean forcing (current fields and tide levels). To increase the precision of the predictions in the zone of interest, SWAN uses a mesh nesting scheme, in which the results obtained for a large computational domain are used as border condition for a smaller domain, but with higher resolution.

The model can be run both in serial mode, i.e. one SWAN program running on one processor, or in parallel mode, i.e. on a shared memory system or distributed memory machines. In this case study, to reduce the computational time when simulating the waves for larger periods the model was run in parallel using Medusa cluster infrastructure, available at the National Laboratory of Civil Engineering (LNEC) of Lisbon.

Once the model is running an accuracy criteria is set to terminate the iterative computations. In particular, SWAN stops the iteration if:

a) The change in the local significant wave height (H_s) from one iteration to the next is less than:

- a relative change fraction of that wave height or

- a relative change fraction with respect to mean value of the average significant wave height (averaged over all wet grid points);

b) and if the change in the local mean wave period (T_{m01}) from one iteration to the next is less than:

- a relative change fraction of that period or
- a relative change fraction with respect to the mean value of the average mean wave period (averaged over all wet grid points);

c) and if the conditions a) and b) are fulfilled in more than a percentage of wet grid points %.

The default value of the relative change is 0.02 for both H_s and T_{m01} and the default value for the percentage of wet grid points is 98%. It is also possible to terminate the iterative procedure by giving the maximum number of iterations after which the computation stops.

The SWAN model has been widely used to assess the changes in shoreline wave climate caused by the installation of a wave farm. Here are some cases that used SWAN for WEC's impact assessment: the Wave Hub wave farm off the north coast of Cornwall (Gonzalez-Santamaria *et al.*, 2013; Millar *et al.*, 2007; Smith *et al.*, 2012); the WaveRoller (Rusu *et al.*, 2016) and Pelamis (Rusu & Soares, 2013) both north of Peniche; a Pelamis (Palha *et al.*, 2010) and a generic wave farm in Sao Pedro de Moel in Portugal (Bento *et al.*, 2014); a generic wave farm in the Galician coast of Spain (Iglesias & Carballo, 2014); a generic wave farm in Monterey Bay and Santa Cruz in California (Chang *et al.*, 2014a).

2.5.2 SWAN model input

According to the User Manual by the SWAN team (available online at http://swanmodel.sourceforge.net/online_doc/swanuse/swanuse.html) the user should provide SWAN with several input files with the following information:

- a file containing the instructions of the user to SWAN (the command file);
- file(s) containing: grid, bottom, current, friction, and wind (if relevant);
- file(s) containing the wavefield at the model boundaries (if relevant).

To construct the input files necessary to run the SWAN execution file (version 41.20AB), a Microsoft Access database was used. This database constructs an input file for SWAN for each grid and wave condition by processing the input that the user fills into the database. Once those INPUT files are produced, they must be placed in the same directory with the bathymetry and the executable file before running SWAN. SWAN is quite flexible with respect to output processing: the output is available for many different wave parameters. However, generally the output is produced by SWAN only at the user's request and the instructions of the user to control output are divided into three categories:

- definitions of the geographic location(s) of the output. The output locations may be either on a geographic grid, along user specified lines (e.g., a given depth contour line) or at individual output locations;
- times for which the output is requested (only in nonstationary runs);
- type of output quantities (wave parameters, currents or related quantities).

2.5.3 SWAN model output

In the present study, two categories of output in the SWAN model were obtained: a file which presents the results of the model for a set of output locations and/or a data file which contains the values of several spectral parameters at all computational grid points. manual (SWAN, 2018) presents a complete description of the output variables of the SWAN model. Here reported are the ones chosen for this study:

- Geographic coordinates: longitude and latitude (in meters since Cartesian) of each computational grid point in ETRS89/Portugal TM06 (EPSG:3763) Coordinate Reference System;
- Significant wave height: denoted as H_s in meters, and defined as

$$H_s = 4\sqrt{\iint E(\omega,\theta)d\omega d\theta} \tag{7}$$

  where $E(\omega,\theta)$ is the energy density spectrum and ω is the absolute radian frequency;

- Mean absolute wave period: denoted as T_{m01} in seconds, and defined as

$$T_{m01} = 2\pi(\frac{\iint \omega E(\sigma,\theta)d\sigma d\theta}{\iint E(\sigma,\theta)d\sigma d\theta})^{-1} \tag{8}$$

  where σ is the relative frequency;

- Mean absolute zero-crossing period: denoted as T_{m02} in seconds, and defined as

$$T_{m02} = 2\pi(\frac{\iint \omega^2 E(\sigma,\theta)d\sigma d\theta}{\iint E(\sigma,\theta)d\sigma d\theta})^{-1/2} \tag{9}$$

- Mean wave direction: denoted ad Dir in ° and nautical convention (i.e. the direction where the waves come from, measured clockwise from geographic North), and defined as

$$Dir = arctan\left[\frac{\int sin\theta E(\sigma,\theta)d\sigma d\theta}{\int cos\theta E(\sigma,\theta)d\sigma d\theta}\right] \tag{10}$$

- Peak direction: denoted as PkDir and is the peak direction of $E(\theta) = \int E(\sigma,\theta)d\sigma$ in ° and nautical convention;

- Relative peak period: denoted as RTP in seconds and equal to absolute peak period in the absence of currents;
- Depth: value in meters of the depth contour line along which output locations are generated by SWAN.

Moreover, SWAN always creates a print file that contains an echo of the command file, an overview of the physical and numerical parameters used in the simulation run and self-explanatory warning and error messages.

In Table 2.3 are reported in summary the input and outputs used for the simulations performed with SWAN in the context of the present work. The output from the Microsoft Access database are the input files for SWAN.

Microsoft Access input	Microsoft Access output/ SWAN input	SWAN output
- Computational grids - Bathymetry grids - Spectrum resolution - Physical processes - Stationary wave conditions - Output specifications	- Bathymetry files (.BOT) - INPUT files - Command file (.BAT)	- Output points files (.dat) - Output grid files (.dat) - PRINT file

Table 2.3 Input and output files of Microsoft Access database and of SWAN.

2.5.4 SNL-SWAN model

A modified version of the standard SWAN was developed, the SNL-SWAN (Ruehl *et al.*, 2013; Ruehl *et al.*, 2014) by the Sandia National Laboratories to evaluate WEC farm effects on wave propagation. For that, a WEC module with five different options (referred to as obstacle cases or OBCASE), that accounts for device-specific WEC power performance was developed. Based on the user specified power performance, SNL-SWAN calculates the associated transmission coefficient (K_t), which describes the ratio of wave height transmitted through a WEC array over that incident upon it.

In detail, to model WECs in SWAN, the OBSTACLE feature is used. It defines the obstacle as a line crossing between two grid points, with a transmission coefficient that acts as an energy sink in the wave action balance equation (5), extracting a fraction of the incident wave energy (Ruehl *et al.*, 2015).

2.5.4.1 WEC module

The modifications made to SNL-SWAN compared to SWAN allow the code to calculate realistic energy extraction terms based on existing WEC power performance data. The implication of the code modifications is that wave farms will be more realistically modelled, resulting in more confidence in the observed environmental effects from deployment of WEC arrays (Ruehl *et al.*, 2015).

Thus, the capacity of a WEC to extract energy from waves is parameterized according to the characteristics of the sea state, or as a function of the wave height and wave period of each spectral component. From the SNL-SWAN user's manual (Ruehl *et al*., 2014) the five possible options in the WEC module are:

OBCASE 0) It is the baseline SWAN OBSTACLE formulation in which the transmission coefficient is a constant value entered into the SWAN input file and applied across all wave frequencies. It represents the ratio of wave heights incident to (H_{inc}) and in the lee (H_{lee}) of the WEC:

$$K_t = \frac{H_{lee}}{H_{inc}} \tag{11}$$

Therefore, a coefficient of 1.0 provides 100% transmission, and a coefficient of 0.0, total blockage. There are several limitations of using this approach to model WECs. First of all, the SWAN OBSTACLE formulation extracts a constant amount of energy from each incident wave period (or binned frequency) but, in reality, WECs are designed to extract more energy at some sea states and less at others. Additionally, WECs are often controlled to maximize energy extraction by tuning the WEC energy conversion with incident wave climate (Kulia *et al.*, 2017; Oskamp & Özkan-haller, 2012). Moreover, due to the variety of existing WEC technologies, there is significant variation in the power performance of different devices due to factors such as power rating, bandwidth, directional dependence, and control (Babarit *et al*., 2012). All of these factors influence the energy extraction of WECs, and thus the transformation of waves through WEC arrays and influence on near-field and far-field environmental effects. None of these factors are captured in the baseline SWAN formulation. This is the reason why modifications were made to SWAN v41.01 (referred to as SNL-SWAN) to improve modelling of WECs and the following additional OBCASEs have been implemented (Ruehl *et al.*, 2015).

OBCASE 1) The transmission coefficient is computed by SNL-SWAN from a user-defined WEC power matrix (Figure 2.7 and Figure 2.10). A power ratio is calculated at the peak wave period based on the absorbed wave power (P_{abs}) from the WEC power matrix and the incident wave power (P_{inc}), then the transmission coefficient, calculated as shown in Eq. (12), is applied as a constant value across all wave frequencies.

$$K_t^2 = 1 - \frac{P_{abs}}{P_{inc}} \tag{12}$$

<u>OBCASE 2)</u> SNL-SWAN computes the transmission coefficient from a user-supplied WEC relative capture width (RCW) curve (Figure 2.8 and Figure 2.11). Given the peak incident wave period and the RCW value the transmission coefficient, calculated as shown in Eq. (3), is applied as a constant value across all wave frequencies.

$$K_t^2 = 1 - RCW \tag{13}$$

<u>OBCASE 3)</u> This is an extension of OBCASE 1, but distinct transmission coefficients are applied to each binned wave frequency based on the WEC power matrix.

<u>OBCASE 4)</u> This is an extension of OBCASE 2, but the RCW curve is sampled independently for each binned wave frequency, resulting in a frequency dependent obstacle transmission coefficient.

OBCASE 3 or 4 are only appropriate when there are available information about individual frequencies, while OBCASE 1 and 2 are more appropriate when information is available about average sea states.

Previous studies have already used SNL-SWAN to evaluate WEC farm effects on wave propagation, such as in the California coast in Monterey Bay and Santa Cruz (Chang *et al.*, 2016; Chang *et al.*, 2014b; Ruehl *et al.*, 2015), in Canada offshore Vancouver Island (Luczko *et al.*, 2016), in Western Australia near Perth (Contardo *et al.*, 2018), in Portugal in Aguçadoura (Monteiro, 2017).

2.5.4.2 Modelling of obstacles

As reported in Section 2.6 of SWAN Scientific and Technical Documentation (SWAN, 2018), SWAN can estimate wave transmission through a line-structure if it is possible to assume that the obstacle is narrow compared to the grid size. This kind of obstacle affects the wavefield in three ways:

- it reduces the wave height of waves propagating through/over the obstacle all along its length,
- it causes waves to be reflected, and
- it causes diffraction around its end(s).

Since obstacles usually have a transversal area that is too small to be resolved by the bottom grid both in SWAN and SNL-SWAN, an obstacle is modelled as a line in the computational area (Figure 2.12).

To calculate the action density flux from one grid point to its neighbours, SWAN first determines if the connecting grid line crosses an obstacle line. If a grid line is crossed by an obstacle line, the transmission coefficient is applied to the flux between those nodes.

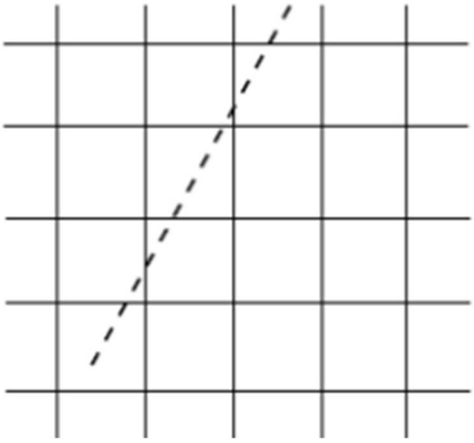

Figure 2.12 Obstacle line cutting through a computational grid. Source: SWAN (2018).

SWAN uses a vertex centred grid, with volume cells defined by grid centres (Figure 2.13). The finite volume cell edges are the fluxing faces between neighbouring vertices. This grid treatment in combination with SWAN's obstacle treatment has some implications about the various ways in which obstacles can interact with the computational grid.

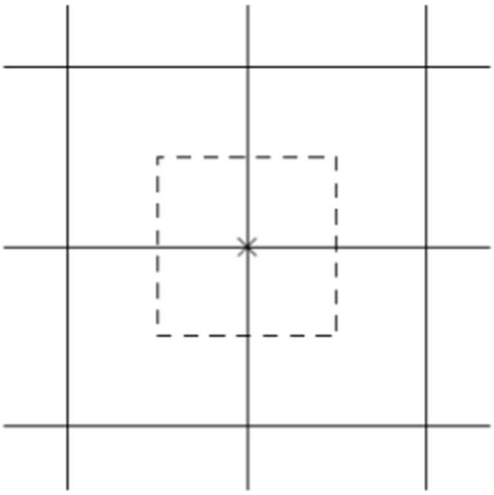

Figure 2.13 Computational grid (solid lines), a grid vertex and the finite volume cell corresponding to that vertex (dashed lines). Source: SNL-SWAN user's manual Ruehl et al*. (2014).*

For instance, if two lines have different length but they both cross the same computation grid line (such as the two blue lines shown in Figure 2.14), they have the same influence on the model solution. If a line does not intercept the computational grid due to grid discretization, that obstacle will have no effect (such as the green line in Figure 2.14). The red line in Figure 2.14 represents the appropriate use of the obstacle, where grid discretization is much finer than the obstacle length. Since the obstacle spans multiple grid lines, its length and transmission effects can be properly captured. This is how each obstacle has been implemented in the simulations performed for the present study. In particular, the WaveRoller type devices are 25 m long and in a computational grid with 25 m resolution they would cross once or twice the computation lines. While the Bombora’s mWave type is 75 m long, therefore it will cross even more computation lines.

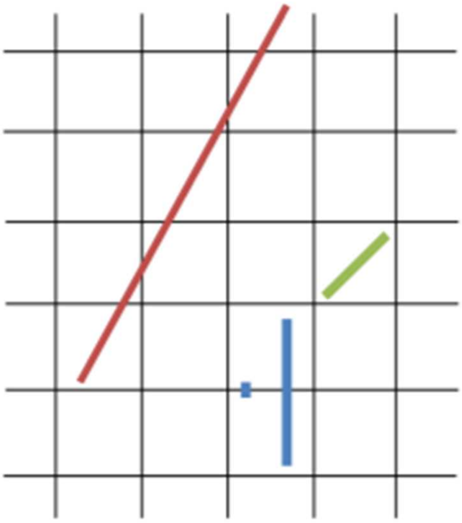

Figure 2.14 Examples of obstacle lines cutting through a computational grid. Source: SNL-SWAN user’s manual Ruehl et al. (2014).

2.5.4.1 SNL-SWAN input and output

In order to run SNL-SWAN simulations the INPUT files of SWAN must be modified by adding new lines with the following commands:

- “SET inrhog=” followed by the number 1 to indicate that the user requires output based on true energy;
- “SET obcase=” followed by the number of OBCASE (0, 1, 2, 3 or 4);
- “OBSTACLE TRANS 0.00 REFL 0.00 LINE” followed by the coordinates (in the coordinate system EPSG:3763 ETRS89 / Portugal TM06) of the first and last point of the line representing the obstacle. If OBCASE 0 is used the transmission coefficient (TRANS) must be specified. If OBCASEs 1 or 3 are selected a Power.txt file must be constructed with the power matrix of the specific WEC device considered and it must be in the same directory as the INPUT files before running SNL-SWAN. If instead OBCASE 2 or 4 are selected an RCW file named Relative_Capture_Width.txt is needed.

In addition to user-specified outputs, SNL-SWAN supplies POWER_ABS.OUT. This file provides absorbed power for each modelled WEC (obstacle). For more details, an online tutorial is provided by the Sandia National Laboratories (http://snl-waterpower.github.io/SNL-SWAN/tutorial.html).

3 | Application of SNL-SWAN model without devices to Almagreira beach

3.1 Introduction

Recent assessments of wave energy potential in the Atlantic Ocean showed that there are some promising areas along the Portuguese coast for wave energy exploitation (Castro-Santos *et al.*, 2018; Gleizon *et al.*, 2017; Silva *et al.*, 2018).

One of these areas is the Almagreira beach north of Peniche, briefly described in section 3.2. This place is a selected area for wave farms installation, where a WaveRoller oscillating wave surge converter was already tested since 2007 and at the present moment a full-scale wave farm installation is previewed.

To simulate the wave propagation in Almagreira beach and the impact of a wave farm on its wave climate, it is necessary to set up and adjust the SNL-SWAN wave model to the specific case of the present study. Therefore, the following preliminary steps have been accomplished and are presented in the present chapter:

- a comparison of the SNL-SWAN model outputs against the in-situ data from the "Nazaré Costeria" buoy, in terms of significant wave height, peak period and mean direction (section 3.3);
- a characterization of the wave climate offshore and nearshore Almagreira beach without the devices, which was performed for a period of 19 years (from 2000 to 2018) and is reported in section 3.4. From that, the most common and energetic sea states have been selected and used as an input to perform the simulations with the wave farm in the following chapter 4 |, which is the main objective to this chapter.

3.2 Almagreira beach

The study area is located nearshore Praia de Almagreira, on the west coast of Portugal in the municipality of Peniche. Peniche is located in the Oeste subregion, with an area of 77.55 km^2 and a total population of 27,753 in 2011 (INE, 2018). Besides tourism, the economy of the Peniche municipality relies on agriculture, services and fishing. In fact, since ancient times it has been an important fishing harbour. Moreover, since 1998 the area of Peniche and Santa Cruz is a Natura 2000 Site of Community Importance (SCI) with the ID: PTCON0056. This SCI covers a wide coastline with high landscape diversity and is characterized by the alternation between dune and cliff systems, supporting an important biodiversity. It includes stretches of rocky and sandy coastline and a complex of coastal wetlands with great biological and geomorphological diversity.

The beaches of Peniche are popular and famous for recreational activities and sports such as surfing, windsurfing, bodyboarding and kite surfing. In particular, Peniche is considered one of the best surfing locations in Europe because it has beaches and breaks facing three distinctly different directions so that there is always a beach which faces the best swells. It is home to many surf camps/schools, it annually hosts the MEO Rip Curl Pro Portugal from the World championship tour of the World Surf League (WSL) at the Supertubos beach (Nunes *et al.*, 2018). In Figure 3.1 are represented the main surf spots of Peniche and among them is Praia de Almagreira, a very long sandy beach on bathed by the Atlantic Ocean for about 1.5 km.

The western Portuguese coast is well exposed to the North Atlantic wave regime and is characterized by a predominant North-West swell and a wider directional spread (South-West to North) of other less energetic waves. Almagreira beach is therefore nearly perpendicular to the prevailing swell. The offshore incident wave regime is characterized by an average significant wave height (Hs) of 2-2.5 m, wave periods of 9-11 s corresponding to WNW to NNW swell (Bosnic *et al*., 2014; Dodet *et al*., 2010). Storms are frequent between October and March and typically raise 6–9 m-high waves along this coast (Costa & Esteves, 2010).

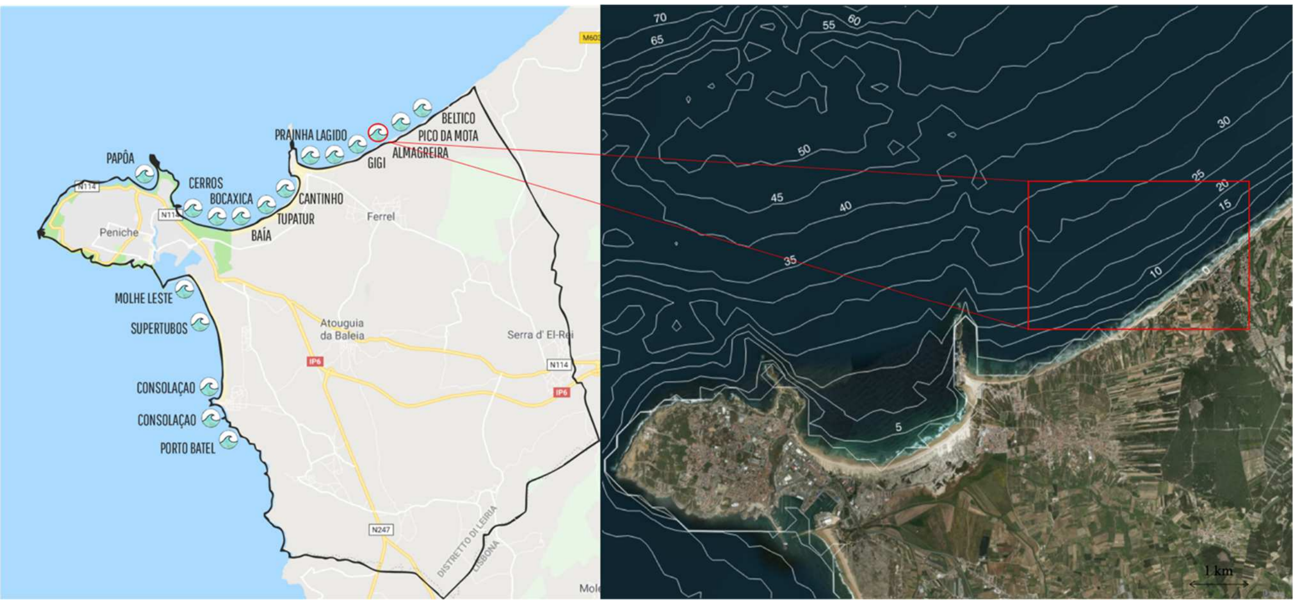

Figure 3.1 Map of the surf spots in Peniche with Almagreira beach among them (left) and bathymetry of the study area location nearshore Almagreira beach (right).

3.3 Comparison with Nazaré wave buoy data

It is of crucial importance to evaluate the performance of numerical codes such as SNL-SWAN that are used to model WEC arrays and predict environmental effects instead of direct measurements from wave farm deployments. Previous studies (Ruehl *et al.*, 2015; Ruehl *et al.*, 2013) have already performed a comparison of SNL-SWAN results with related spectral wave models (the EMS, Exeter

Modified SWAN) and with WEC array experimental data, gathered by Columbia Power Technologies at Oregon State University.

However, for the present study area (Almagreira beach) no previous studies or WEC data were available that could be used to analyze the performance of the SNL-SWAN model. The only available data are the wave data collected by the Instituto Hidrografico (http://www.hidrografico.pt/boias) with the buoy “Nazaré Costeira” (MONICAN2, 90 m mooring depth), located north of Peniche (39°33.6' N, 9°12.6' W).

For this reason, it was decided to first evaluate the SNL-SWAN, only in terms of wave propagation simulations without considering any devices. In this case, SNL-SWAN wave propagation calculations refer to the native SWAN code for cases without obstacles, therefore this preliminary test was accomplished using the native SWAN model.

With SWAN the deep-water waves propagation from offshore to shallow water was simulated in the study site. The input boundary wave values of SWAN (offshore wave characteristics) were taken from the ECMWF database (https://www.ecmwf.int/en/forecasts/datasets), namely, the significant wave heights, peak periods and wave directions from 2000 to 2018 at a selected offshore point of the Almagreira beach. The output wave conditions (significant wave height H_s, mean wave period T_{m01}, peak period T_p, mean direction Dir_m, peak direction Dir_p) were compared with the data collected by the Instituto Hidrografico (http://www.hidrografico.pt/boias) with the buoy “Nazaré Costeira”.

In the next subsections, the set-up of SWAN or SNL-SWAN model without obstacles is presented, as well as the results of the simulation of wave propagation from offshore to the Nazaré buoy (north of Peniche), near Almagreira beach.

3.3.1 Model set-up

The bathymetric data from Almagreira site were taken from EMODNet (European Marine Observation and Data Network) website (http://www.emodnet-hydrography.eu or http://portal.emodnet-bathymetry.eu) that provides fine-resolution bathymetries.

The 2018 version of the EMODnet digital terrain model (DTM) has been created at a grid resolution of 1/16 * 1/16 arc-minutes (circa 115 * 115 m) using the best available bathymetry data sets from several data providers (plummets, single beam, multi-beam, LIDAR observations, composite Digital Terrain Models, Satellite Derived Bathymetry). Despite this, there are still areas where high-quality bathymetry data is not available that have been filled with the GEBCO Digital Bathymetry 2014 at 30 arc-second global interval grid.

The choice of the geographical computational grid plays a crucial role in wave model simulations. A standard approach is a regular mesh with additional runs on a nested mesh to decrease the overall computational demand. Therefore, in this case, two nested grids were constructed since they showed to decrease the computational time even more. Moreover, changing the resolution changes the speed of the run, so that lower resolution means faster runs. Therefore, to perform the SWAN model simulations nearshore Almagreira beach a three-nested model domain was employed, similar to that presented in a previous study by Silva *et al*. (2016).

The three grids employed are regular and rectangular. The main grid and first nested-grid have a bathymetry resolution of 103.16 m in latitude and longitude, while the second nested-grid has a resolution of 30 m. All of them are Cartesian grids in nautical coordinates (Figure 3.2). The bathymetry of the second nested grid (30 m x 30 m) has been generated by interpolating in QGIS the coarse resolution grid (103.16 m x 103.16 m) with a higher resolution grid of 20 m x 20 m (Figure 3.3) available on EMODnet bathymetry viewing and download service only for a nearshore area of Almagreira of around 3 km length and wide 1.5 km. The geodetic system of those grid was WGS84 and has been transformed into the projected coordinate system for Portugal (EPSG:3763 ETRS89/Portugal TM06).

A resume of the characteristics of the bathymetric grids used as well as the correspondent parameters needed for SWAN and SNL-SWAN to simulate the wave propagation can be found in Table 3.1, while the characteristics of the computational grids can be found in Table 3.2.

Bathymetric grids	Main Grid	Nested Grid	Nested Grid 1
X initial (Longitude)	-137259.34	-137259.34	-104583.25
Y initial (Latitude)	-67313.33	-67313.33	-33216.34
Grid rotation (°)	0	0	0
n° DX	574	574	174
n° DY	721	721	156
DX (m)	103.16	103.16	30
DY (m)	103.16	103.16	30

Table 3.1 Characteristics of SNL-SWAN bathymetric grids. The initial X and Y refer to the bottom left corner (coordinate system EPSG:3763 ETRS89 / Portugal TM06) of the grid. DX and DY refer to the cell size.

Computational grids	Main Grid	Nested Grid	Nested Grid 1
X initial (Longitude)	-137259.34	-110702	-104523.26
Y initial (Latitude)	-67313.33	-34626	-33036.34
Grid rotation (°)	0	0	0
Grid length in x direction (m)	59210	17500	3570
Grid length in y direction (m)	74380	16510	2590
DX (m)	500	250	100
DY (m)	500	250	100
Number of meshes in x direction	118	70	36
Number of meshes in y direction	149	66	26

Table 3.2 Characteristics of SNL-SWAN computational grids. The initial X and Y refer to the bottom left corner (coordinate system EPSG:3763 ETRS89 / Portugal TM06) of the grid. DX and DY refer to the cell size.

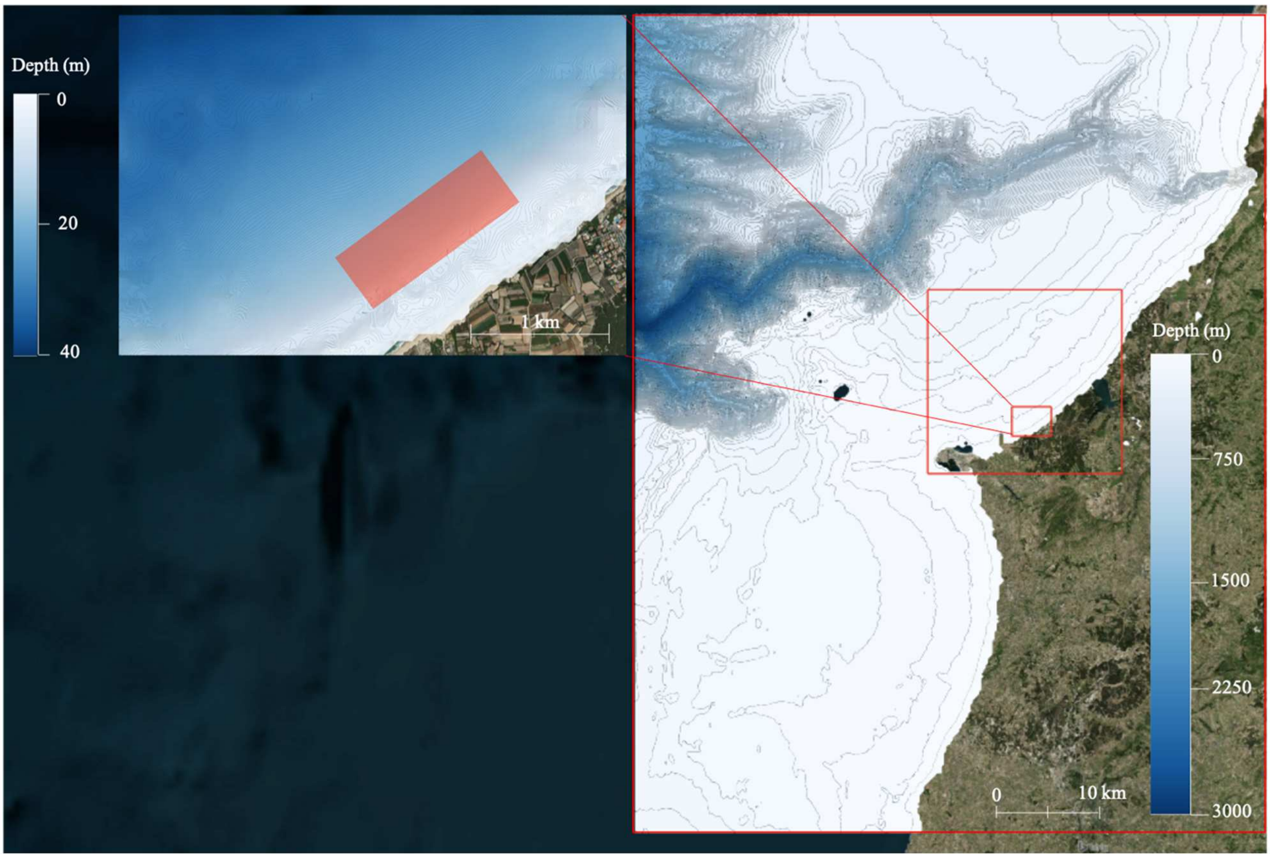

Figure 3.2 Bathymetry grids for SNL-SWAN simulations with scale in meters. The main grid and first nested grid have a bathymetry resolution of 103.16 m (right) while the second nested grid has a bathymetry resolution of 30 m (left). The approximate location of the WECs farm is also reported (red rectangle).

Figure 3.3 Computational grids for SNL-SWAN simulations: the most external one is the main grid and the two insides are the nested grids. The points were the wave climate has been characterized are reported (yellow circles) along with Nazaré Costeira buoy.

The model was run in a stationary mode, which means with constant meteorological and hydrodynamic conditions at the offshore boundaries. Directional wave energy spectra conditions were exported from the coarse resolution model and used as boundary conditions for the first nested grid, and the conditions used in the SWAN model of the first nested grid were then exported and used for the second nested fine resolution grid. The nested grid models were also implemented as stationary models.

The SWAN initial wave conditions were extracted from ECMWF database at the point located at the top left corner of the main grid (Figure 3.3) and at a depth of around 1700 m (with coordinates -8°7'59.599" W, 39°40'7.017"N, EPSG:4326 WGS 84 coordinate system). The offshore wave data corresponds to the values of significant wave height, peak period and wave direction from the period between 2010 and 2018. This was the available period of Nazaré Costeira wave buoy data of the Portuguese Instituto Hidrográfico (http://www.hidrografico.pt/m.boias).

Moreover, it has been proved from previous studies that in the area of Almagreira beach not only the wind intensity and direction but also the tide level may significantly influence the wave characteristics (Silva *et al.*, 2016). Therefore, the tide must be included in the model inputs for the simulations and it was extracted with WXTide32, a Windows tide and current prediction program that predicts tides worldwide from 1970 through 2037.

A JONSWAP spectrum with default parameters was considered. The frequency resolution was 31 logarithmically spaced frequencies between 0.04 and 1 Hz. SWAN was run with default bottom friction coefficient, diffraction turned on, triad wave-wave interactions turned on and quadruplet wave-wave interactions turned off. For this test, the model was run in parallel for a period of 9 years (from 2010 to 2018) using the high-performance Linux cluster MEDUSA cluster, available at the National Laboratory of Civil Engineering (LNEC) of Lisbon. This is part of the National High-Computing Performance Network (RNCA in Portuguese), a high-computing facility linking four research institutes and universities in Portugal and aiming at meeting the high-computing needs of researchers in such field as fluid dynamics, physics or data mining.

3.3.2 Results

The SWAN computed values of significant wave height (H_s), mean period (T_{m01}), mean direction (Dir_m) and also peak period (T_p) and peak direction (Dir_p) were compared with the measured values at the Nazaré Costeira buoy site for the period between 2010 and 2018. The major problem encountered during the model validation were the missing data from buoy measurements, as can be seen from the time series of significant wave height modelled values and buoy values (Figure 3.4).

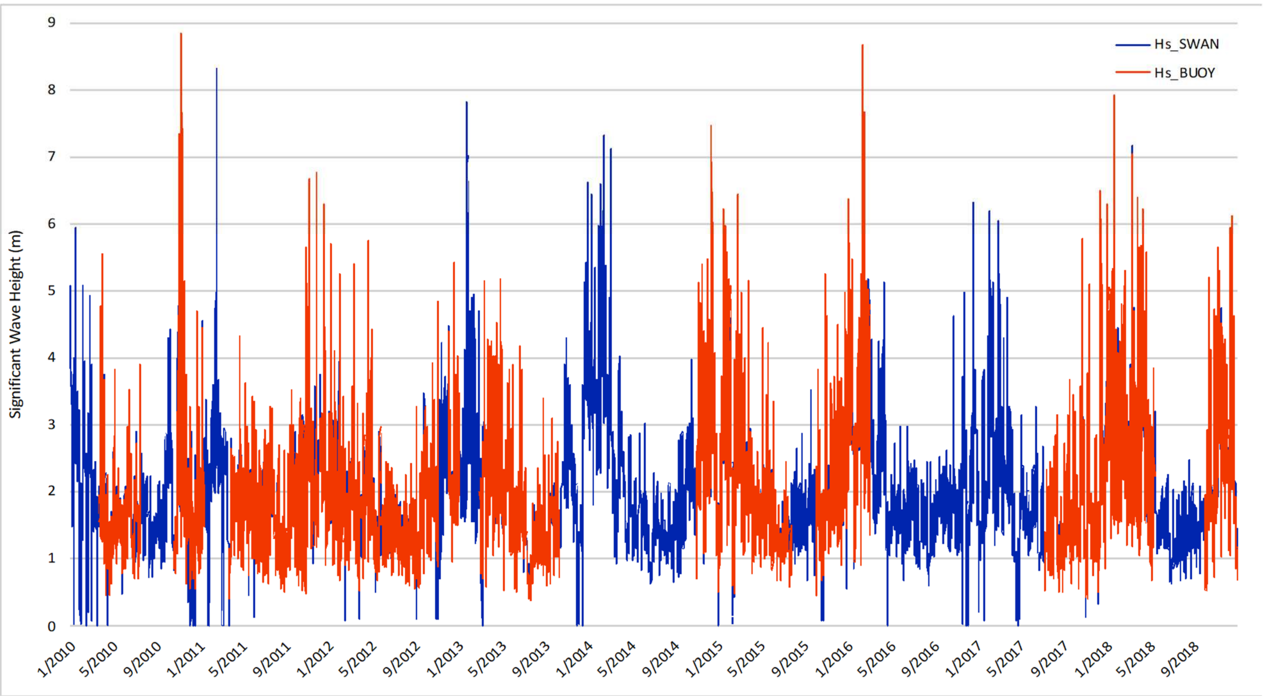

Figure 3.4 Time series of significant wave height (in meters) for the period between 2010 and 2018. Both the modelled values (in blue) with SWAN parallel runs and the measured values (in orange) from the "Nazaré Costeira buoy" (from the Portuguese Instituto Hidrografico) are represented.

The statistical parameters used to compare the SWAN simulations with the data from the buoy were the average value of measurements ($\bar{X}$) and of simulations ($\bar{Y}$) with their standard deviations (s_X and s_Y), the Root Mean Square Error (RMSE), the Bias, the Scatter Index (SI) and the correlation coefficient (r), being calculated with the formulations presented below:

$$\bar{X} = \frac{\sum_{i=1}^{n} X_i}{n} \tag{14}$$

$$\bar{Y} = \frac{\sum_{i=1}^{n} Y_i}{n} \tag{15}$$

$$s_X = \sqrt{\frac{\sum_{i=1}^{n}(X_i - \bar{X})^2}{n}} \tag{16}$$

$$s_Y = \sqrt{\frac{\sum_{i=1}^{n}(Y_i - \bar{Y})^2}{n}} \tag{17}$$

$$RMSE = \sqrt{\frac{\sum_{i=1}^{n}(X_i - Y_i)^2}{n}} \tag{18}$$

$$Bias = \frac{\sum_{i=1}^{n}(X_i - Y_i)}{n} \tag{19}$$

$$SI = \frac{RMSE}{\bar{X}} \tag{20}$$

$$r = \frac{\sum_{i=1}^{n}(X_i - \bar{X})(Y_i - \bar{Y})}{\sqrt{\sum_{i=1}^{n}(X_i - \bar{X})^2 \sum_{i=1}^{n}(Y_i - \bar{Y})^2}} \tag{21}$$

where X_i corresponds to measured values, Y_i to simulated values and n is the number of points used.

Looking at the statistical results presented in Table 3.3, it can be seen that the correlation coefficient between the data is high, particularly for the H_s and Dir_m parameters.

The Bias presents also good results, with the worst value for the peak direction (-0.44). A negative Bias means that the model overestimates the real data while a positive Bias means that the model underestimates it. Even if for the peak direction the results were not so good, nevertheless, the overall numerical results showed good agreement with the experimental ones.

	$\bar{X}$	$\bar{Y}$	s_X	s_Y	RMSE	Bias	SI	r
H_s	2.07 m	2.09 m	1.07 m	0.93 m	0.38 m	-0.02 m	0.18	0.94
T_{m01}	9.21 s	9.41 s	1.96 s	1.93 s	1.13 s	-0.20 s	0.12	0.84
Dir_m	310.99 °	311.26 °	22.34 °	26.87 °	12.21 °	-0.27 °	0.04	0.89
T_p	11.04 s	11.07 s	2.63 s	2.46 s	1.59 s	-0.02 s	0.14	0.81
Dir_p	311.11 °	311.55 °	22.65 °	27.35 °	18.22 °	-0.44 °	0.06	0.75

Table 3.3 Statistical results for significant wave height (H_s), mean period (T_{m01}), mean direction (Dir_m), peak period (T_p) and peak direction (Dir_p). Both the buoy measured mean value ($\bar{X}$) and the SWAN simulated mean value ($\bar{Y}$) with their standard deviation (s_X and s_Y) are reported, along with the root mean square error (RMSE), the Bias, the scatter index (SI) and the correlation coefficient (r). The data refers to the period between 2010 and 2018.

A linear regression equation has also been estimated by OLS (Ordinary Least Squares) model with the GNU econometrics software GRETL (http://gretl.sourceforge.net/). The data from the buoy were considered as independent variable (X) while the data generated by SWAN simulations were considered as dependent variable (Y). The linear trend obtained from the regression test along with the correlation coefficient (r) are reported in Table 3.4 and Figure 3.5, Figure 3.6, Figure 3.7.

The SWAN model seems to underestimate the significant wave height H_s for values lower than 1 m and higher than 5 m. Nevertheless, the slope parameter for H_s and also for T_{m01}, Dir_m,T_p and Dir_p resulted to be statistically significant even at 1% (p-value < 0.01).

The r is also quite high meaning that there is a strong positive relationship between the values measured by the "Nazaré Costeira" buoy and those simulated by SWAN. To conclude, the results of the present study show that the SWAN wave model (therefore the SNL-SWAN version) can be employed with a high level of confidence for hindcasting of the wave parameters.

Parameters	Regression equation	r
H_s (m)	Y = 0.97 X	0.97
T_{m01} (s)	Y = 1.01 X	0.99
Dir_m (°)	Y = 1.00 X	1.00
T_p (s)	Y = 0.99 X	0.98
Dir_p (°)	Y = 1.00 X	1.00

Table 3.4 Results of the validation between the values obtained with the SWAN model (Y) and the values from the "Nazaré Costeira" buoy (X). The regression equation for significant wave height (H_s), mean peak period (T_m and T_p), mean and peak direction (Dir_m and Dir_p) are reported along with their correlation coefficient (r).

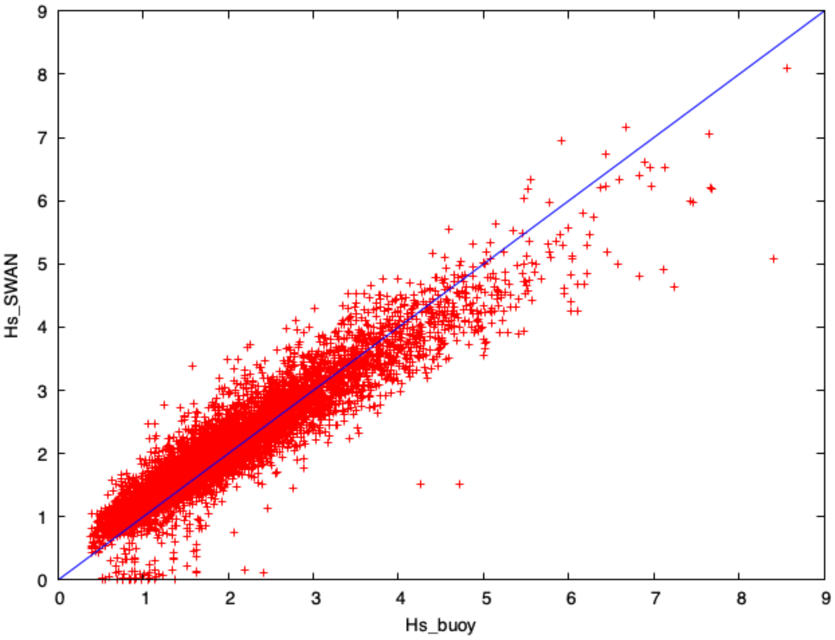

Figure 3.5 Scatterplot of the significant wave heights (in meters) computed by SWAN (on the y-axis) and obtained from the "Nazaré Costeira" buoy (on the x-axis).

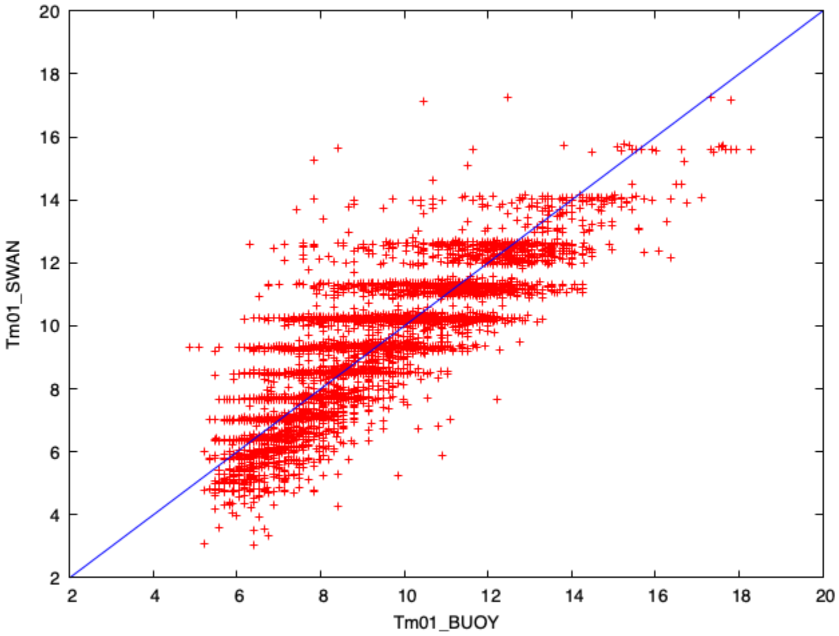

Figure 3.6 Scatterplot of the mean periods (in seconds) computed by SWAN (on the y-axis) and obtained from the "Nazaré Costeira" buoy (on the x-axis).

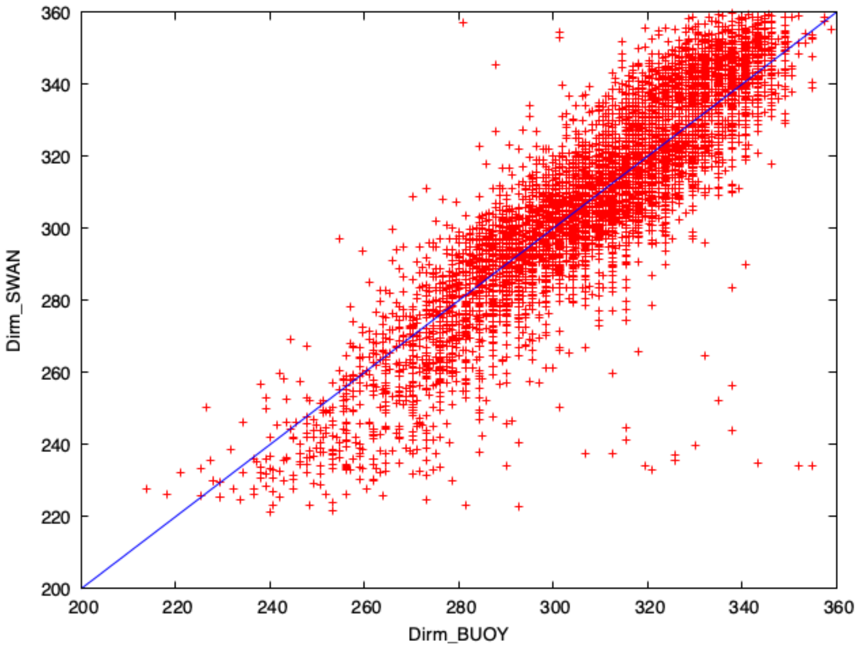

Figure 3.7 Scatterplot of the mean directions (in degrees) computed by SWAN (on the y-axis) and obtained from the "Nazaré Costeira" buoy (on the x-axis).

3.4 Offshore and nearshore wave and wave power characterization

To characterize the wave climate in Almagreira beach, two points were considered (Figure 3.3). The first point is located at the top left corner of the external main grid (with coordinates -9.74899° W, 39.68880° N) and is the same point that has been used as input boundary condition in the model. It is located at a depth of around 1700 m and the wave height, wave peak period and mean wave direction in that point were taken from the European Centre for Medium-Range Weather Forecasts (ECMWF), which provides wave hindcasted data.

The dataset considered covers the period from 2000 to 2018 with a 6 hours step. The second point is located nearshore Almagreira beach (with coordinates -9.29784° W, 39.39350° N, water depth around 10 m), at the approximate location of the WaveRoller device according to Silva *et al.*, (2016). These two locations are shown in Figure 3.3.

With the 19 years wave climate data from ECMWF and the bathymetric and computational grids previously mentioned (Table 3.1 and Table 3.2) parallel runs of SWAN have been performed, without the presence of WECs. From those simulations, the wave climate at the second point has been extracted and statistically analyzed.

An offshore and nearshore characterization of the wave power was also performed, based upon the offshore and nearshore wave regime.

3.4.1 Wave regime

3.4.1.1 *Offshore wave regime*

The data from the offshore point (-9.74899° W, 39.68880° N) have been analyzed and the percentage probability of occurrence of each sea state is reported in Table 3.5. The wave climate of those 19 years is also represented by the wave roses in Figure 3.8. It is observed that waves are concentrated in a narrow direction sector, between 290° and 340 °, which corresponds to the North-West direction. Moreover, waves mostly range between 1 and 3 m with maximum peaks of 9 m and periods ranges from 10 to 14 s with maximum peaks of 20 s.

Hs (m)	9.0						0.01	
	8.0				0.01	0.02	0.03	
	7.0				0.07	0.07	0.13	0.06
	6.0			0.04	0.21	0.32	0.38	0.15
	5.0	0.01	0.11	0.38	1.37	1.32	0.75	0.13
	4.0	0.25	0.60	1.21	5.80	3.27	0.75	0.12
	3.0	2.49	2.07	6.53	15.95	2.85	0.58	0.06
	2.0	4.41	10.72	19.77	11.75	0.81	0.17	0.02
	1.0	0.82	2.07	1.10	0.25	0.01	0.01	
	0.0	8	10	12	14	16	18	20
Tp (s)								

Table 3.5 Percentage probability of occurrence [%] of sea states for the period from 2000 to 2018. On the y-axis are reported the significant wave heights (Hs) in meters, on the x-axis are reported the peak periods (Tp) in seconds. The point considered is located offshore Almagreira beach (-9.74899° W, 39.68880° N) at around 1700 m depth. The colours help to identify the most common sea states (red) and less common sea states (orange to green). The data are taken from ECMWF dataset.

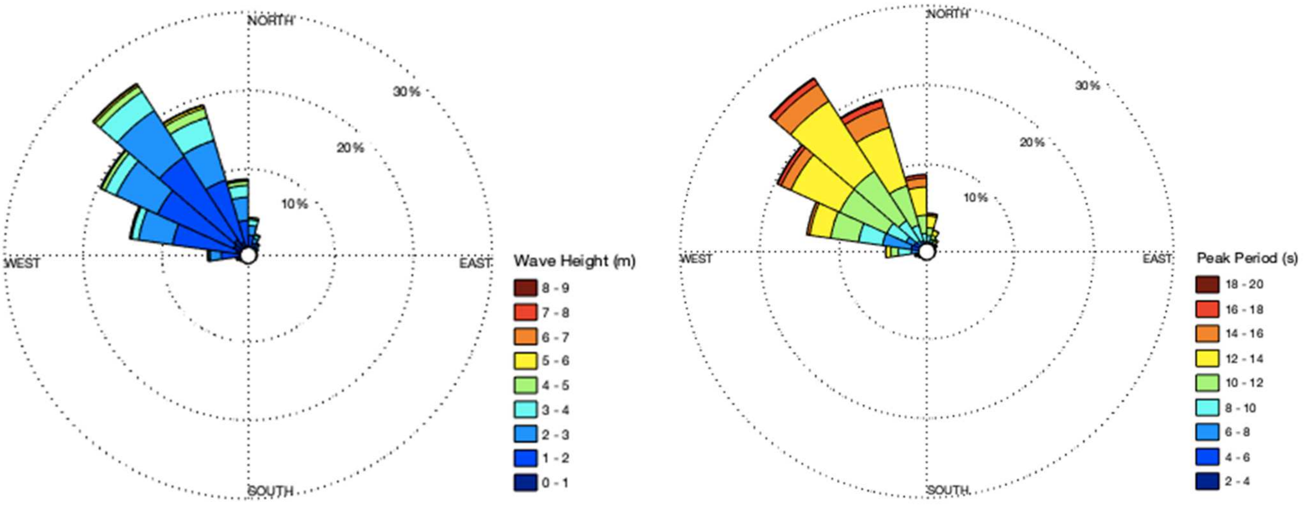

Figure 3.8 Wave roses for the period between 2000 and 2018 in the offshore point with coordinates (-9.74899° W and 39.68880° N) located at around 1700 m depth. On the left, the significant wave height is represented (in meters), on the right the peak period (in seconds). The interval of each sector is 22.5°. The data are taken from ECMWF dataset.

3.4.1.2 *Nearshore wave regime*

The ECMWF hindcasted data at the offshore point has been used as input boundary conditions to run in parallel SNL-SWAN for the 19 years, from 2000 to 2018. With that model run, the waves have been propagated from offshore to nearshore and the wave climate conditions in front of Almagreira beach have been extracted and analyzed. The bathymetric and computational grids and parameters considered for these calculations of SNL-SWAN without obstacles are the same as the ones used in subsection 3.3.1. In particular, the percentage probability of occurrence of each sea state was calculated and is presented in Table 3.6, along with the wave rose and the peak period rose (Figure 3.9) for a selected point with coordinates -9.29784° W, 39.39350° N and at a depth of around 10 m. This is where the WaveRoller device prototypes have been deployed. Compared to the results obtained offshore Almagreira beach they are quite similar but there is an overall decrease in wave height and in 90% of the cases the wave direction is between 290° and 340°.

	6.0				0.07	0.06	0.14	0.06
	5.0		0.03	0.05	0.40	0.55	0.47	0.16
	4.0	0.02	0.19	0.25	2.38	1.99	0.95	0.15
	3.0	0.85	1.28	2.20	12.39	3.95	0.78	0.09
	2.0	8.14	14.39	11.27	18.56	2.06	0.43	0.04
	1.0	4.57	6.63	2.56	1.78	0.08	0.03	
	0.0	8	10	12	14	16	18	20
	Tp (s)							

Table 3.6 Percentage probability of occurrence [%] of sea states for the period from 2000 to 2018. On the y-axis are reported the significant wave heights (Hs) in meters, on the x-axis are reported the peak periods (Tp) in seconds. The point considered is located nearshore Almagreira beach (-9.29784° W, 39.39350° N) at around 10 m depth. The colours help to identify the most common sea states (red) and less common sea states (orange to green). The data are produced by SNL-SWAN simulations.

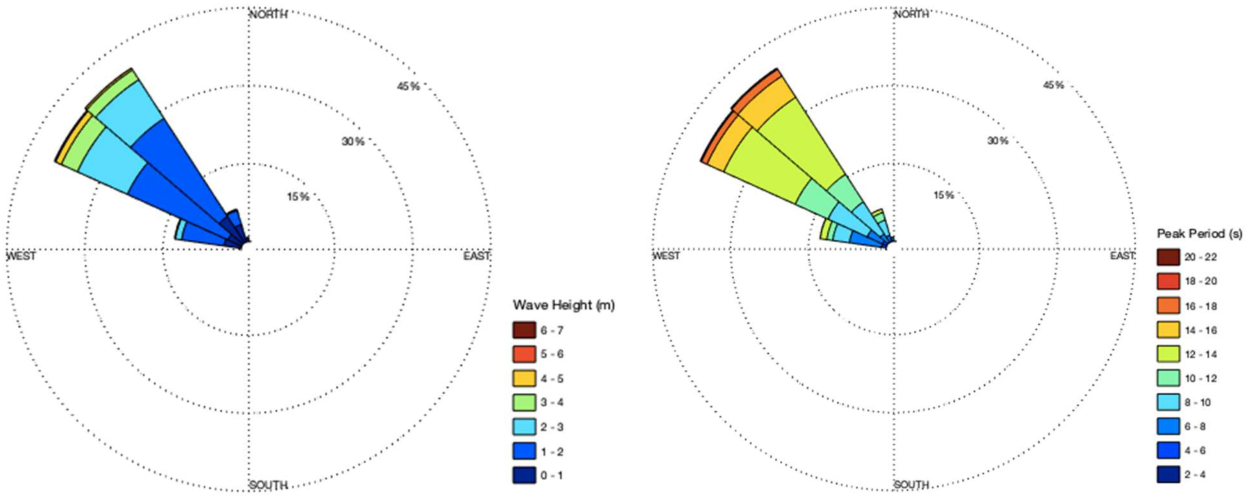

Figure 3.9 Wave roses for the period between 2000 and 2018 in the nearshore point with coordinates (-9.29784° W, 39.39350° N) located at around 10 m depth. On the left, the significant wave height is represented (in meters), on the right the peak period (in seconds). The interval of each sector is 22.5°. The data are produced by SNL-SWAN simulations.

To better characterize the offshore climate of the study area a wind rose was plotted with the data from the Nazaré Costeira buoy (located at 39°33.6' N and 9°12.6'W at a depth of 90 m) from 2011 to 2019 (Figure 3.10). The data are provided by the Portuguese Hydrographic Institute (IH) and are downloaded from the EMODNet website (http://www.emodnet-physics.eu/Map/). The main wind direction resulted to be from North, and the wind speed commonly ranges from 4 to 10 m/s, with a maximum of 20 m/s. However, to simplify the SWAN model set-up, the wind was not considered as an input.

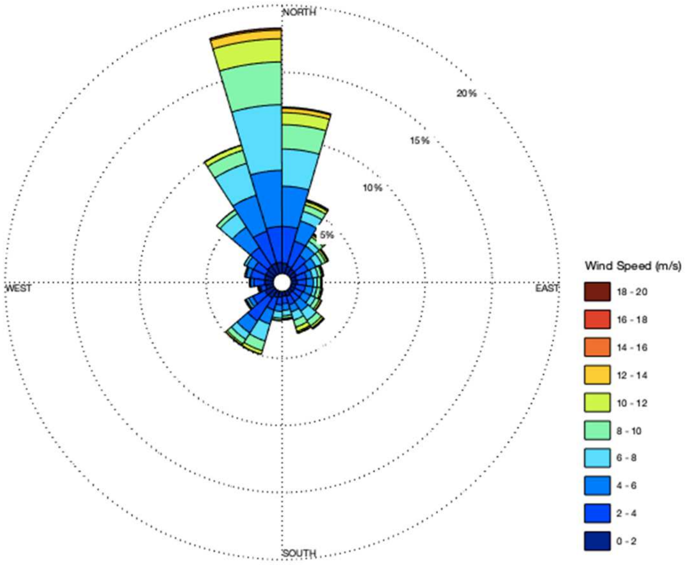

Figure 3.10 Wind speed (in m/s) rose for the period between 2011 and 2019 at the location of the Nazaré Costeira buoy. Data provider: Instituto Hidrográfico.

3.4.2 Wave power characterization

The energy flux (P) per wave front length (kW/m) of a random sea can be expressed as a function of the significant wave height (H_s) and the energy period (T_e), as below (Lisboa *et al.*, 2017):

$$P = \frac{\rho g^2}{64\pi} T_e H_s^2 \left(1 + \frac{2kh}{sinh2kh}\right) tanhkh \tag{22}$$

where ρ is the water density (1025 kg/m^3), g is the gravity acceleration (9.81 m/s^2), k is the wave number based on the period T_e ($k = 2\pi/T_e$) and h is the water depth.

In deep water conditions ($^h/_\lambda$ > 0.5, where λ is the wavelength) the following approximate relationship can be applied (Besio *et al.*, 2016):

$$P = \frac{\rho g^2}{64\pi} T_e H_s^2 \tag{23}$$

The significant wave height H_s and the energy period T_e using a spectral approach are defined as:

$$H_s = H_{m0} = 4\sqrt{m_0} \tag{24}$$

$$T_e = \frac{m_{-1}}{m_0} \tag{25}$$

where m_n is the nth-order spectral moment. The energy period physically represents the period of the sinusoidal wave that has the same energy as an actual sea-state. For the case of the JONSWAP spectrum, T_e is about 90% of the peak period T_p.

The energy flux variability is of fundamental importance for WEC installation viability since it influences the efficiency of the device. The WEC dimension and Power Take-Off (PTO) system are designed to reach high efficiency only in a certain range of wave periods and directions. However, the wave energy flux, also called wave power, must not be confused with the actual power generated by a wave power device.

3.4.2.1 Offshore wave power regime

With the simplified equation (23), it was calculated the energy flux at the offshore point (Figure 3.11). From a statistical analysis of the energy flux P in that point for the period between 2000 and 2018 it was estimated that in 80% of the cases P ranges between 0 and 50 kW/m, 15% of the cases between 50 and 100 kW/m and around 5% of the cases between 100 and 200 kW/m, with few higher picks. Thus, can be concluded that the average wave energy flux offshore Peniche is 33.62 kW/m for the period analyzed (2000-2018).

The months with a higher energy flux are those with higher waves and longer periods since P is directly proportional to H_s and T_e (Figure 3.12). In particular, January is the most energetic month decreasing until July, which is the least energetic one, followed by an increase until December. The variability of the seasonal and annual results is clear (Figure 3.13) and as expected the winter has the highest values and the summer the lowest ones. Among the years, a notable difference was shown, being 2014 the most energetic year with an average of 44.2 kW/m and 2005 the least energetic with 28.3 kW/m.

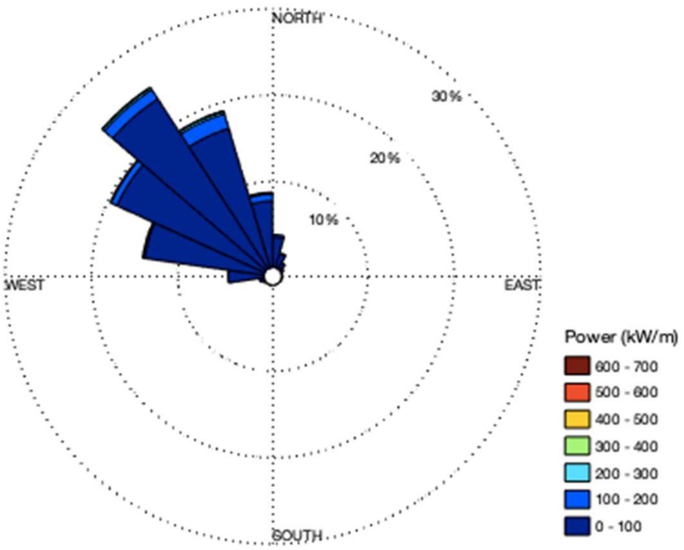

Figure 3.11 Energy flux per wave front length [kW/m] rose for the period between 2000 and 2018 in the offshore point with coordinates (-9.74899° W and 39.68880° N). The interval of each sector is 22.5°.

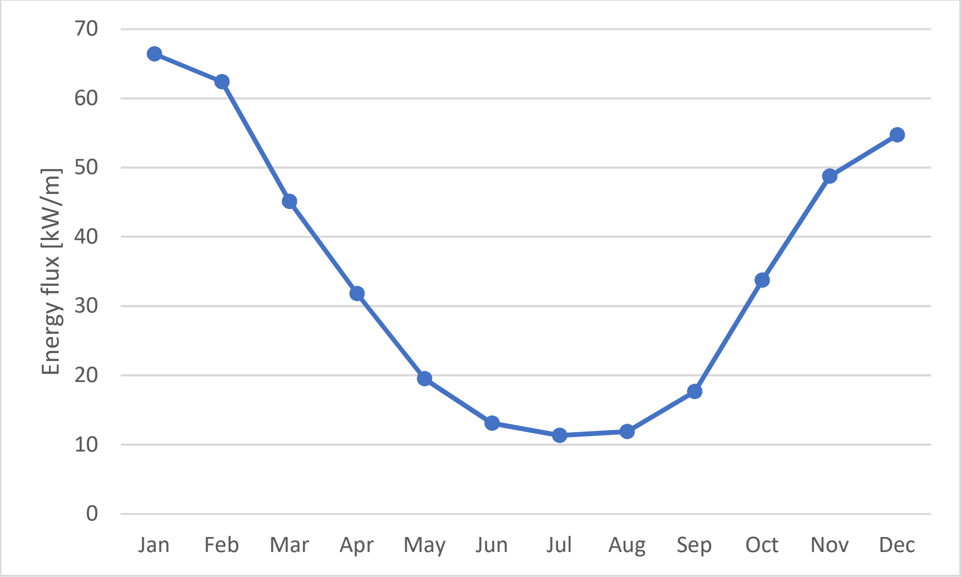

Figure 3.12 Average monthly energy flux per wave front length [kW/m] for the period 2000-2018 offshore Almagreira beach.

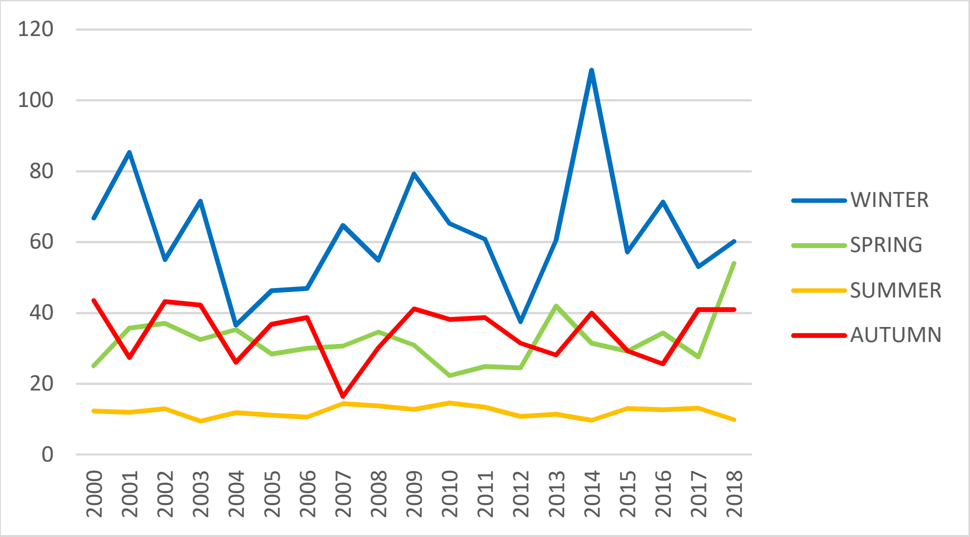

Figure 3.13 Average seasonal energy flux per wave front length [kW/m] for the period 2000-2018 offshore Almagreira beach.

By multiplying the average energy flux per wave front length, the average annual number of hours (8766 h) and the probability of occurrence of each sea state (previously reported in Table 3.5) it is possible to obtain the average annual energy per unit wave crest length available in each sea state in MWh/m (Table 3.7). From that, the most common and energetic sea states offshore Almagreira beach have been identified (Table 3.8).

Hs (m)	9.0				18.02	20.59	46.34	
	8.0				42.71	97.63	128.14	20.34
	7.0			9.34	207.12	249.16	476.53	233.59
	6.0			82.38	448.50	787.16	1060.60	457.65
	5.0	6.36	115.21	495.79	2063.40	2269.18	1451.61	278.09
	4.0	136.28	416.97	1000.73	5602.66	3612.39	933.61	167.80
	3.0	772.28	803.75	3039.37	8667.61	1768.82	406.74	45.76
	2.0	608.17	1849.03	4092.15	2837.81	223.74	53.77	7.63
	1.0	28.22	89.46	56.82	15.35	0.76	0.57	
	0.0	8	10	12	14	16	18	20
Tp (s)								

Table 3.7 Mean annual energy per unit crest length [MWh/m] available for each sea state, calculated for the period 2000-2018 offshore Almagreira beach.

Significant wave height H_s (m)	Peak period T_p (s)	Wave direction
2	12	NW
3	12	NW
2	14	NW
3	14	NW
4	14	NW
4	16	NW

Table 3.8 Most common and energetic sea states offshore Almagreira beach.

3.4.2.2 Nearshore wave power regime

With the nearshore wave climate data obtained from the SNL-SWAN simulations without WECs and the shallow water equation (22) was possible to calculate the energy flux also in the nearshore point chosen (Figure 3.14). From a statistical analysis of the energy flux P in this point for the period between 2000 and 2018 it was estimated that 90% of the times P ranges between 0 and 50 kW/m, 8% of the times between 50 and 100 kW/m and that the average wave energy flux nearshore Almagreira beach is 22.20 kW/m. The average annual energy per unit wave crest length available in each sea state in MWh/m was calculated (Table 3.9) by multiplying the average energy flux per wave front length, the average annual number of hours (8766 h) and the probability of occurrence of each sea state (Table 3.5). From that, the most common and energetic sea states nearshore Almagreira beach have been selected (Table 3.10) and will be used as wave climate input for the SNL-SWAN simulations in the presence of the WECs. In particular, case study A, B and C have the same wave height of 2 m but different wave peak period, respectively of 10 s, 12 s and 14 s. This will allow to compare the results and infer the impact of the peak period on them. Similarly, case study C, D and F have same peak period of 14 s but different wave height, respectively of 2 m, 3 m and 4 m. This will allow to detect the impact of wave height under the same peak period. Case study F has been chosen for its high peak period of 16 s and since it is still energetic and common.

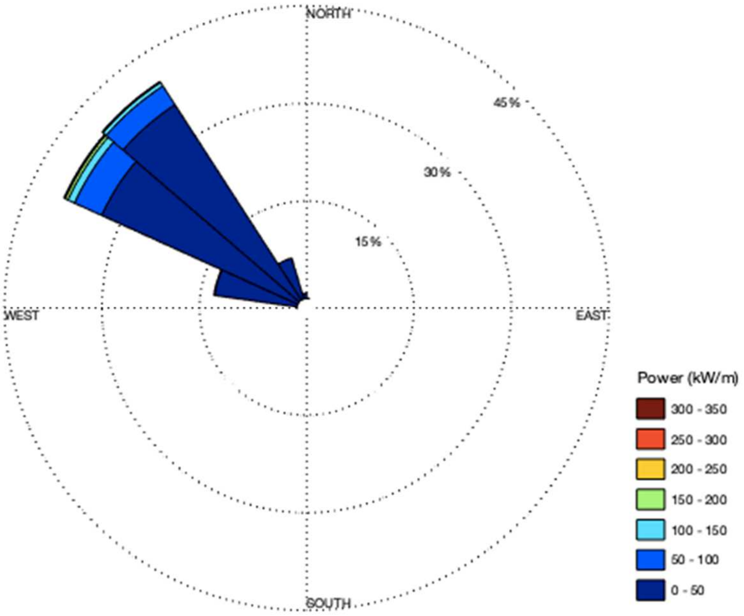

Figure 3.14 Energy flux per wave front length [kW/m] rose for the period between 2000 and 2018 in the nearshore point with coordinates (-9.29784° W, 39.39350° N). The interval of each sector is 22.5°.

Hs (m)	7.0					12.51	14.07	
	6.0				144.76	156.25	382.59	195.31
	5.0		31.91	62.23	597.59	951.04	919.13	335.10
	4.0	12.256	127.66	205.27	2301.90	2201.82	1181.08	209.36
	3.0	264.25	498.34	1023.68	6731.46	2454.07	548.03	66.06
	2.0	1122.87	2482.92	2332.29	4481.38	569.86	132.12	14.04
	1.0	157.53	285.95	132.51	107.23	5.36	2.59	0.32
	0.0	8	10	12	14	16	18	20
	Tp (s)							

Table 3.9 Mean annual energy per unit crest length (MWh/m) nearshore Almagreira beach for each sea state from 2000-2018.

Case study	Significant wave height H_s (m)	Peak period T_p (s)	Wave direction
A)	2	10	NW
B)	2	12	NW
C)	2	14	NW
D)	3	14	NW
E)	4	14	NW
F)	3	16	NW

Table 3.10 Most common and energetic sea states nearshore Almagreira beach.

4 | Application of SNL-SWAN model with devices to Almagreira beach

4.1 Introduction

This chapter is dedicated to the application of SNL-SWAN in the presence of WEC devices. Before simulating the wave propagation in Almagreira beach and the impact of a wave farm it is necessary to set up and adjust the SNL-SWAN wave model to the specific case of the present study. Therefore, a sensitivity analysis of the wave model was performed for a wave farm of 10 WaveRoller type bottom-fixed oscillating flaps (section 4.2). This section includes:

- the description of the main model set-up that has been used (subsection 4.2.1);
- the evaluation of the link between incoming waves direction and model boundary conditions (subsection 4.2.2), the computational spectral grid chosen depending on SNL-SWAN input peak period (subsection 4.2.3), the effects of considering or not triads wave-wave interactions in the physical processes of the model (subsection 4.2.4);
- the verification of the SNL-SWAN OBCASE 0 against the native SWAN and the evaluation of SNL-SWAN OBCASE 1, 2, 3 and 4 (subsection 4.2.5). In this last subsection, it is also explained why OBCASEs 3 and 4 couldn’t be considered for the simulations.

After that, different wave farms have been considered in section 4.3 in order to:

- find the optimal WECs configuration, in terms of best configuration (subsection 4.3.2) and spacing between devices (subsection 4.3.3);
- define a main input wave direction to simulate the case studies from A to F, that have been previously selected in subsection 3.4.2 as the most common and energetic sea states in the study area (subsection 4.3.4);
- understand the effects of the wave farm on the significant wave height (subsection 4.3.5), mean period (subsection 4.3.6) and mean direction (subsection 4.3.7);
- study the behaviour of a wave farm in real sea state conditions by simulating 19 years of wave climate (subsection 4.3.8);
- compare the results obtained for a WaveRoller type of WECs farm with a similar farm of Bombora’s mWave devices (subsection 4.3.9).

4.2 SNL-SWAN Sensitivity Analysis

A model sensitivity analysis was performed using SNL-SWAN by changing some input parameters to understand the model behaviour under different set-ups and to adapt the model with the specific case studies analysed. This analysis aims at establishing the dominant physical processes and appropriate model setup for the Almagreira beach under the six most common and energetic case studies. Those have been previously selected with the wave power regime analysis nearshore Almagreira beach, as reported in Table 3.10.

4.2.1 Model set-up

To perform the sensitivity analysis the model was run in a stationary mode. It covered the main grid and a nested grid, with bathymetric resolution of respectively 103.16 m and 30 m and computational resolution of respectively 50 m and 25 m. Both are regular rectangular grids and their characteristics are reported more in detail in Table 4.1 and Table 4.2. Initially, the spectrum was discretized with a frequency range between 0.04 Hz and 1.0 Hz, 35 frequency bins logarithmically spaced and with 36 equally spaced directions. Then, as explained in subsection 4.2.3, the frequency range has been changed according to the boundary peak period.

The initial wave conditions imposed to the boundary of the main grid have been previously selected with the wave power regime analysis nearshore Almagreira beach, as reported in Table 3.10. The six most common and energetic sea states: A) H_s=2m, T_p=10s; B) H_s=2m, T_p=12s; C) H_s=2m, T_p=14s; D) H_s=3m, T_p=14s; E) H_s=4m, T_p=14s; F) H_s=3m, T_p=16s.

For waves coming from the North-West (315°) those conditions are imposed to the Northern and Western boundaries of the main grid, as explained in subsection 4.2.2. In all the simulations the dissipation due to depth-induced wave breaking and due to bottom friction were activated, as well as the diffraction. The quadruplet wave-wave interactions were deactivated and the triad wave-wave interactions activated for the tests in subsection 4.2.3 and then deactivated in subsection 4.2.4.

The wave farm considered for the sensitivity analysis is composed of 10 WaveRoller type bottom-fixed oscillating flaps with 25 m length, aligned at a depth between 10 m - 15 m with 10 m spacing between them.

Bathymetric grids	Main Grid	Nested Grid
X initial (Longitude)	-137259.34	-104583.25
Y initial (Latitude)	-67313.33	-33216.34
Grid rotation (°)	0	0
n° DX	574	174
n° DY	721	156
DX (m)	103.16	30
DY (m)	103.16	30

Table 4.1 Characteristics of SNL-SWAN bathymetry grids. The initial X and Y refer to the bottom left corner (coordinate system EPSG:3763 ETRS89 / Portugal TM06) of the grid. DX and DY refer to the cell size.

Computational grids	Main Grid	Nested Grid
X initial (Longitude)	-110702	-103087
Y initial (Latitude)	-34626	-31100
Grid rotation (°)	0	0
Grid length in x direction (m)	17500	3570
Grid length in y direction (m)	16510	2400
DX (m)	50	25
DY (m)	50	25
Number of meshes in x direction	350	143
Number of meshes in y direction	330	96

Table 4.2 Characteristics of SNL-SWAN computational grids. The initial X and Y refer to the bottom left corner (coordinate system EPSG:3763 ETRS89 / Portugal TM06) of the grid. DX and DY refer to the cell size.

4.2.2 Wave direction and boundary conditions

The boundaries of the computational spatial grid in SWAN are defined as land or water. The land does not generate waves and it absorbs all incoming wave energy in SWAN. But in the case of a water boundary, there may be a problem since often no wave conditions are known along the boundary and SWAN then assumes that no waves enter the area and that waves can leave the area freely. The errors contained in these assumptions can propagate into the model. These boundaries of the main grid must, therefore, be chosen sufficiently far away from the area where reliable computations are needed (nested grid) so that they do not affect the computational results there.

In this case, the six initial boundary wave conditions, reported in Table 3.10, are imposed to the main grid. Then SNL-SWAN is run and the waves are propagated and transformed until they reach the second nested domain.

As a general suggestion, the following procedures can be followed regarding the wave direction (Dir) to avoid propagation errors:

- If the input boundary wave direction is from the North-West (315°) it must be imposed to the Northern and Western boundaries of the main grid;
- If the input boundary wave direction is from the North (360°) it must be imposed to the Northern, Western and Eastern boundaries of the main grid;
- If the input boundary wave direction is from the West (270°) it must be imposed to the Northern, Western and Southern boundaries of the main grid.

4.2.3 Computational spectral grid

In the SWAN model, as well as in the SNL-SWAN version of it, the computational spectral grid needs to be provided by the user (Ruehl *et al.*, 2014). In the frequency space, it is defined by a minimum and maximum frequency and by the frequency resolution (Δf) which is proportional to the frequency itself (f). The frequency domain is part of the command CGRID and it may be specified in four ways:

- The lowest frequency ([f_low] in Hz), the highest frequency ([f_high] in Hz) and the number of frequencies ([msc]) can be chosen.
- Only the lowest frequency and the number of frequencies can be chosen and the highest frequency will be computed by SWAN such that $\Delta f = 0.1\, f$.
- Only the highest frequency and the number of frequencies can be chosen and the lowest frequency will be computed by SWAN such that $\Delta f = 0.1\, f$.
- Only the lowest frequency and the highest frequency can be chosen and the number of frequencies will be computed by SWAN such that $\Delta f = 0.1\, f$.

This is because all the variables are related through the following equation:

$$[msc] = \log\left(\frac{[f\_high]}{[f\_low]}\right)/\log(1+\frac{\Delta f}{f}) \tag{26}$$

The last option was the one chosen for the present study. The guideline given by the SWAN User Manual is that: the value of the highest frequency must be at least 2.5 to 3 times the highest peak frequency expected. Moreover, in the SWAN user manual (Ruehl *et al.*, 2014) the recommended frequency range for applications in coastal areas is $0.04 \leq f \leq 1.00\, Hz$.

However, performing several simulations was observed that this recommended range always works well for boundary initial peak periods of 10 s or lower. While for higher peak periods it works without WECs but when obstacles are introduced in the nested domain wrong results are produced (Figure 4.1b). Thus, several tests were performed for the case study peak periods (10, 12, 14 and 16 s) changing the frequency range. In Figure 4.1 is reported, as an example, the case of 10 WECs aligned (configuration 1) for a boundary significant wave height of 2 m and peak period of 12 s. In Figure 4.1 c and d the highest frequency was changed (respectively from 3 times to 2.5 times the peak frequency) while in Figure 4.1 e and f the lowest frequency was changed (respectively from 3 times to 2.5 times the peak frequency).

Since the results didn't show significant differences, it was decided to adopt for all the cases:

$$[f\_low] = \frac{1/T_p}{2.5} \tag{27}$$

$$[f\_high] = 1/T_p * 2.5 \tag{28}$$

Therefore, in the simulations was necessary to set different frequency ranges for the six case studies (previously defined in Table 3.10) depending on the SNL-SWAN input peak period. The frequency ranges used are reported in Table 4.3.

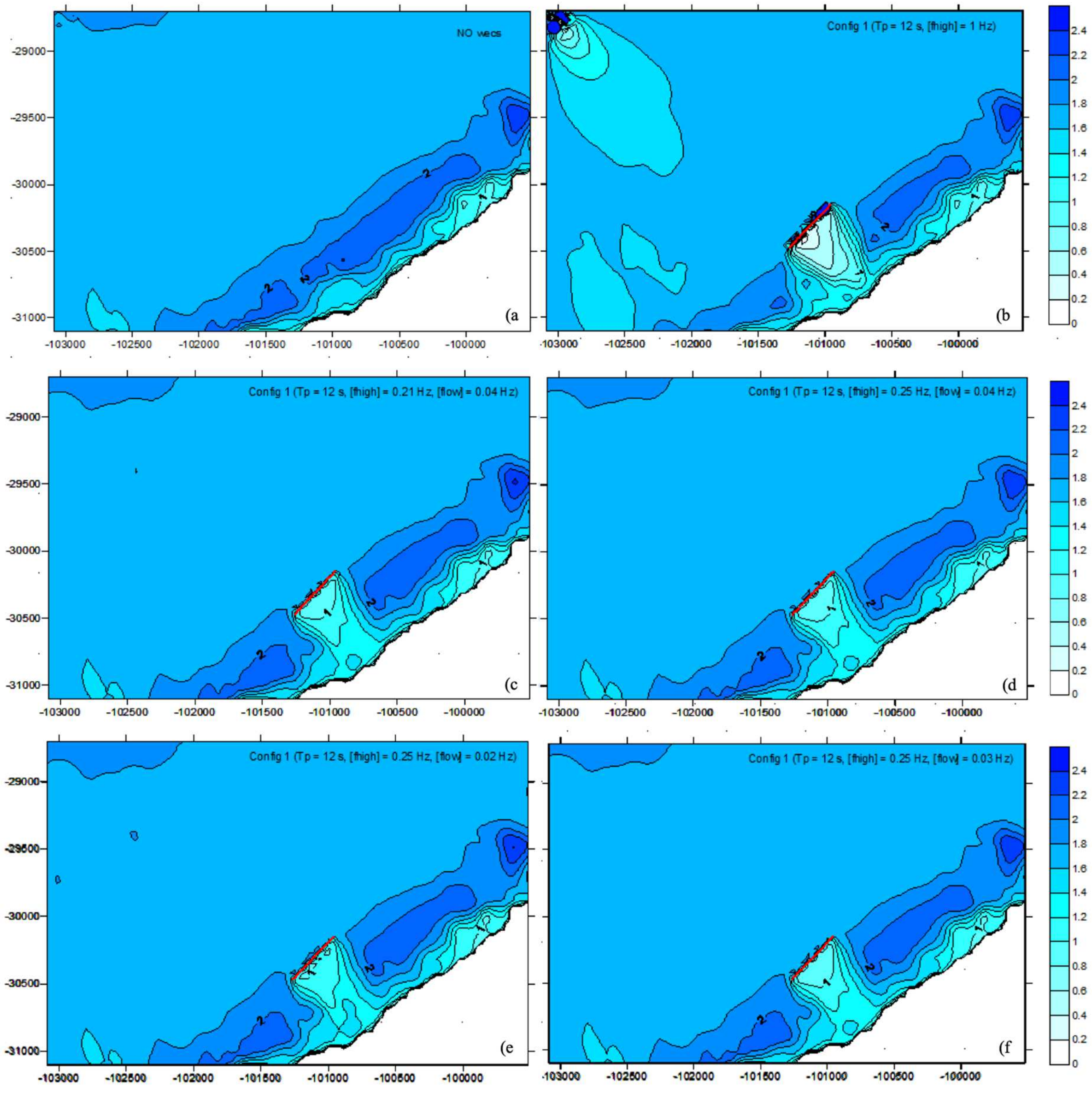

Figure 4.1 Sensitivity analysis for the frequency range. All simulations are performed with SNL-SWAN OBCASE 1.

Peak period (T_p)	Lowest frequency [f_low]	Highest frequency [f_high]
10 s	0.04	0.25
12 s	0.03	0.21
14 s	0.03	0.18
16 s	0.02	0.18

Table 4.3 Frequency range, defined by the lowest ([f_low]) and highest ([f_high]) frequencies in Hz, chosen for SNL-SWAN simulations according to boundary initial peak period (Tp) in seconds.

4.2.4 Triads

The physical meaning of the wave-wave interactions is that resonant sets of wave components can exchange and redistribute energy over the spectrum. In deep and intermediate water, four-wave interactions (so-called quadruplets) are important, while in shallow water three-wave interactions (so-called triads) become important. The triads transfer energy from lower frequencies to higher frequencies which means that running SNL-SWAN with triads gives lower periods nearshore than without triads. The test was performed for the six selected wave conditions and what can be generally concluded is:

- With triads SNL-SWAN needs almost 4 times more iterations to converge than without triads, therefore the computational speed must decrease to have a more accurate solution nearshore;
- The peak period (T_p), the mean absolute period (T_{m01}) and the mean period (T_{m02}) decreases nearshore if triad wave-wave interactions are considered. This is happening with and without WECs;
- The significant wave height (H_s) also decreases if triads are considered, but it showed smaller changes than the period.

Therefore, it was decided to consider triad interactions and loose computational speed to have better accuracy since they resulted to change significantly the wave characteristics. Of course, this is valid only for the nested domain which includes shallow water areas.

4.2.5 Evaluation of SNL-SWAN OBCASEs

4.2.5.1 OBCASE 0

SNL-SWAN was operated using switch 0 with and without WECs and compared to results from the native SWAN model to ensure model integrity. The SNL-SWAN and native SWAN model initial wave conditions were: H_S = 2 m, T_P = 10 s and Dir = 315°, applied to the northern and western boundary of the main external grid.

First, the model was run without obstacles, then with 1 WEC and finally with an array of 10 WEC devices at a depth between 10 m and 15 m (Figure 4.2), with 86% transmission ($K_t = 0.86$) and zero wave energy reflection allowed (Chang *et al.*, 2016). The 10 WECs array was arranged in a linear-shape as a representative configuration. As already mentioned, the WEC devices are the WaveRoller type bottom-fixed oscillating flaps with 25 m length and with around 10 m spacing between them.

The results from the linear regression between SWAN and SNL-SWAN models are reported in Table 4.4 and Figure 4.3. As expected, the results from SNL-SWAN switch 0 and native SWAN runs are identical, meaning that SNL-SWAN modifications did not affect the functionality and integrity of SWAN.

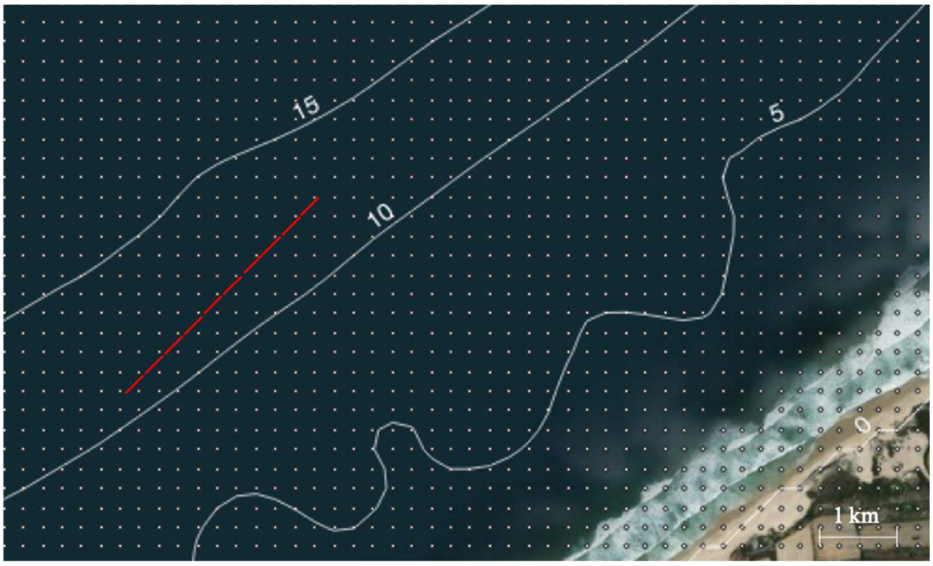

Figure 4.2 Location of 10 aligned WaveRoller type of WECs with 25 m length and 10 m spacing between them.

	Parameter	Regression equation	r
Without WECs	H_s (m)	Y = 0.99 X	0.99
	T_p (s)	Y = 1.00 X	0.99
	Dir (°)	Y = 1.00 X	0.99
With 1 WEC	H_s (m)	Y = 0.99 X	0.99
	T_p (s)	Y = 1.00 X	0.99
	Dir (°)	Y = 1.00 X	0.99
With 10 WECs	H_s (m)	Y = 0.99 X	0.99
	T_p (s)	Y = 1.00 X	0.99
	Dir (°)	Y = 1.00 X	0.99

Table 4.4 Results from the linear regression between SWAN (Y) and SNL-SWAN (X) models. Three cases have been simulated: without WECs (first row), with 1 WEC (second row) and with 10 aligned WECs (third row). The regression line equations are reported along with the correlation coefficient (r).

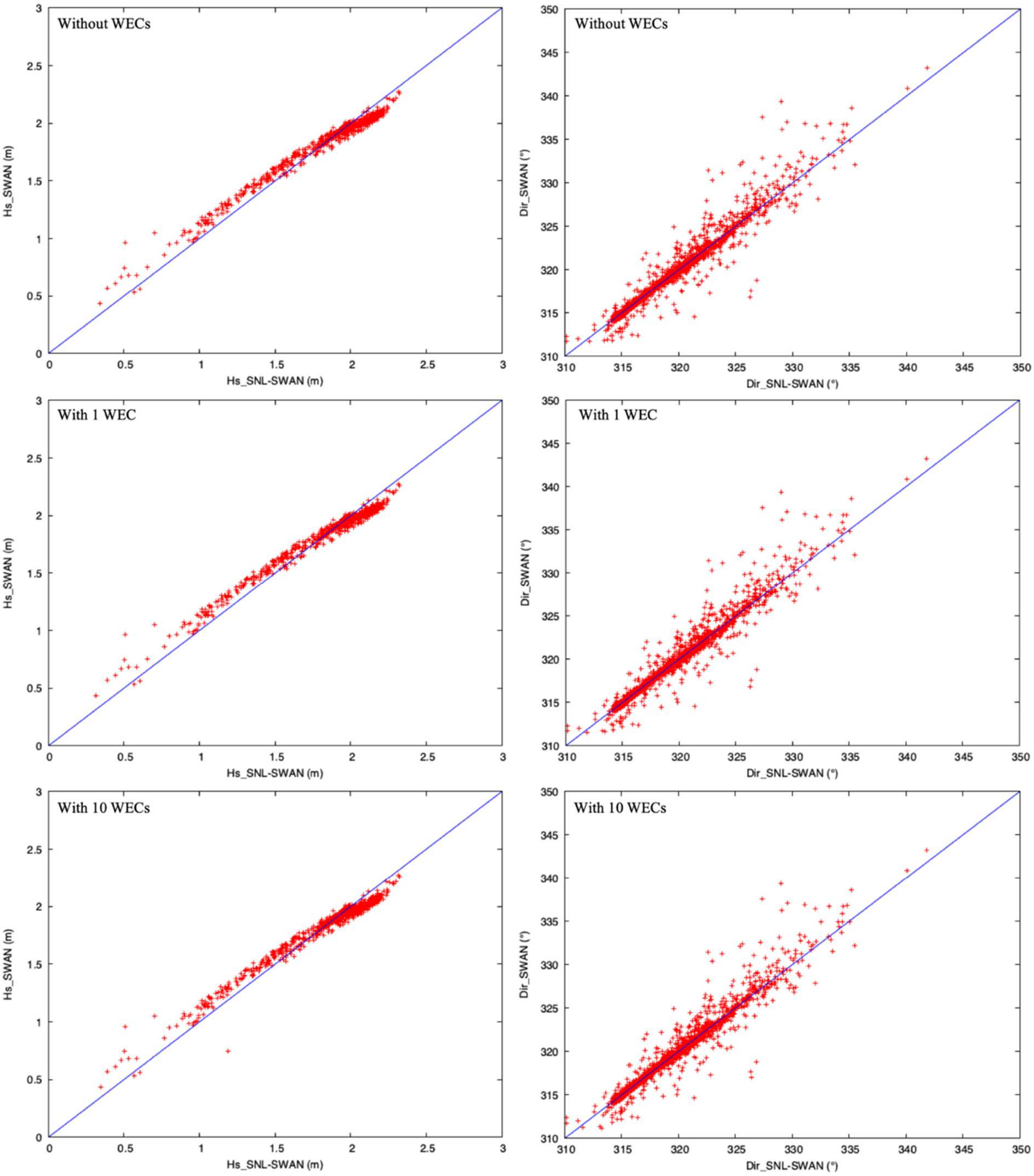

Figure 4.3 Results from the linear regression between SWAN and SNL-SWAN models. Three cases have been simulated: without WECs (first row), with 1 WEC (second row) and with 10 aligned WECs (third row). The scatterplots of significant wave heights (H_s) are reported on the left, the scatterplots of mean direction (Dir) on the right.

4.2.5.2 OBCASE 1 and OBCASE 2

The original idea was to evaluate SNL-SWAN switches 1, 2, 3 and 4 for an array of 10 WECs (with 25 m length and 10 m spacing between them) and the sea states from A to F (see Table 3.10). The characteristics of each OBCASE are reported again in Table 4.5.

OBCASE	DESCRIPTION
0	Baseline SWAN formulations using constant K_t^2 value, specified by user in INPUT file.
1	WEC power matrix used to calculate K_t^2, applied as a constant value across all frequencies.
2	WEC RCW used to calculate K_t^2, applied as a constant value across all frequencies.
3	WEC power matrix used to calculate K_t^2, applied as a unique value at each binned frequency.
4	WEC RCW used to calculate K_t^2, applied as a unique value at each binned frequency.

Table 4.5 Summary of SNL-SWAN WEC module options. Source: Ruehl et al., 2015.

The model processed the array reading the input files for the four OBCASEs without any apparent problem. However, in the visualization of the results, it was possible to verify that the influence of the converters in the wave propagation for OBCASE 3 and 4 was null, meaning that the power extracted resulted equal to zero for each of the 10 devices. This was due to a bug in the formulation of OBCASEs 3 and 4 at the time when this work was performed. Even though the bug has now been resolved in the latest version of the model (available at https://github.com/SNL-WaterPower/SNL-SWAN), only OBCASEs 1 and 2 are here reported and compared while OBCASEs 3 and 4 could not be implemented. Anyway, from previous studies with a bottom-fixed oscillating flap of 25 m was demonstrated that OBCASEs 1 and 2 simulated wave height reduction are consistently higher than those modelled using SNL-SWAN OBCASEs 3 and 4 (Ruehl *et al*., 2015).

The sea states A to F were computed without and with the WECs array and the difference in significant wave height between those two cases is reported in Figure 4.4, Figure 4.5 and Figure 4.6. The white shading in the figures indicates no changes in the significant wave height. Colour bars are also included in each figure to define the amount of change.

What can be clearly and generally observed is that OBCASE 2 tends to underestimate the effects of the wave farm on the wave propagation and transformation. The difference in significant wave height can reach up to 1 m for OBCASE 1 but instead is always lower than 0.5 m for OBCASE 2. For this reason, OBCASE 1 should be chosen to simulate the worst-case scenario in terms of changes in significant wave height, while OBCASE 2 should be chosen as the worst-case scenario in terms of wave power absorption since the devices absorb less energy than in OBCASE 1. However, being the aim of the present work to examine the effects of WECs on near-field and far-field wave conditions in the lee of the farm, OBCASE 1 was preferred to perform all the following analysis.

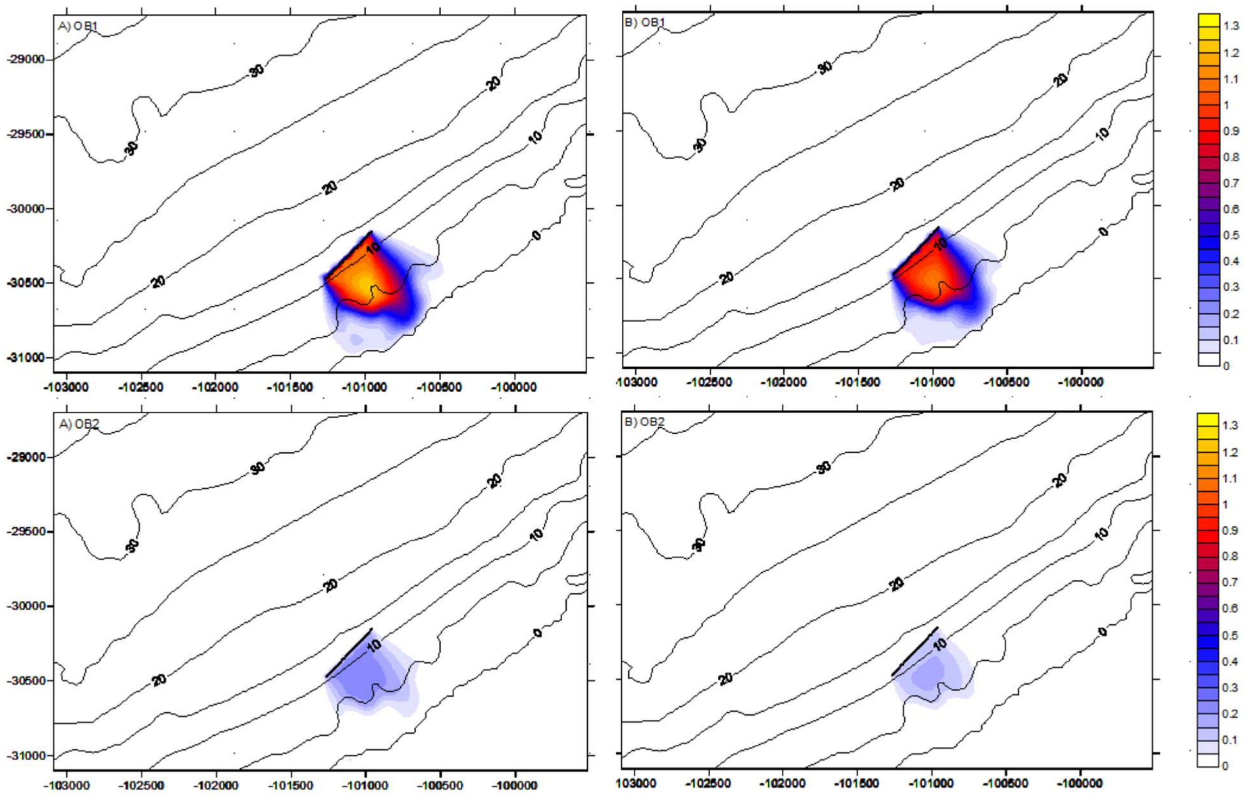

Figure 4.4 Difference in significant wave height (in meters) between case study A (left) and B (right) without obstacles and case study A and B with an array of 10 WECs (25m length, 10m spacing). SNL-SWAN OBCASE 1 (top) and OBCASE 2 (bottom) have been used. The isobaths and the WECs array are also reported.

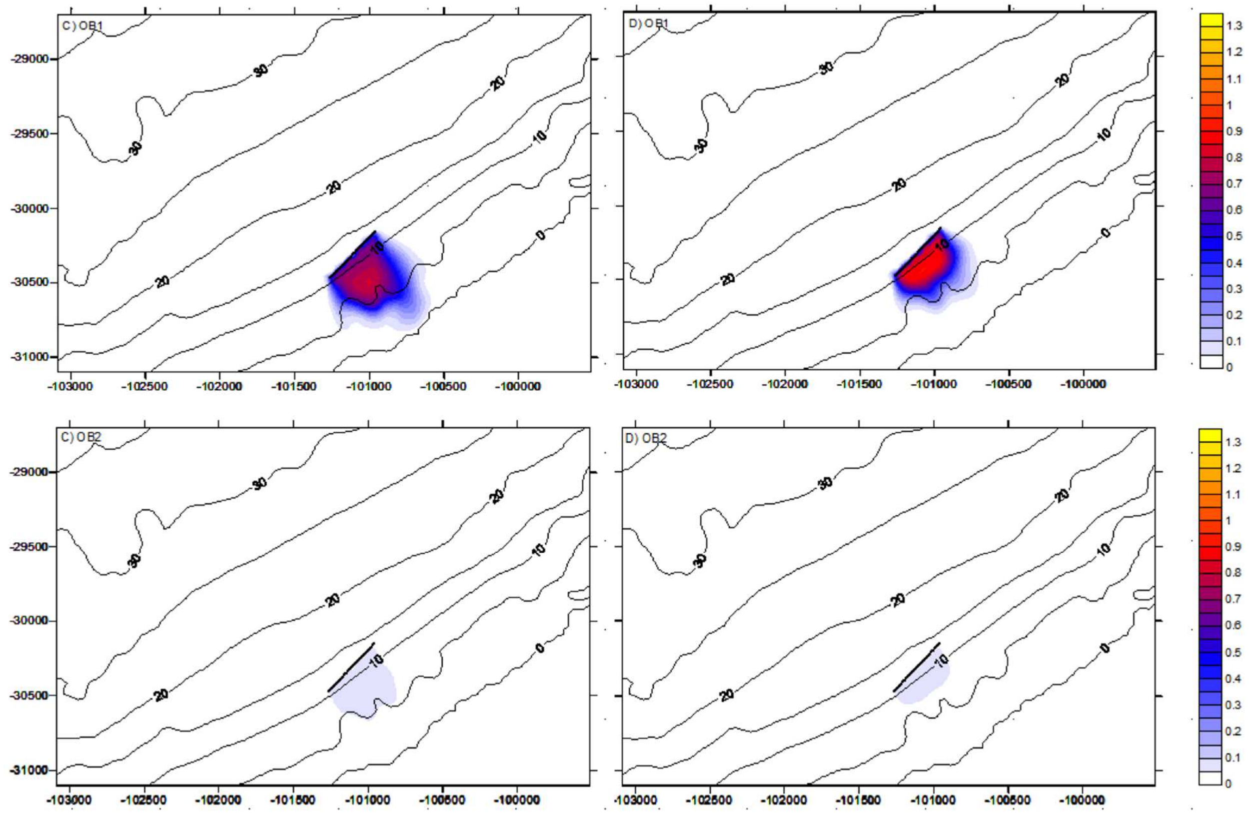

Figure 4.5 Difference in significant wave height (in meters) between case study C (left) and D (right) without obstacles and case study C and D with an array of 10 WECs (25m length, 10m spacing). SNL-SWAN OBCASE 1 (top) and OBCASE 2 (bottom) have been used. The isobaths and the WECs array are also reported.

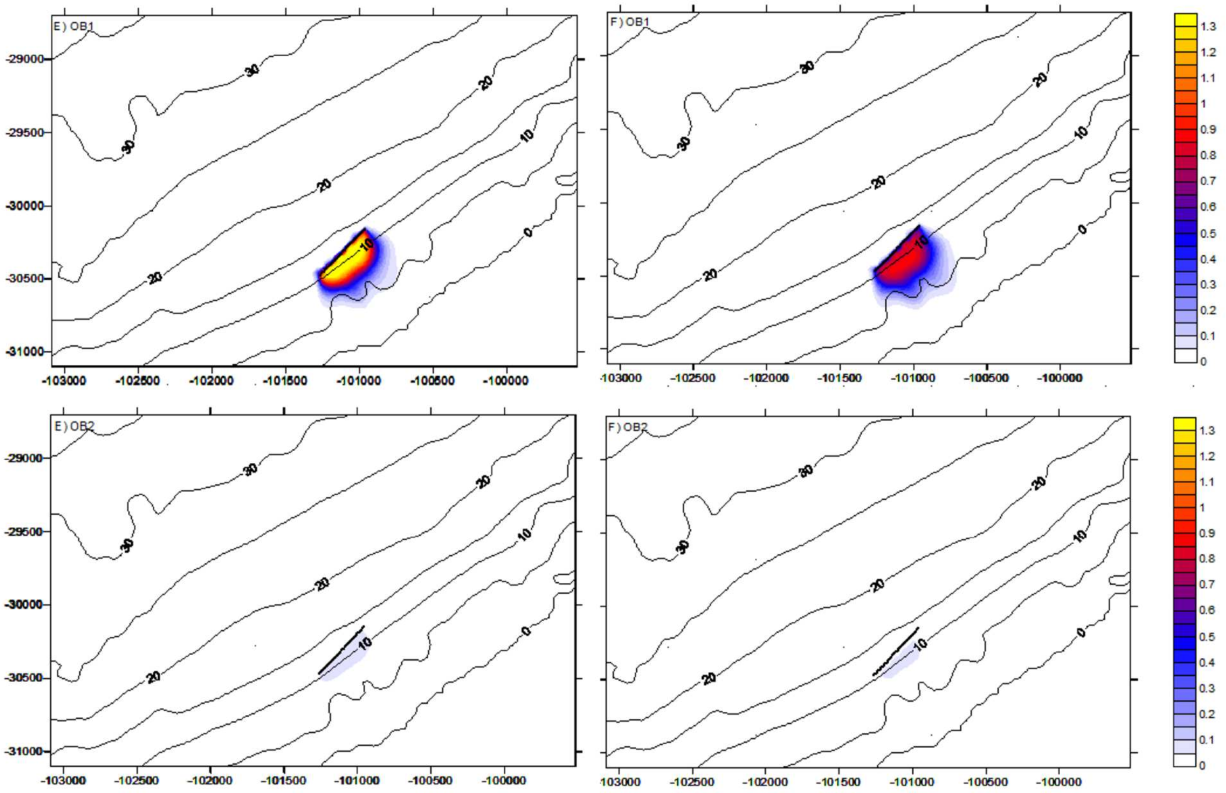

Figure 4.6 Difference in significant wave height (in meters) between case study E (left) and F (right) without obstacles and case study E and F with an array of 10 WECs (25m length, 10m spacing). SNL-SWAN OBCASE 1 (top) and OBCASE 2 (bottom) have been used. The isobaths and the WECs array are also reported.

4.3 Wave farms study

4.3.1 Introduction

The main focus of this section is to analyse the alteration of the incident wave spectra at nearshore locations downstream of the wave farm. To do so, the modelled scenario results have been compared to the baseline scenario results, where the baseline scenario does not include WEC devices. It is assumed that secondary waves potentially generated and/or radiated by a WEC are insignificant at the scales considered here. Note that the magnitude of wave height reduction is directly correlated to the WEC's power matrix values at the modelled incoming wave height and period, with larger values resulting in more reduction in wave height. Thus, the results here presented are valid for bottom-fixed oscillating flap WECs with the specific power matrix showed in Figure 2.7 and membrane pressure-differential WECs with the power matrix in Figure 2.10. The model set-up adopted for the following tests is the same as the sensitivity analysis, as described in subsection 4.2.1.

4.3.2 WECs Configuration tests

In the present study, the same configurations as Sarkar *et al.* (2014) were tested for an array of 13 WaveRoller type WECs (Figure 4.7) and the results are following presented. To evaluate the interaction effect of the WECs array configuration on the extracted power, the interaction factor (*q*-

factor) is used. It represents the ratio of the total power extracted from the array configuration to that for the same number of isolated WECs. If all the WECs are identical geometrically and operationally, that is the case the present research, the WEC array interaction q-factor [-] is:

$$q = \frac{\sum_{i=1}^{N} P_{i,tot}}{NxP_{0,tot}} \tag{29}$$

In this case $P_{i,tot}$ corresponds to the power absorbed by the ith flap and is taken from the SNL-SWAN run. While $P_{0,tot}$ corresponds to the power captured by each single device according to the power matrix, thus it depends on the significant wave height and peak period of the incident waves. If $q > 1$ there is a gain in the net power output from the array due to constructive interaction among the flaps. If $q < 1$ the mutual interactions have a cumulative destructive influence on the global array efficiency. To understand the performance of each device individually in the array another parameter can be used, the q_i^{mod}-factor (modified q-factor) defined as:

$$q_i^{mod} = \frac{P_i - P_{0,tot}}{\max(P_{0,tot})} \tag{30}$$

where P_i is the power captured by the ith flap while $\max(P_{0,tot})$ is the maximum power absorbed in the considered range of incident wave periods. This parameter represents the performance modification of each device induced by the array. If $q_i^{mod} > 0$ there is a beneficial influence, if instead $q_i^{mod} < 0$ a negative interaction effect occurs. The two parameters together, the q-factor and the q_i^{mod}-factor, can describe the performance behaviour of an array configuration both at a global-scale and single-scale.

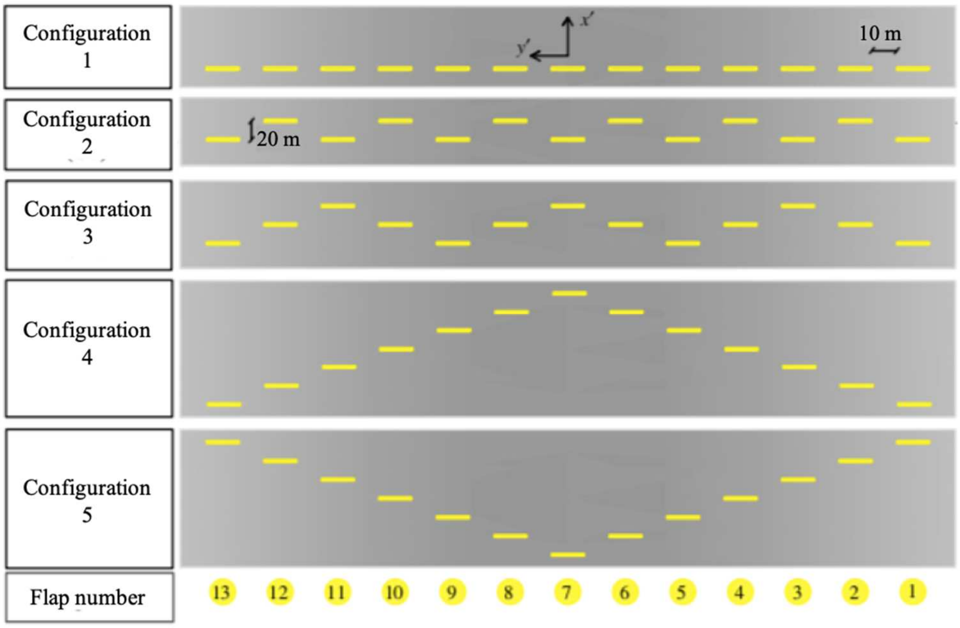

Figure 4.7 Five possible configurations of a 13 OWSC wave farm are shown here. The spacing between neighbouring flaps in all the cases is fixed at 10 m in the y-direction and 10 m in the x-direction. Readapted from: Sarkar et al. (2014).

Therefore, the wave absorption by an array of 13 WaveRoller WECs was studied for some of its possible layouts, as above mentioned. The number of devices and the configurations were chosen according to the study by Sarkar *et al.* (2014) to compare the results obtained.

It has been already proved that the dynamics of each WEC in a wave farm strongly depends on: its location in the farm, the wave frequency and the angle of incidence of waves. In particular, with an increase of the distance between the flaps, the mutual hydrodynamic interaction between them reduces and the behaviour of the converters tends towards that of an isolated device.

However, there are two considerations to make when deciding the spacing between devices:

- from an economic perspective, it is better to maximize the number of devices at a particular wave farm location to extract more power;
- from a modelling perspective, the computational grid resolution forces to locate the devices in a way that they all cross the grid lines (see 2.5.4.2 “Modelling of obstacles”). Moreover, nearshore devices such as the WaveRoller also have limited space if compared to offshore converters.

For those reasons, a spacing between devices of 10 m was chosen and a spacing between lines of 20 m. As far as their disposition is concerned, they are symmetric with respect to the central flap (number 7 in Figure 4.7) so that for normal wave incidence the hydrodynamic behaviour with respect to the x′-axis passing through the centre of the central flap is symmetric.

The five different configurations were tested and their performance has been estimated by calculating the q-factor and q_i^{mod}-factor to investigate the impact a device’s shadow has on a subsequent device’s power production. To give an example of the results obtained, here reported is the case with input wave conditions H_s = 2 m, T_p = 10 s (case study A) and Dir = 315° (normal to the array) and OBCASE 1 (Table 4.6). According to the power matrix showed in Figure 2.7, the power absorbed by an isolated bottom-fixed oscillating flap device under those incoming wave conditions is 383 kW. A value of $q > 1$, which is the case of configuration 1, implies that there is a gain in the net power output from an array because of constructive interaction among the flaps. Wave focusing effects result into an increase of the power absorption per WEC. For all the other configurations $q < 1$, which indicates that mutual interactions have a cumulative destructive influence on the array efficiency, which means that masking effects diminish the overall power absorption of the array.

The following considerations can be done on the results obtained for each configuration, Table 4.6 and Table 4.7:

- Configuration 1: this aligned configuration has the highest q-factor, implying that is the one with the highest constructive interference between all the devices. In fact, they all resulted to have a positive q_i^{mod}-factor.
- Configuration 2: in this configuration, the devices are placed in a zigzag way in two different lines. This is the configuration with the lowest q-factor, thus the worst performance among the five case studies. Moreover, the flaps located in the same line have similar hydrodynamic behaviour: the flaps in the front line (1, 3, 5, 7, 9, 11 and 13) all have negative q_i^{mod}-factor while the flaps in the back line (2, 4, 6, 8, 10 and 12) have positive q_i^{mod}-factor. What happens is that immediately behind the first line of devices there is a reduction in the wave height, meaning a less energetic wave field available for extraction by the second line.
- Configuration 3: in this configuration, the devices are also placed in a zigzag way but in three different lines. The flaps on the back line (3, 7 and 1) are the ones reached by the waves first. In fact, they have a positive q_i^{mod}-factor. While all the other devices in the second and third line have a negative q_i^{mod}-factor. The behaviour of the flaps is symmetrical with respect to the central flap 7 and the flaps having the worst performance are number 9 and 5 which are in the centre of the front line, while the external flaps (1 and 13) experience less influence from the other flaps.
- Configuration 4: in this 'V' shaped layout, the flap most exposed to the incoming waves (number 7) has the highest q_i^{mod}-factor, as observed also by Sarkar *et al*. (2014). Since all the flaps behind the central one reflects some amount of incident wave energy more energy is available for extraction by the foremost flap 7. The other flaps have a not perfect symmetrical behaviour probably because the bathymetry of the flaps placed on the right is slightly different than the bathymetry of the flaps placed on the left. This is due to the fact that the wave farm is located perpendicular to the waves coming from 315 ° and not parallel to the isobaths.
- Configuration 5: in this inverted 'V' layout, the outermost flaps (1 and 13), which are located in the front, record the highest value in the q_i^{mod}-factor. However, although the configuration mirrors the previous one, there is no such equivalent constructive focusing effect on the central flap (number 7), which showed instead the lowest q_i^{mod}-factor.

The same analysis was performed for the six case studies (defined in Table 3.10) and what can be concluded is that: the aligned configuration (number 1) resulted to have the highest q-factor in all the considered wave conditions, thus the best performance; the 'V' shaped layout (number 4) resulted to have the lowest q-factor, thus generally the worst performance. All the results are summarized in Table 4.8.

Configuration	q-factor
1	1.05
2	0.75
3	0.76
4	0.78
5	0.79

Table 4.6 Values of the q-factor for five different WECs array configurations.

q_i^{mod}-factor					
Obstacle	Config. 1	Config. 2	Config. 3	Config. 4	Config. 5
1	0.21	-0.09	-0.07	-0.08	0.22
2	0.18	0.01	-0.05	0.00	-0.08
3	0.18	-0.43	0.22	-0.08	-0.19
4	0.20	0.05	-0.03	0.01	-0.01
5	0.22	-0.43	-0.43	-0.06	-0.17
6	0.23	0.06	-0.01	-0.04	0.02
7	0.23	-0.43	0.23	0.23	-0.44
8	0.21	0.04	-0.04	-0.06	0.04
9	0.20	-0.43	-0.43	-0.18	-0.07
10	0.18	0.04	-0.01	-0.03	0.01
11	0.17	-0.43	0.23	-0.18	-0.07
12	0.18	0.04	-0.04	0.00	-0.04
13	0.20	-0.16	-0.16	-0.16	0.26

Table 4.7 Values of the modified q-factor for each single device (numbered from 1 to 13) in all the five different WECs array configurations.

Case study	Significant wave height H_s (m)	Peak period T_p (s)	q-factor				
			Config 1	Config 2	Config 3	Config 4	Config 5
A)	2	10	1.05	0.75	0.76	0.78	0.79
B)	2	12	1.29	0.95	0.98	0.94	0.99
C)	2	14	1.21	0.94	0.93	0.91	0.95
D)	3	14	1.33	1.08	1.06	1.03	1.08
E)	4	14	1.33	1.01	1.01	0.98	1.01
F)	3	16	1.44	1.16	1.13	1.10	1.16

Table 4.8 Values of the q-factor for five different WECs array configurations the initial wave conditions from A to F.

4.3.3 WECs optimal spacing

Apart by choosing the best array configuration, the power generated from the WECs could be further maximized by arranging the devices in the array at their optimal spacing. If the WECs are spaced at their optimal spacing the destructive interference is minimized and the maximum amount of wave energy is generated from the array layout. The optimal spacing of an array of WECs has been studied by using various optimization techniques and types of devices, such as point absorbers (Child & Venugopal, 2010), adjacently placed oscillating wave surge converters and point absorbers (Sarkar *et al.*, 2014), generic WECs (Borgarino *et al.*, 2012). The parametric behaviour of an in-line array of OWSCs, which is the case of the present work, has been investigated concerning the spacing between the flaps (Renzi & Dias, 2012; Tay & Venugopal, 2016).

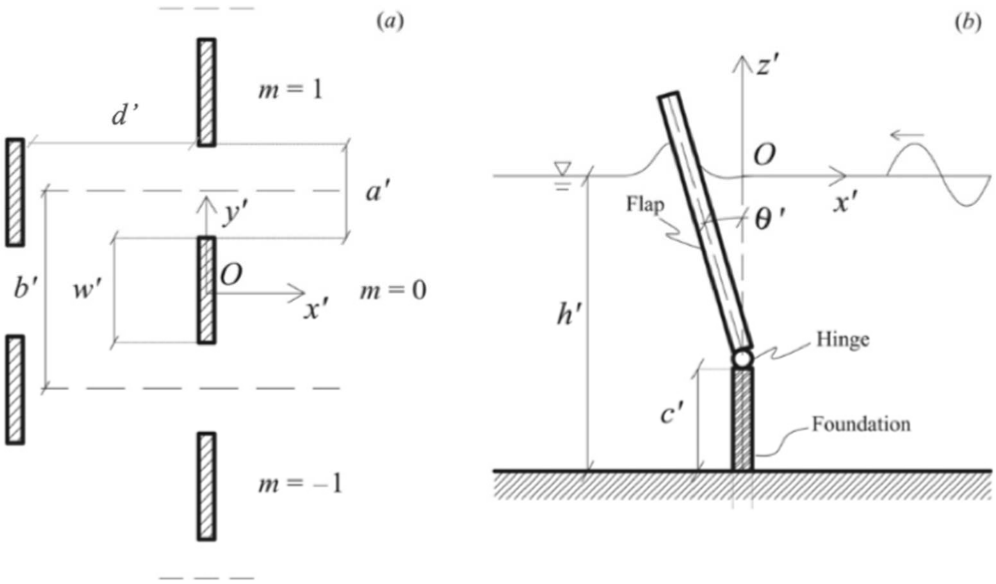

Figure 4.8 Geometry of an array (a) and reference flap (b) in physical variables. Readapted from: Renzi & Dias (2012).

The optimal flap spacing is the spacing that maximizes the q-factor, which means that the constructive interaction among the flaps is maximum (Renzi *et al.*, 2014). The geometry of a three-flaps array is reported in Figure 4.8 to define the necessary array dimensions. The array that has been tested in the present study to find the optimal spacing is composed of 13 bottom-fixed oscillating flaps (with w'= 25 m and with at a depth of h'= 25 m). The spacing between them was set equal to a' = 10 m, 20 m and 50 m. Then, for each spacing, the six wave case studies from A to F (defined in Table 3.10) have been simulated with SNL-SWAN. In all the cases the incoming waves are perpendicular to the array, thus coming along the x' direction. From the results in terms of q-factor, reported in Table 4.9, the array seems to have a better performance (higher q-factor) for a spacing of 10 m and 50 m and a less good performance (lower q-factor) for a spacing of 20 m. As already mentioned, the q-factor is a performance assessment parameter that quantifies the average total power produced by an array compared to an individual device. However, the result obtained seems only partially in accordance to what has been found in a previous research on OWSC by Tay & Venugopal (2016). They found the optimal spacing to be highly correlated to the scattering parameter (kw'), defined as the product between the wave number (k) and the device length (w'). The wave number is defined as:

$$k = \frac{2\pi}{\lambda} = \frac{2\pi f}{c} \tag{31}$$

where λ is the wavelength, f is the wave frequency and c is the wave speed. According to the linear wave theory, also known as Airy wave theory, if the water depth (around 10 m) is much less than the wavelength (that ranges between 110 m for 10 s period waves and 170 m for 16 s period waves) the shallow-water approximation is valid (Stewart, 2008), which means the wave speed can simply be estimated from the water depth (h) and the gravity coefficient (g):

$$c = \sqrt{gh} \tag{32}$$

Therefore, it was possible to estimate the scattering parameter (kw') for the case under study and compare it with the results of Tay & Venugopal (2016). Since in this case it is ranging from 1.5 to 0.9 their suggested optimal spacing for a single-array (which means the devices are deployed in a single line) is two times the length of the device ($2w'$), that would be 50 m for the present array. This is the spacing that was selected for the following simulations. Moreover, it was already observed from previous studies that wave height reductions decrease with increasing WEC spacing (Chang *et al.*, 2016). This indicates that closely spaced arrays have potentially more effects on nearshore wave propagation if compared to arrays of WECs spaced further apart. Also, the locations directly in the lee of the WEC array are the most sensitive to the spatial extent of the array, while at greater distance from the so-called WEC array footprint area the model results are less sensitive to the WECs spacing.

Case study	Significant wave height H_s (m)	Peak period T_p (s)	q-factor		
			a'=10 m	a'=20 m	a'=50 m
A)	2	10	1.05	0.94	0.95
B)	2	12	1.29	1.15	1.17
C)	2	14	1.21	1.09	1.12
D)	3	14	1.33	1.19	1.24
E)	4	14	1.33	1.20	1.24
F)	3	16	1.45	1.30	1.34

Table 4.9 Q-factor relative to the case studies from A to F for an array of 13 aligned bottom-fixed oscillating flaps of 25 m length and spacing between them (a') equal to 10 m, 20 m or 50 m.

With a fixed spacing between aligned devices of a'=50 m, the case studies A to F have been simulated for an array of 13 WECs alternated in two lines (configuration 2 in Figure 4.7). The spacings between the two lines (d' in Figure 4.8) that have been tested are again 10, 20 and 50 m. The results in terms of the q-factor are reported in Table 4.10. The configuration that resulted to have for all the simulated cases the higher q-factor is with a spacing of d'=20 m between the two lines of WECs.

Case study	Significant wave height H_s (m)	Peak period T_p (s)	q-factor		
			d'=10 m	d'=20 m	d=50 m
A)	2	10	0.71	0.77	0.64
B)	2	12	0.90	1.00	0.80
C)	2	14	0.90	1.00	0.81
D)	3	14	1.05	1.16	0.94
E)	4	14	0.99	1.08	0.87
F)	3	16	1.12	1.24	1.01

Table 4.10 Q-factor relative to the case studies from A to F for an array of 13 alternated bottom-fixed oscillating flaps of 25 m length and spacing between the two lines of WECs (d') equal to 10 m, 20 m or 50 m.

4.3.4 WEC array and wave-propagation directions

Comparisons of the q-factor for different wave-propagation directions have been performed for the array of 13 aligned WECs. The spacing between them is 50 m, since it resulted to be the spacing that guarantees the best performance. Three wave directions have been tested: waves coming from the North (360°), East (270°) and North-East (315°). The q-factor for each simulated case is reported in Table 4.11 and it was found to be the largest when the wave approaches from the head sea direction (i.e., 315°). A large difference between the q-factor for the head sea condition and that of the oblique seas was observed, implying that the WaveRoller devices are most effective in generating power when subjected to a head sea condition. This was the result expected since, for this directional device, the optimal performance is for a wave with a direction perpendicular to the device. For this reason, the wave farm was located perpendicular to the most common wave direction, which is exactly 315°.

Case study	Significant wave height H_s (m)	Peak period T_p (s)	q-factor		
			Dir=270°	Dir=315°	Dir=360°
A)	2	10	0.68	1.06	0.86
B)	2	12	0.85	1.32	1.03
C)	2	14	0.88	1.22	1.06
D)	3	14	1.10	1.34	1.20
E)	4	14	0.85	1.33	1.13
F)	3	16	1.15	1.45	1.30

Table 4.11 Q-factor relative to the case studies from A to F for an array of 13 bottom-fixed oscillating flaps of 25 m length, 50 m spacing between them and waves coming from 260°, 315° (which is perpendicular to the devices) and 360°.

4.3.5 WECs effects on significant wave height

To assess the WECs impact on significant wave height, 10 wave farms have been simulated with a number of WECs increasing from 10 to 100 and placed between a depth ranging from 10 m to 17 m. Even if from the results in subsection 4.3.2 the configuration number 1 has been proven to give the highest performance, the configuration 2 was instead chosen because it easier allowed to have a farm with such a high number of devices concentrated in a small spatial area. As previously mentioned (subsection 4.3.3), the spacing chosen between aligned devices is 50 m while between two lines of devices is 20 m. For all the simulated initial wave conditions the q-factor decreases exponentially with a significant correlation coefficient, as reported in Figure 4.9. Only when $q > 1$ there is a gain in the net power output from the array due to constructive interaction among the flaps. While when $q < 1$ the mutual interactions have a cumulative destructive influence on the global array efficiency.

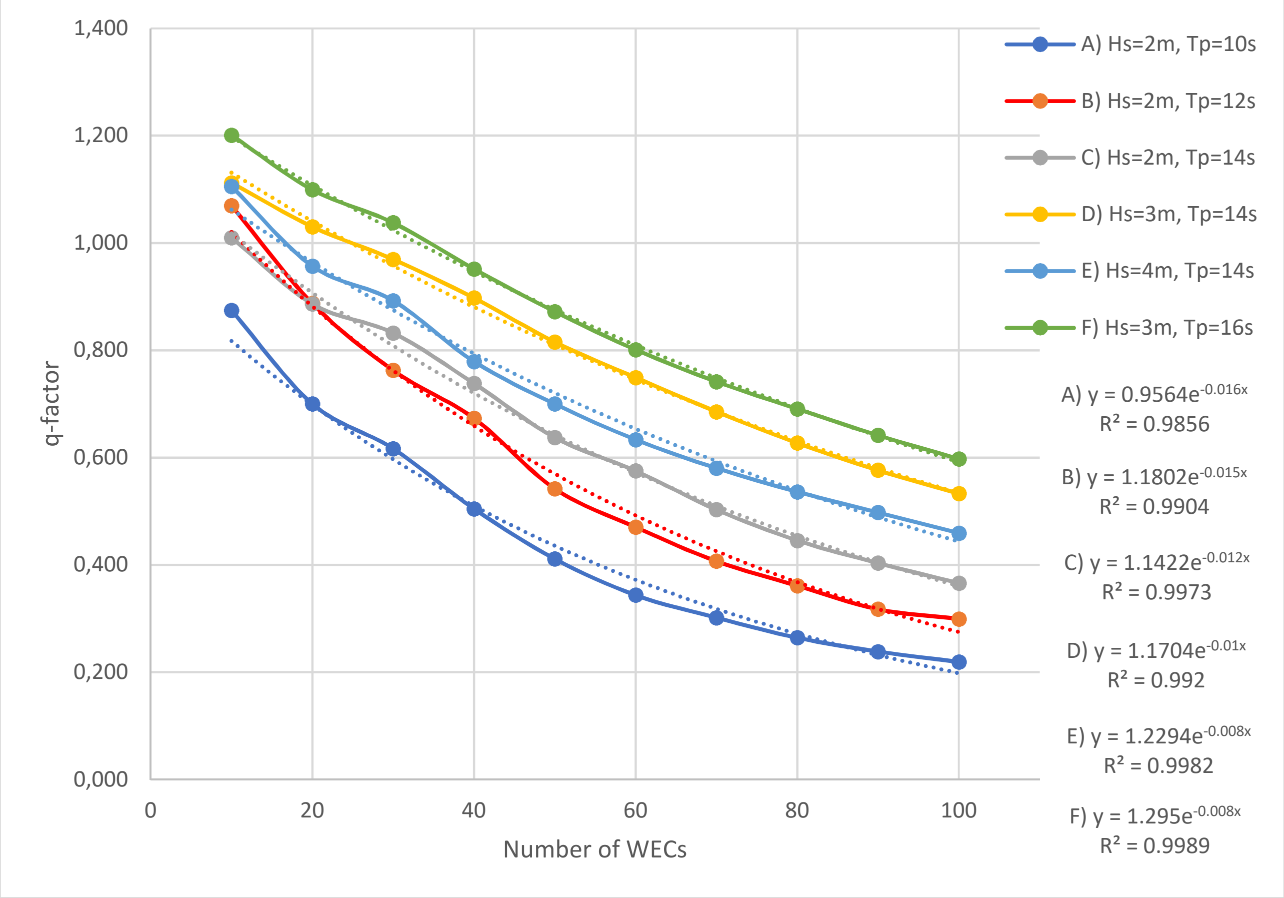

Figure 4.9 Q-factor exponential trend for different initial wave conditions (A to F) and a different number of devices (10 to 100). The exponential trend equation is reported with the correlation coefficient.

The reason why in most of the cases the q-factor resulted <1 is that this kind of configuration was already proven not to give the best performance. However, it is still interesting to investigate the percentage difference in significant wave height in the lee of the wave farm with and without the devices. To do so, it is necessary to define and calculate the significant wave height percentage change

($H_s\ diff$) between the baseline scenario (that does not include the WECs) and the scenarios with 10 to 100 WECs, as follows (Chang *et al.*, 2016):

$$H_s\ diff = \frac{H_s\ baseline - H_s\ WECs}{H_s\ baseline} x\ 100 \tag{33}$$

The percentage change has been estimated for all the initial wave conditions and number of devices and the maximum percentage change for all the cases is reported in Table 4.12. Since it is a positive change it means the devices are decreasing the significant wave height. There were also a few negative changes, not reported in the table. As expected, if the number of WECs in the array is larger, the difference between modelled wave height with and without obstacles is also greater. This result is directly correlated to WEC power absorption because more buoys will absorb more power. Moreover, it was observed that for the case studies with same initial significant wave height (e.g. case studies A, B, C and case studies D, F) the percentage decrease is always higher for lower initial peak periods. For instance, looking at the results in Table 4.12 for 100 WECs: case study A has a maximum percentage decrease of H_s of 73.31 %, that is higher case study B (65.19 %), that is higher than case study C (63.58 %) as well as the maximum percentage decrease for case study D (78.36 %) is higher than case study F (75.07 %).

For the sake of brevity, only the plots of significant wave height and percentage change for the case study with higher initial boundary condition (case study E with H_s=4 m, T_p=14 s, Dir=315°) are reported. Figure 4.10 to Figure 4.14 presents the extent of the wave farm's impact on the surrounding wave climate when 10 to 100 obstacles are employed. The black shading in the figures on the right indicates no changes in the significant wave height from the baseline scenario. Colour bars are also included in each figure to define the amount of change.

The percentage change in significant wave height can reach more than 80% difference between the case with 100 devices and the case without. In particular, for an array of 10 WECs the maximum percentage change is 62.34% (case study A at 10.73 m depth), that corresponds to 1.08 m; for 50 WECs the maximum percentage change is 79.24% (case study A at 11.19 m depth), that corresponds to 1.38 m; for 100 WECs the maximum percentage change is 83.06% (case study E at 11.17 m depth), that corresponds to 3.36 m. Therefore, an increase in the number of devices corresponds to an increase in percentage change of significant wave height in the lee of the wave farm and to an increase in the footprint area (i.e., the area affected by the change). The extent of this area was not exactly measured but it can be visually assessed from Figure 4.10 to Figure 4.14. The extend of the coastline affected by the change in wave height is, instead, always smaller or equal to the length of the wave farm, at least for the direction simulated (315°). However, even in the worst-case scenario (which is case study E with 100 WECs) the percentage change near the coastline ranges between 0 and 5%.

Case Study	H_s(m)	T_p (s)	Number of WECs									
			10	20	30	40	50	60	70	80	90	100
A)	2	10	62.34	70.07	63.65	69.44	79.24	69.62	77.52	69.05	74.82	73.31
B)	2	12	51.32	63.97	55.36	65.63	68.45	73.64	68.26	73.57	66.69	65.19
C)	2	14	36.27	45.91	57.90	65.17	63.90	65.39	69.59	66.35	66.95	63.58
D)	3	14	28.71	41.83	51.71	59.27	67.35	74.94	78.98	73.53	76.32	78.36
E)	4	14	35.47	43.06	53.22	58.78	67.39	72.26	77.42	81.85	83.15	83.06
F)	3	16	27.16	37.54	46.45	51.44	60.10	65.03	70.42	74.93	77.09	75.07

Table 4.12 Maximum percentage decrease of significant wave height (% Hs diff) for case studies A to F and a number of 10 to 100 WECs.

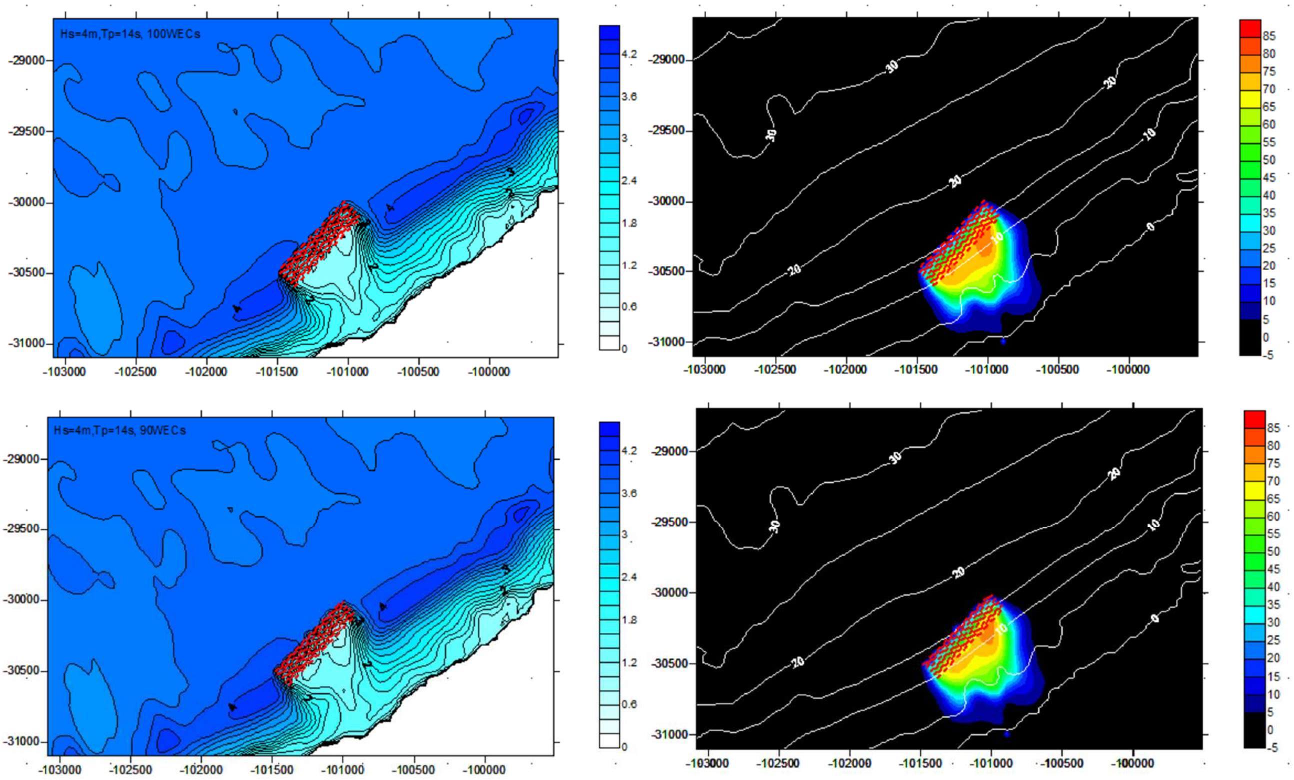

Figure 4.10 Significant wave height (left) in meters and percentage decrease (right) in % for a wave farm of 100 (top) and 90 (bottom) devices (red lines) and initial boundary wave conditions of H_s=4 m, T_p=14 s, Dir=315°. The isobaths are also reported (white lines on the right).

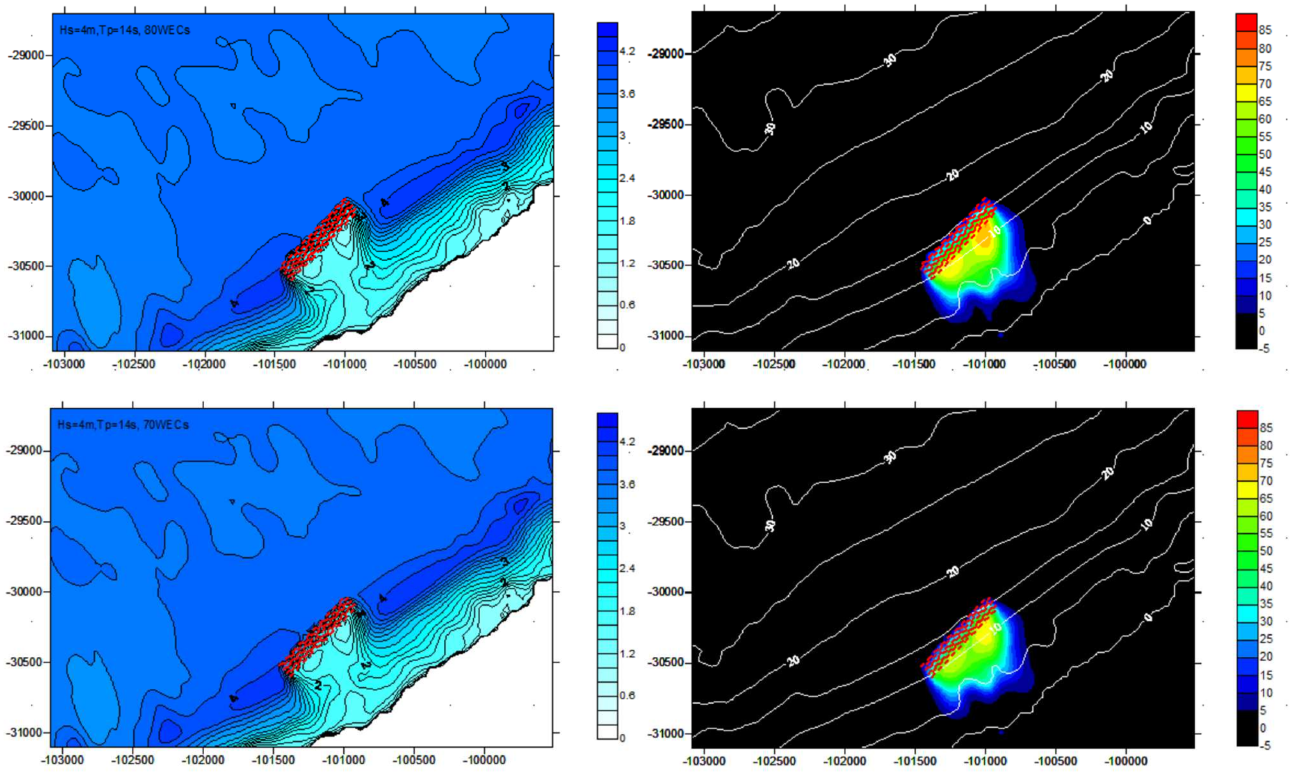

Figure 4.11 Significant wave height (left) in meters and percentage decrease (right) in % for a wave farm of 80 (top) and 70 (bottom) devices (red lines) and initial boundary wave conditions of H_s=4 m, T_p=14 s, Dir=315°. The isobaths are also reported (white lines on the right).

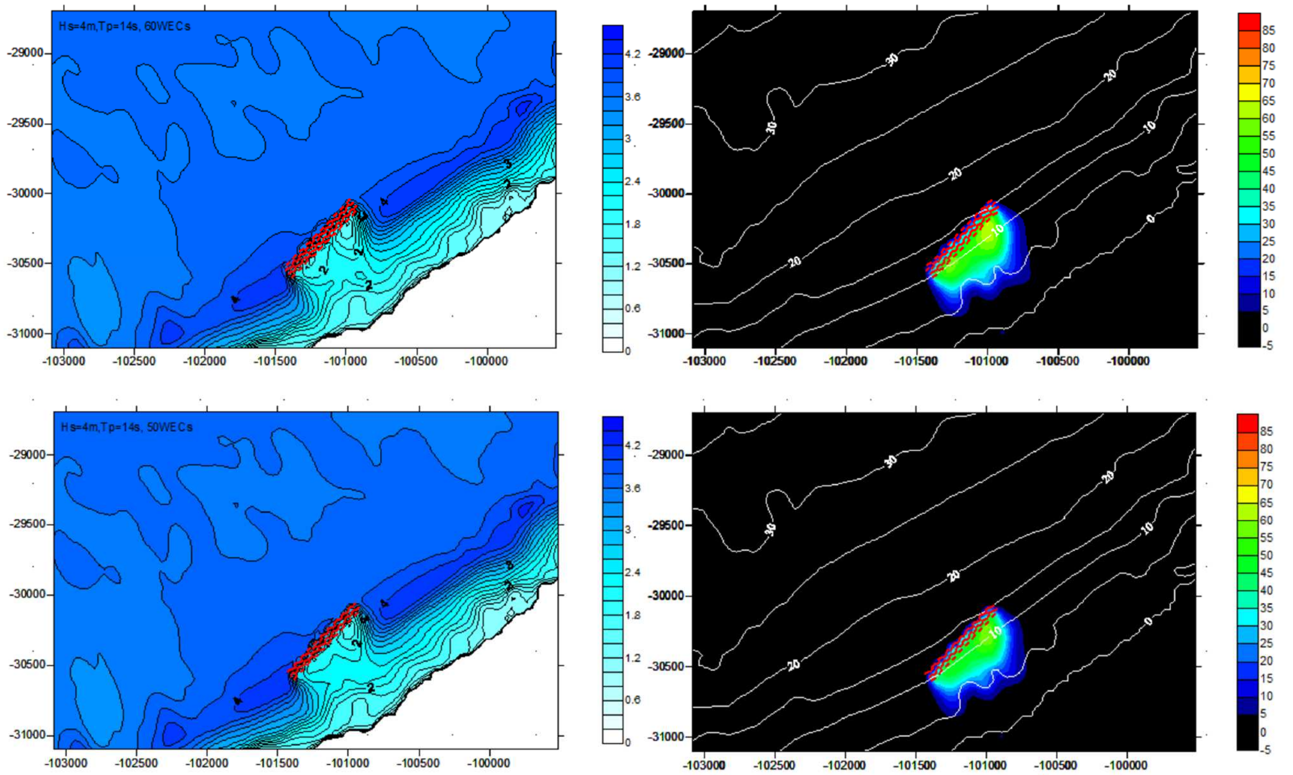

Figure 4.12 Significant wave height (left) in meters and percentage decrease (right) in % for a wave farm of 60 (top) and 50 (bottom) devices (red lines) and initial boundary wave conditions of H_s=4 m, T_p=14 s, Dir=315°. The isobaths are also reported (white lines on the right).

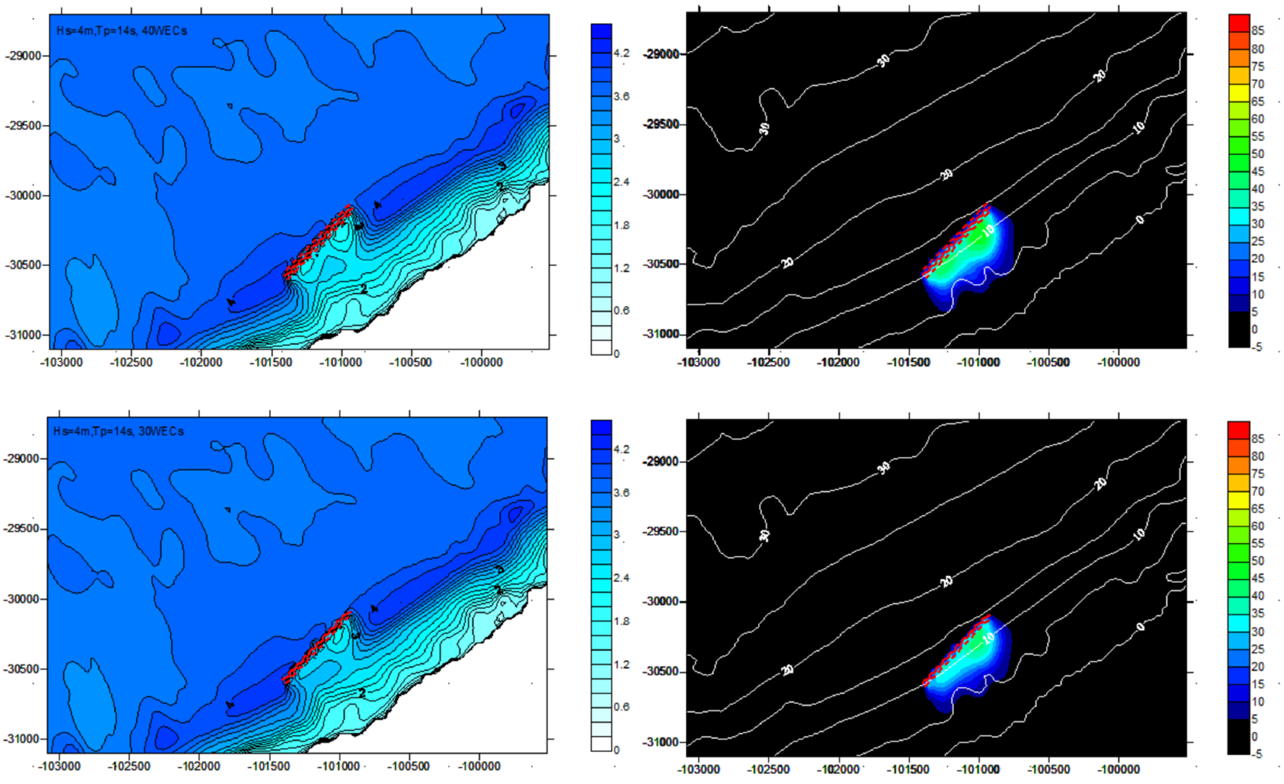

Figure 4.13 Significant wave height (left) in meters and percentage decrease (right) in % for a wave farm of 40 (top) and 30 (bottom) devices (red lines) and initial boundary wave conditions of H_s=4 m, T_p=14 s, Dir=315°. The isobaths are also reported (white lines on the right).

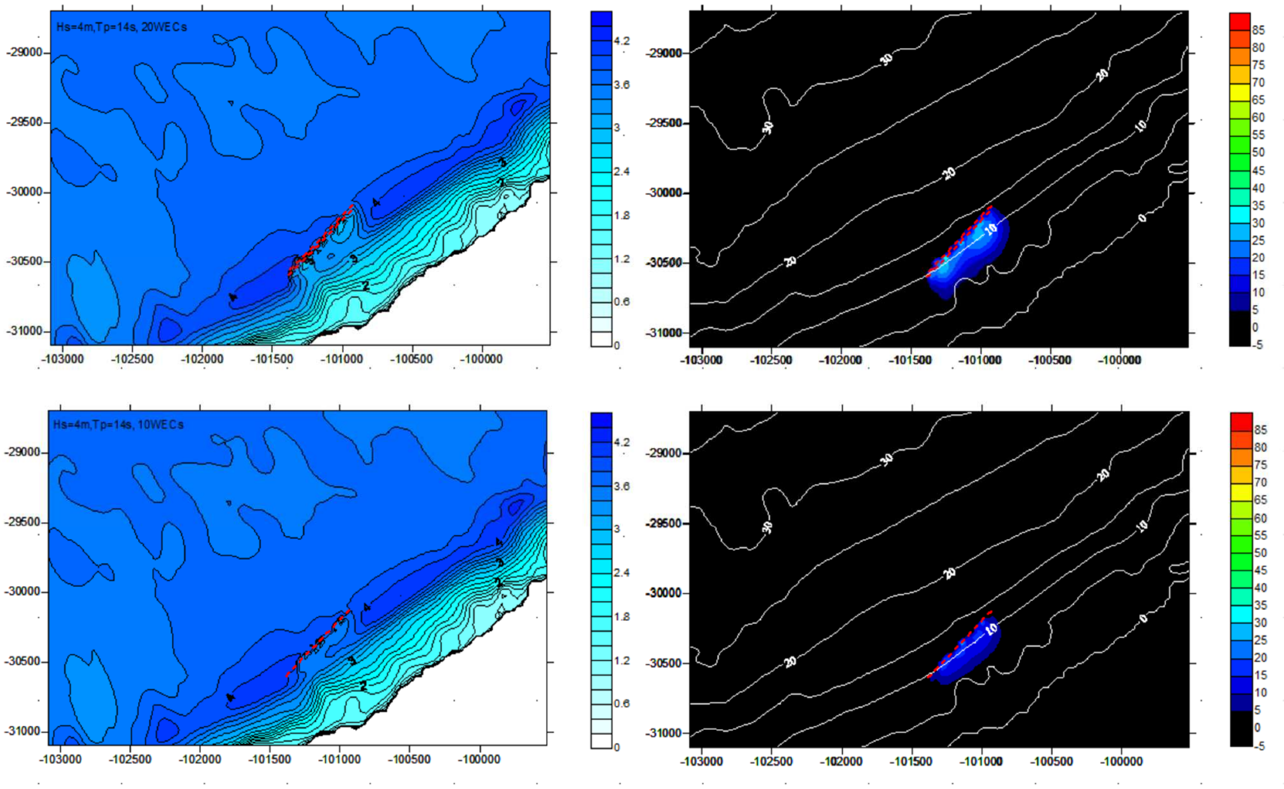

Figure 4.14 Significant wave height (left) in meters and percentage decrease (right) in % for a wave farm of 20 (top) and 10 (bottom) devices (red lines) and initial boundary wave conditions of H_s=4 m, T_p=14 s, Dir=315°. The isobaths are also reported (white lines on the right).

To better understand the effects on the percentage change significant wave height nearshore, only the water depth from 0 to 5 m (which corresponds to a maximum distance from the coastline between 200 and 350 m) were considered (Figure 4.15). From the histograms for the case studies A to F and for 10, 50 and 100 WECs can be concluded that:

- For an array of 10 WECs the percentage change of significant wave height comparing the simulations with and without WECs in the area between the coast and a depth of 5 m is between 0 and 10% in almost 90-100% of the cases, depending on the initial wave conditions; this corresponds to an average change of 0.01 m and a maximum change of 0.23 m (case study C).
- For an array of 50 WECs the percentage change of significant wave height comparing the simulation with and without WECs in the area between the coast and a depth of 5 m is between 0 and 10% in almost 70-90% of the cases, depending on the initial wave conditions; this corresponds to an average change of 0.03 m and a maximum change of 0.25 m (case study D).
- For an array of 100 WECs the percentage change of significant wave height comparing the simulation with and without WECs in the area between the coast and a depth of 5 m is between 0 and 10% in almost 60-80% of the cases, depending on the initial wave conditions; this corresponds to an average change of 0.03 m and a maximum change of 0.27 m (case study D).

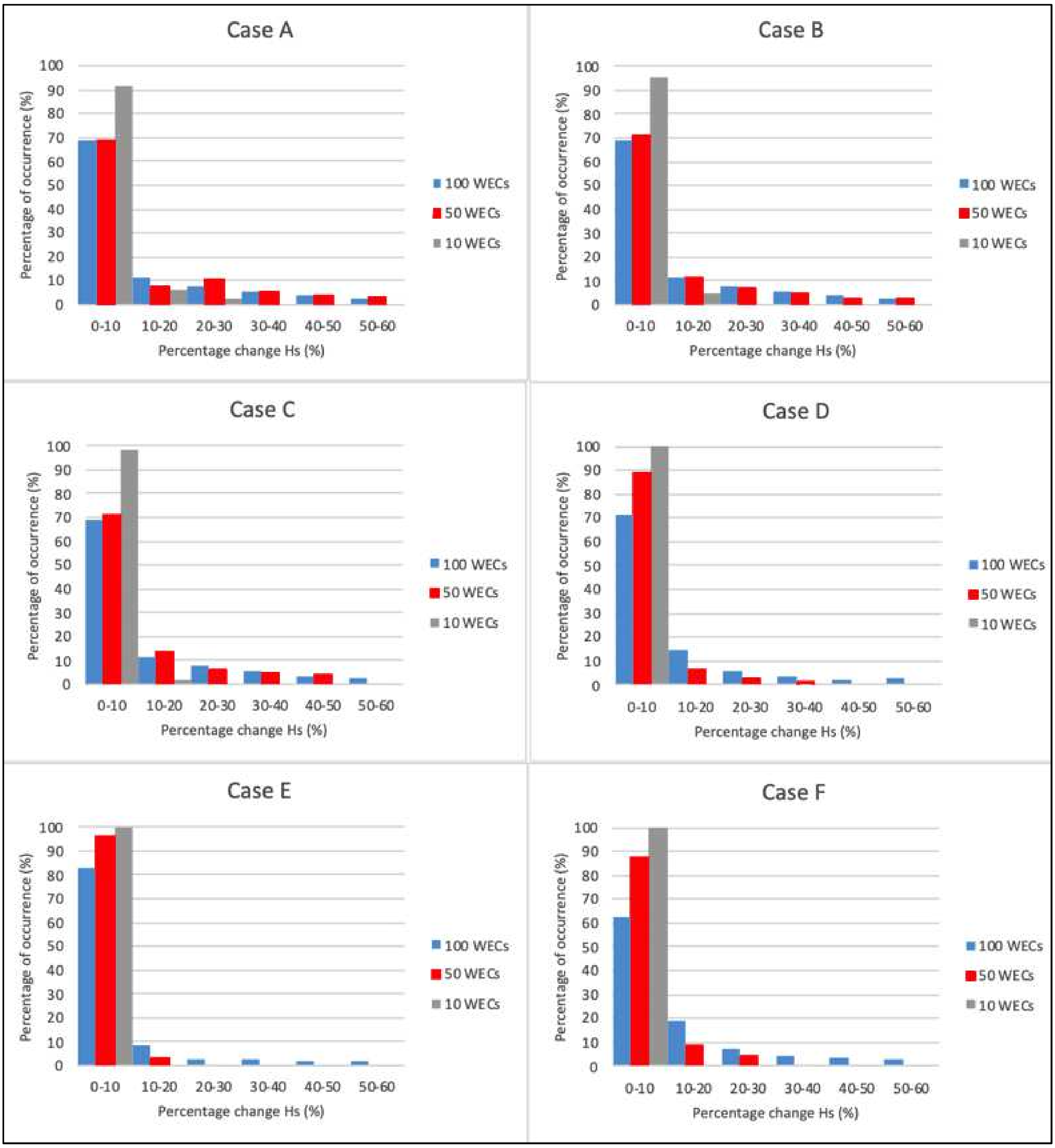

Figure 4.15 Histograms for case studies A to F of percentage change of significant wave height (%) in the nearshore area between 0-5 m depth comparing the baseline case without devices and the cases with 10, 50 and 100 WECs.

4.3.6 WECs effects on wave mean period

The percentage changes in peak period (T_p) in the present study were negligible, such as in a previous similar study by Chang *et al*. (2016). While the mean wave period (T_{m01}) resulted to have both a positive change, which means the mean periods decreased due to the presence of the wave farm and a negative change, which means the mean periods increased due to the presence of the wave farm. As for the significant wave height the mean period percentage change ($T_{m01}\ diff$) between the baseline scenario (that does not include the WECs) and the scenarios with 10 to 100 WECs was calculated as follows:

$$T_{m01}\,diff = \frac{T_{m01} baseline - T_{m01}\,WECs}{T_{m01}\,baseline}\,x\,100 \quad (34)$$

The maximum positive change is reported in Table 4.13 while the maximum negative change is reported in Table 4.14. To better understand what is happening in the presence of the WECs the case with 100 devices and initial conditions A (H_s=2 m, T_p=10 s, Dir=315°) is reported in Figure 4.16. In the lee of the device, there's a negative change, meaning that the period is higher in the presence of the farm, however closer to the coastline the period in the presence of the farm seems to be slightly lower compared to the baseline scenario. In particular, for a farm of 10 WECs the mean period in the lee of the farm increased of maximum 9.46% (case study A), which corresponds to 0.72 s; for a 50 WECs farm it increased of maximum 28.76% (case study A), which corresponds to 1.75 s; for a 100 WECs farm it increased of maximum 33.07% (case study A), which corresponds to 2.79 s. While in the nearshore area between 0 m and 5 m depth for 10 WECs there is a maximum decrease in the mean period of 7.98% (case study A), which corresponds to 0.47 s; for 50 WECs the maximum decrease is of 9.52 % (case study A), which corresponds to 0.56 s; for 100 WECs the maximum decrease is of 9.87 % (case study A), which corresponds to 0.58 s.

Case Study	H_s(m)	T_p (s)	Number of WECs									
			10	20	30	40	50	60	70	80	90	100
A)	2	10	7.98	9.25	9.42	9.54	9.52	9.63	9.51	9.73	9.90	9.87
B)	2	12	2.38	5.98	7.31	9.01	9.04	9.22	9.22	5.37	6.03	9.34
C)	2	14	1.26	2.45	3.82	4.12	4.40	6.62	6.59	6.74	6.70	6.67
D)	3	14	0.55	1.29	2.44	2.63	3.77	4.86	5.85	4.25	6.56	6.63
E)	4	14	0.77	1.19	1.87	1.89	3.07	3.81	4.22	3.40	4.02	4.42
F)	3	16	0.41	2.47	2.60	3.10	3.53	3.67	4.00	2.55	3.52	4.83

Table 4.13 Maximum percentage change of mean wave period (Tm01 diff in %) for case studies A to F and from 10 to 100 WECs.

Case Study	H_s(m)	T_p(s)	Number of WECs									
			10	20	30	40	50	60	70	80	90	100
A)	2	10	-9.46	-13.63	-24.78	-27.57	-28.76	-27.04	-27.69	-26.80	-26.46	-27.03
B)	2	12	-7.30	-12.12	-18.27	-23.44	-27.39	-24.11	-27.12	-25.88	-24.16	-24.58
C)	2	14	-4.71	-8.36	-15.22	-18.67	-21.71	-23.08	-26.34	-25.06	-25.90	-24.44
D)	3	14	-3.28	-6.73	-11.74	-15.38	-19.92	-22.58	-26.28	-28.45	-30.16	-33.07
E)	4	14	-2.83	-5.54	-10.14	-12.64	-16.16	-18.11	-21.32	-23.23	-26.48	-27.91
F)	3	16	-2.33	-4.67	-8.15	-10.52	-13.86	-15.66	-18.24	-20.30	-22.61	-23.97

Table 4.14 Minimum percentage change of mean wave period (Tm01 diff in %) for case studies A to F and from 10 to 100 WECs.

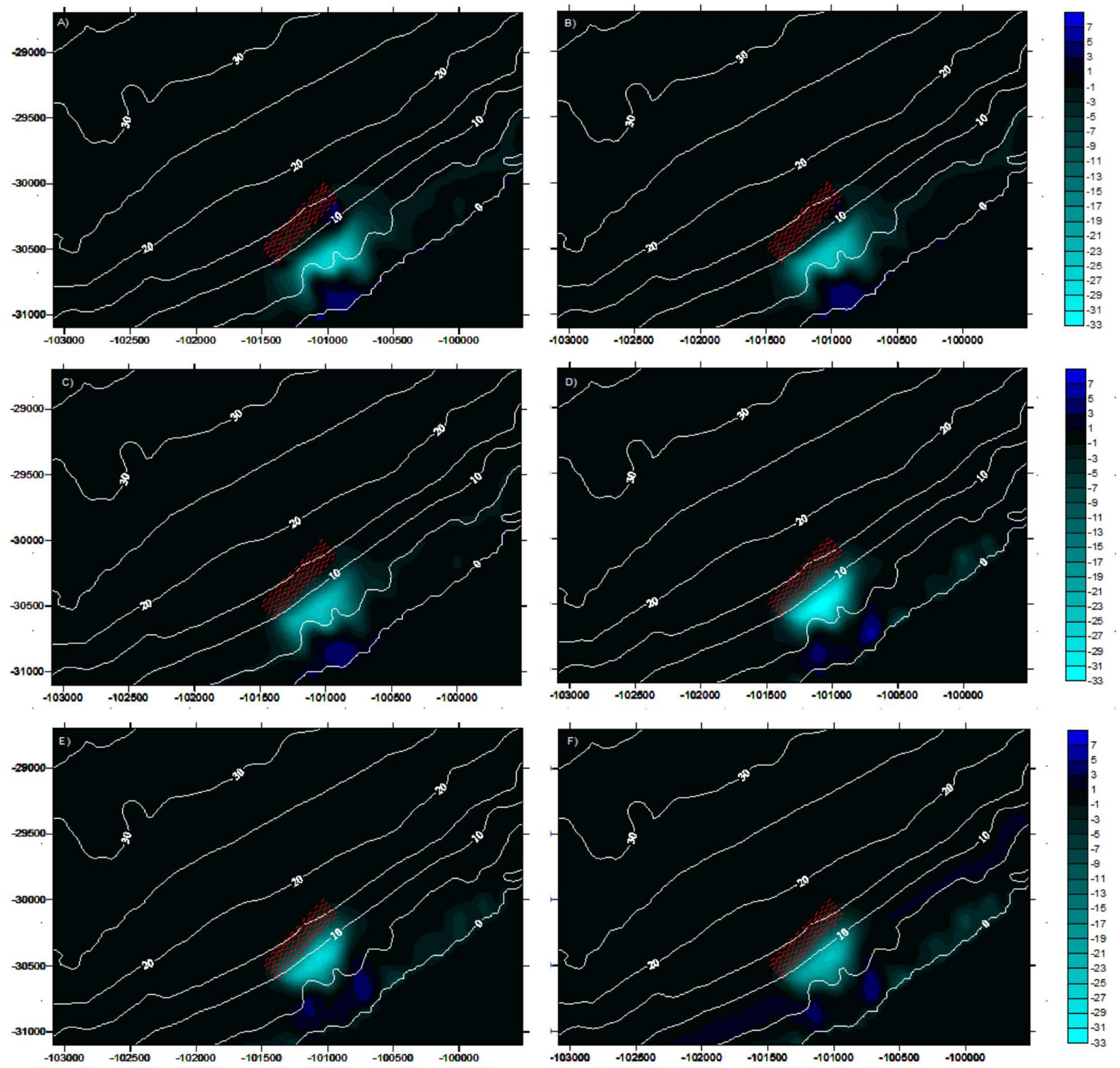

Figure 4.16 Percentage change in mean wave period (Tm01 diff in %) for the cases from A to F and a wave farm of 100 WECs. The white lines are the isobaths, the red lines are the WEC devices.

4.3.7 WECs effects on wave direction

The percentage changes in mean wave direction between the case without WECs (baseline case) and the cases with 10 to 100 WECs have been estimated as follows:

$$Dir\ diff = \frac{Dir\ baseline - Dir\ WECs}{Dir\ baseline} x\ 100 \tag{35}$$

The maximum positive and maximum negative changes are reported respectively in Table 4.15 and Table 4.16. From Figure 4.17, corresponding to the case study A with 100 WECs, it is possible to understand what is happening to the mean wave direction when waves approach the wave farm. The direction of the waves is decreasing in the case of a negative percentage change, meaning that the waves are rotating clockwise, while it is increasing in the case of a positive percentage change, meaning that the waves are rotating counter-clockwise around the wave farm. However, more or less all percentage differences between the baseline scenario and all simulated WEC array are within ±4%, corresponding to ±10° change in mean wave direction. Zero wave direction change is observed in the central part of the lee of the array.

Case Study	H_s(m)	T_p (s)	Number of WECs									
			10	20	30	40	50	60	70	80	90	100
A)	2	10	2.33	2.77	2.76	3.27	3.55	3.03	3.20	3.07	3.84	3.56
B)	2	12	1.63	2.27	1.64	2.48	2.80	2.41	2.67	2.95	2.73	2.82
C)	2	14	0.95	1.34	1.36	1.40	1.86	2.16	2.67	2.54	2.44	2.64
D)	3	14	0.68	1.10	1.06	1.00	1.07	1.51	2.05	2.51	3.11	3.61
E)	4	14	0.78	1.03	0.96	0.87	1.05	1.25	1.42	1.91	2.42	2.84
F)	3	16	0.71	1.01	0.93	1.15	1.04	1.30	1.46	1.71	2.24	2.68

Table 4.15 Maximum percentage change of mean wave direction (Dir diff in %) for case studies A to F and 10 to 100 WECs.

Case Study	H_s(m)	T_p(s)	Number of WECs									
			10	20	30	40	50	60	70	80	90	100
A)	2	10	-2.15	-2.82	-3.56	-4.70	-3.93	-4.90	-5.47	-4.60	-4.57	-5.29
B)	2	12	-1.54	-2.15	-2.06	-3.28	-2.59	-3.48	-3.79	-3.39	-3.18	-3.82
C)	2	14	-0.92	-1.17	-1.53	-2.12	-2.33	-3.03	-2.34	-2.83	-2.82	-2.93
D)	3	14	-0.65	-0.97	-1.21	-1.78	-2.32	-3.01	-3.44	-3.64	-3.78	-3.85
E)	4	14	-0.69	-0.87	-1.26	-1.68	-2.27	-2.76	-3.24	-3.82	-4.17	-4.51
F)	3	16	-0.71	-0.93	-1.03	-1.48	-1.87	-2.25	-2.65	-3.08	-3.34	-3.74

Table 4.16 Minimum percentage change of mean wave direction (Dir diff in %) for case studies A to F and 10 to 100 WECs.

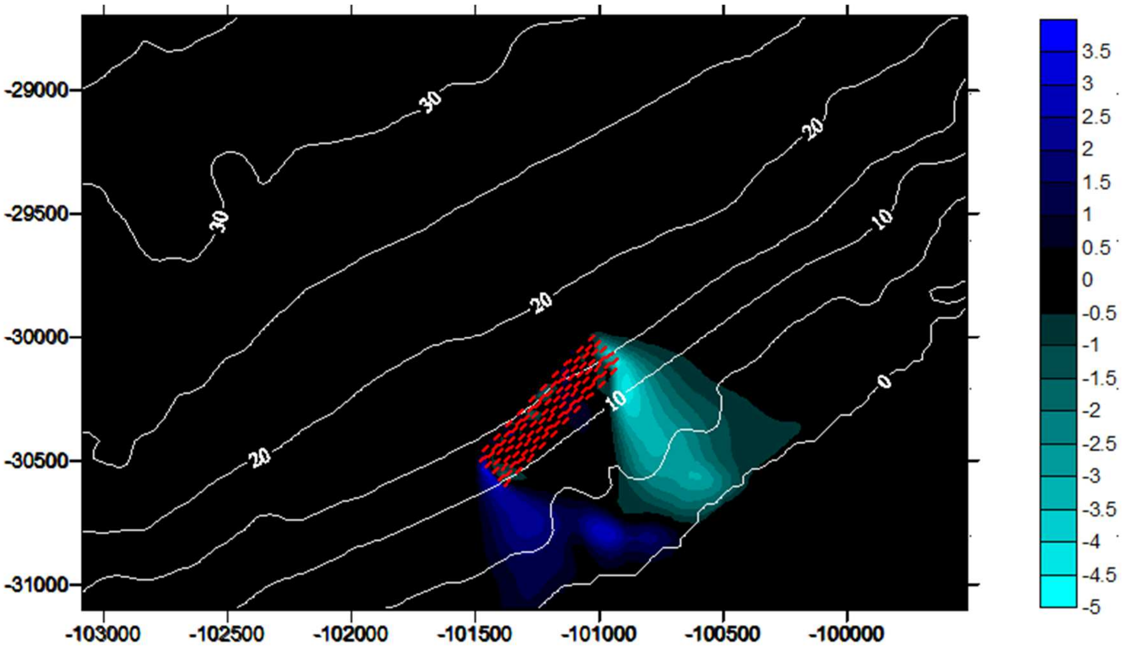

Figure 4.17 Percentage change in mean wave direction (Dir diff in %) for case study A (Hs=2m, Tp=10s, Dir=315°) and a wave farm of 100 WECs. The white lines are the isobaths, the red lines are the WEC devices.

4.3.8 Real sea states

To study the behaviour of a wave farm in real sea state conditions, 19 years of wave climate have been simulated (from 2000 to 2018). The initial wave conditions were extracted from ECMWF database at the point located at the top left corner of the main grid at a depth of around 1700 m (with coordinates -8°7'59.599" W, 39°40'7.017"N, EPSG:4326 WGS 84 coordinate system). A wave farm of 50 devices was chosen as the most realistic worst scenario and the WECs have been arranged in alternated lines of 10 WECs each (configuration 2) with spacing between aligned devices equal to 50 m and spacing between lines of 20 m, as defined in subsection 4.3.3. As output locations 30 reference points have been chosen (shown in Figure 4.18), of which 3 are located before the wave farm (Point 1, Point 2, Point 3) and 27 are located in the lee of the wave farm (from Point 4 to Point 30), between a depth of 12 m and 0 m.

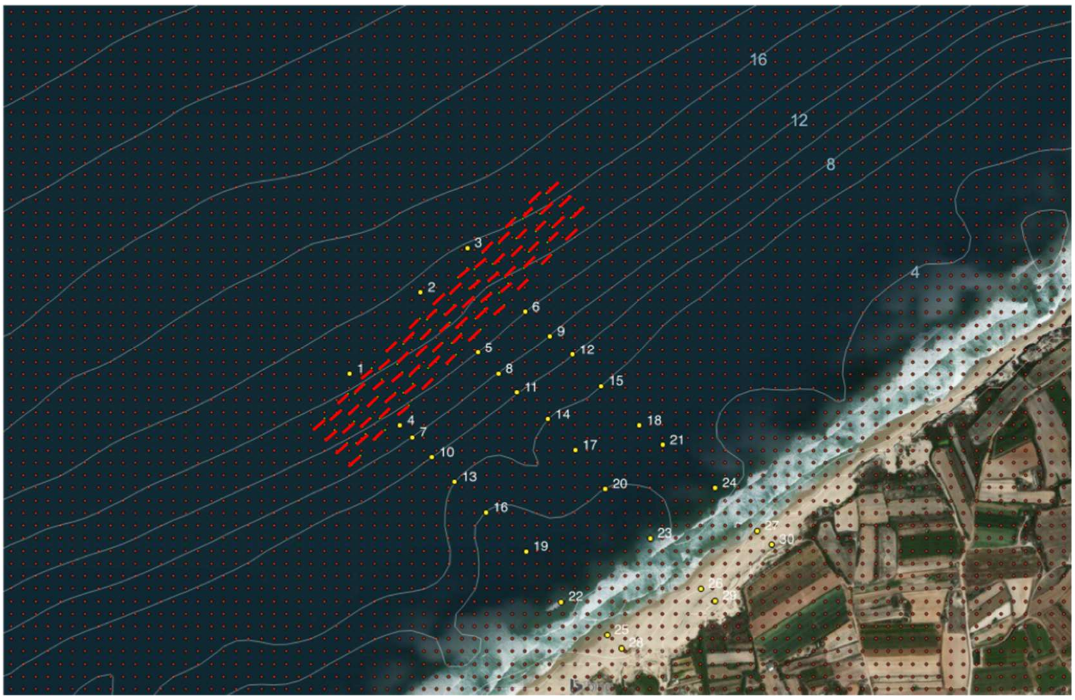

Figure 4.18 Second nested grid with an array of 50 WECs of WaveRoller type (in red) with spacing 50 m. The output locations of the SNL-SWAN model simulations are reported (in yellow) and numbered along with the bathymetric contour lines (in m) of the area.

4.3.8.1 Model set-up

For the 19 years simulation three computational grids have been used, the same already mentioned in Table 3.2 but with different cell size, to optimize the computational time). The main and first nested grids have a bathymetric resolution of 103.16 m and computational resolution of, respectively, 500 m and 250 m. The second nested grid has instead a higher bathymetric resolution of 30 m and a computational resolution of 25 m, which will allow to better simulate the waves in the coastal area where the wave farm is located. The input wave climate data were taken from ECMWF database and are: significant wave height, peak period and mean direction every 6 hours. Those wave climate input data have already been analysed in section 3.4 and are here used again as input for the SNL-SWAN simulations. The frequency resolution range is different for each input file because it has been estimated with equation (29) for the lower frequency and equation (30) for the higher frequency, as explained in subsection 4.2.3. This was necessary because the sensitivity analysis of SNL-SWAN (section 4.2) showed that the model is not working properly with the standard frequency resolution range of 0.04 Hz and 1 Hz. The UNIX version of SNL-SWAN model (*snl-swan-unix-ser-ifort.exe*) was run in parallel for a period of 19 years (from 2000 to 2018) using the Medusa cluster infrastructure. Since OBCASE 1 has been proven to give always higher differences in the wave propagation compared to OBCASE 2, the simulations were only performed with OBCASE 1 to have a worst-case scenario.

4.3.8.2 Time series analysis

The results obtained from the 19 years simulation are here reported along with an accurate analysis of the wave conditions at several locations, before and after the wave farm. This was performed in terms of significant wave height but also mean wave direction to assess any change in the currents around the devices. The main objective of this analysis is to study in more detail the wave transformation immediately in the lee of the WaveRoller type WECs farm and the adjacent coastal area. As can be seen from Figure 4.19, the wave farm captures the wave energy flux from the incoming waves (Point 2) and, as a result, the waves are of lower height in the region behind the devices (Point 5). The monthly and annual mean, maximum and minimum percentage decrease in significant wave height between Point 2 and Point 5 is reported in Table 4.17 and Table 4.18. What can be observed is that there is a stronger variability on a monthly base rather than on an annual base. From the seasonal histograms of percentage decrease in significant wave height (Figure 4.20) can be seen how there is a clear shift toward lower wave heights after the wave farm (Point 5).

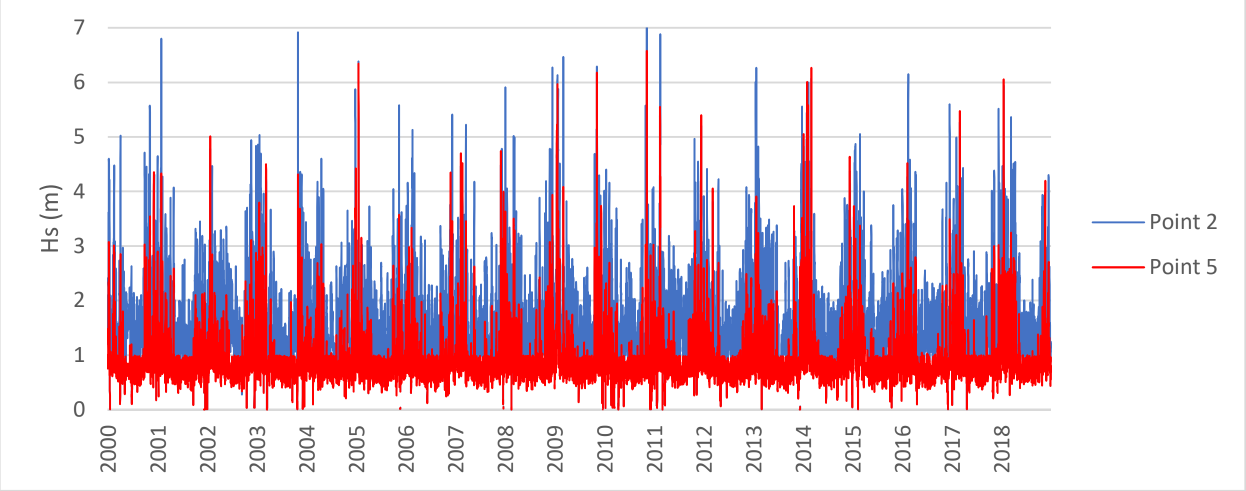

Figure 4.19 Time series of significant wave height Hs (in m) at a location before the wave farm (point 2) and after the wave farm (point 5) simulated with SNL-SWAN for the years 2000-2018.

	MEAN (%)	MAX (%)	MIN (%)
Jan	46.19 ± 11.63	83.54	0.05
Feb	46.49 ± 11.97	84.27	0.01
Mar	48.48 ± 12.80	84.61	0.02
Apr	47.98 ± 16.22	84.96	0.01
May	46.89 ± 18.84	84.57	0.02
Jun	42.64 ± 21.41	83.67	0.00
Jul	43.82 ± 21.97	83.67	0.00
Aug	43.59 ± 21.74	84.16	0.00
Sep	42.90 ± 18.69	81.65	0.00
Oct	45.92 ± 15.90	83.98	0.01
Nov	48.78 ± 13.49	84.41	0.09
Dec	45.81 ± 14.36	90.40	0.01

Table 4.17 Monthly mean, maximum and minimum values of percentage decrease in significant wave height between a point before the wave farm (point 2) and a point after the wave farm (point 5) for the simulated period 2000-2018.

	MEAN	MAX	MIN
2000	45.45 ± 18.29	82.14	0.00
2001	47.23 ± 15.76	82.73	0.04
2002	46.84 ± 15.90	83.46	0.02
2003	42.53 ± 18.90	84.10	0.00
2004	46.64 ± 16.73	84.41	0.02
2005	45.92 ± 17.69	83.72	0.01
2006	44.22 ± 17.49	74.25	0.02
2007	45.27 ± 16.37	84.55	0.01
2008	47.38 ± 15.56	84.25	0.01
2009	45.39 ± 16.61	83.06	0.00
2010	46.55 ± 17.83	84.57	0.02
2011	45.36 ± 17.00	83.67	0.00
2012	45.23 ± 17.55	83.75	0.05
2013	46.45 ± 18.04	84.96	0.04
2014	44.32 ± 17.46	74.09	0.01
2015	47.18 ± 16.36	90.40	0.01
2016	46.65 ± 16.61	87.89	0.01
2017	44.70 ± 18.38	82.14	0.01
2018	47.13 ± 14.77	83.98	0.00

Table 4.18 Annual mean, maximum and minimum values of percentage decrease in significant wave height between a point before the wave farm (point 2) and a point after the wave farm (point 5).

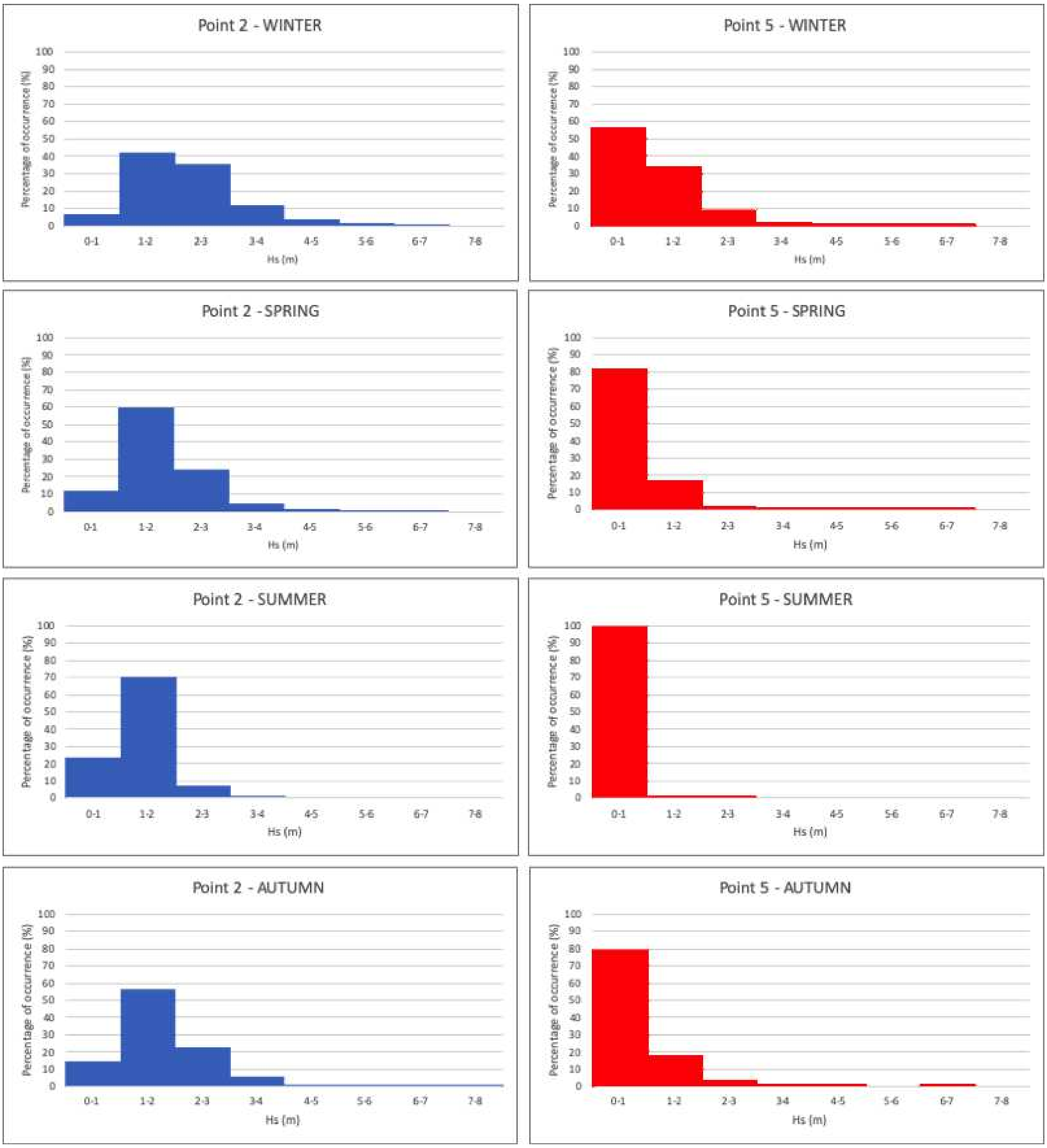

Figure 4.20 Histograms od percentage of occurrence of significant wave height Hs (in m) for winter (December, January, February), spring (March, April, May), summer (June, July, August) and autumn (September, October, November). Point 2 is located before the wave farm, point 5 is located in the lee of the wave farm.

4.3.8.3 *WECs effect on wave power resource*

The wave power resource, or wave energy flux per unit of wave-crest length, has been calculated with equation (22) before the wave farm and after the wave farm (Figure 4.21). The difference between the energy flux before and after the waves cross the devices does not represent the energy extracted by the wave farm. However, it helps understanding how much the wave power resource is decreasing due to the presence of the WECs that can imply changes in the flow field around the wave farm. The mean wave energy flux per unit of wave-crest length at point 2 is 18.9 ± 23.7 kW/m while at point 5 is 5.9 ± 12.3 kW/m, which is three times less.

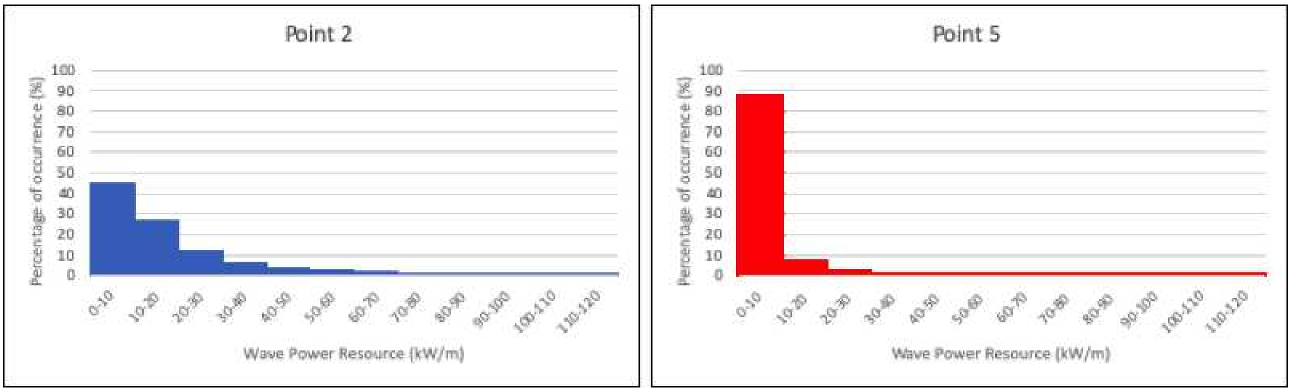

Figure 4.21 Percentage of occurrence (in %) of energy flux per unit of wave-crest length (in kW/m) available at Point 2 and Point 5.

4.3.8.4 WECs effect on mean wave direction

The goal of this study was to quantitatively characterize the environments where WEC devices may be installed and to assess effects of WECs on the hydrodynamic but not on the local sediment transport. However, there can be changes in the patterns of sediments dynamics and circulation due to the presence of WEC devices. This is because waves are the main source of shear stress at the sediment bed in the nearshore region and they can cause resuspension of sediment and, once suspended, sediments will be transported by the combined currents produced by waves and tides. Therefore, even if SNL-SWAN is not a sediment transport model, it allows to identify changes in wave direction due to the presence of the WEC array. In particular, from the histograms of percentage of occurrence of mean wave direction before the wave farm (at location 2) and after the wave farm (at locations 4 and 6), it is possible to observe some changes (Figure 4.22). For instance, in point 4 and 6 the directions increase compared to point 2, meaning that there is a clockwise rotation in the direction of the waves at both sides of the wave farm.

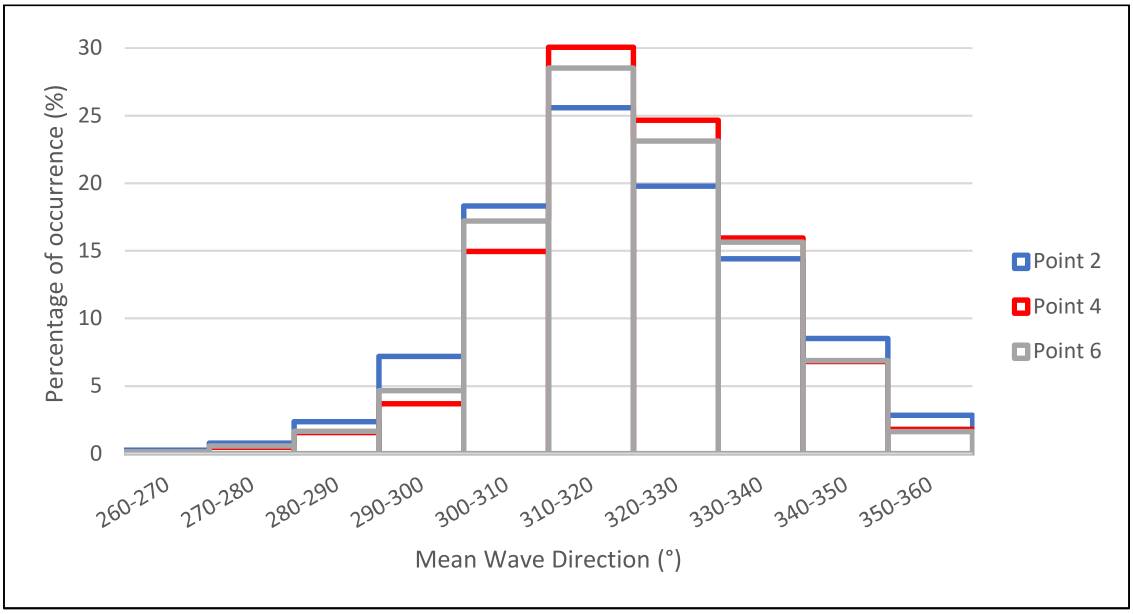

Figure 4.22 Histograms of percentage of occurrence of mean wave direction (in °) at Point 2 (in blue) before the wave farm and Point 4 (in red) and 6 (in grey) after the wave farm for the period from 2000 to 2018.

4.3.9 WEC devices comparison

To investigate the levelized coast of energy (LCOE) for a Bombora wave farm, a study in 2016 investigated the economics of a 60MW wave farm consisting of 40 WECs in Praia de Almagreira (Bombora Wavepower, 2016). In the present study, the same WECs configuration was considered to simulate the effects of the farm on the significant wave height, peak period and mean direction of the incoming waves. The results have been compared to a similar wave farm of bottom-fixed oscillating flap devices to understand the differences between the two kinds of farms, Bombora and WaveRoller. The WaveRoller array configuration and spacing between devices were chosen to be the most comparable with the Bombora array.

The characteristics of both farms are reported in Table 4.19 and two different configurations have been tested:

- with the devices aligned in a direction perpendicular to the incoming waves of 315°, which is the optimal configuration for the WaveRoller type of WECs (reported in orange in Figure 4.24 and Figure 4.25) and corresponds to $\alpha = 0°$ in Figure 4.23;
- with the devices aligned in a direction rotated of $\alpha = 30°$ with respect to the previous one, which is the configuration suggested by Algie *et al.* (2017) for the Bombora type of WECs on the coast of Peniche (reported in green in Figure 4.24 and Figure 4.25).

	WaveRoller type	Bombora type
WECs length	25 m	75 m
WECs spacing	45 m	60 m
WECs number	40	40
WECs orientation	Aligned with wave crest	Perpendicular to wave crest

Table 4.19 WECs characteristics in the farm for the WaveRoller and Bombora type. The spacing in the case of Bombora includes the diameter of 15 m and the actual distance between WECs of 45 m. The WECs orientation refers to waves coming from 315°.

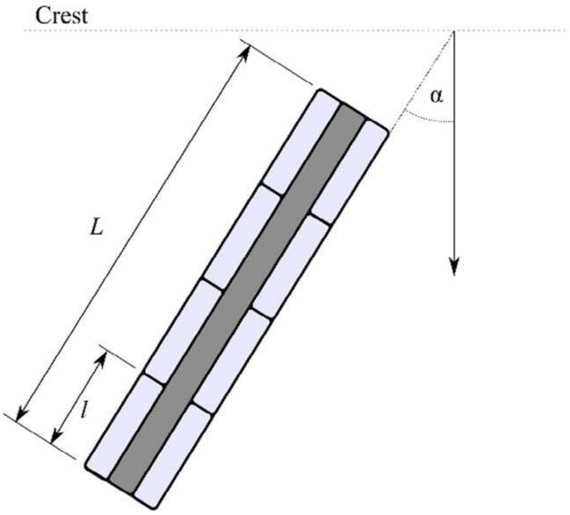

Figure 4.23 Bombora WEC orientation with respect to incoming waves. Source: Algie et al. *(2017).*

Figure 4.24 Location and disposition of the wave farm of 40 WECs of WaveRoller kind. The orange WECs refers to the configuration perpendicular to the incoming waves of 315° while the green WECs refers to the same configuration rotated of 30°.

Figure 4.25 Location and disposition of the wave farm of 40 WECs of Bombora kind. The orange WECs refers to the configuration perpendicular to the incoming waves of 315° while the green WECs refers to the same configuration rotated of 30°.

Both devices have been simulated under initial wave conditions from A to F, angle of inclination α=0° and 30° and with SNL-SWAN OBCASE 1 and 2. It was decided to test again the OBCASE 2 to see if with a different device the results would change. The *q*-factor was then estimated because it can give a measure of the overall constructive (*q*-factor > 1) or destructive (*q*-factor < 1) interactions between the single devices within the array in terms of performance. The *q*-factor results are summarised in Figure 4.26, while the total power absorbed (in kW) by the 40 WECs array of both types (Bombora's mWave and WaveRoller) is reported in Figure 4.27. Moreover, the ratio between the mean power absorbed (in kW) by a single WaveRoller WEC and the mean power absorbed by a single Bombora's mWave WEC was calculated and is reported in Table 4.20. From the comparison of the two types of devices can be concluded that:

- For the WaveRoller type of WECs the optimal wave farm configuration (which means higher *q*-factors) is with an angle of inclination α = 0° (as already demonstrated in subsection 4.3.4);
- For both devices, OBCASE 1 gives higher performance then OBCASE 2 because, as already mentioned in subsection 4.2.5.2, the devices resulted to absorb more energy when the power matrix is used instead of the RCW curve. The total power absorbed by both the WEC types is higher for OBCASE 1 than for OBCASE 2 (Figure 4.27);

- Among all the simulated case studies for both devices the higher performance is obtained for case study E, which corresponds to H_s = 4 m, T_p = 14 s and Dir = 315°, while the lower performance is obtained for case study A, which corresponds to H_s = 2 m, T_p = 10 s and Dir = 315°;
- The array of 40 WaveRoller type devices showed an overall higher performance if compared to the array of 40 Bombora's mWave type devices, this is due to the different power matrix (reported in Figure 2.7 and Figure 2.10) that is therefore largely influencing the simulated absorbed power.

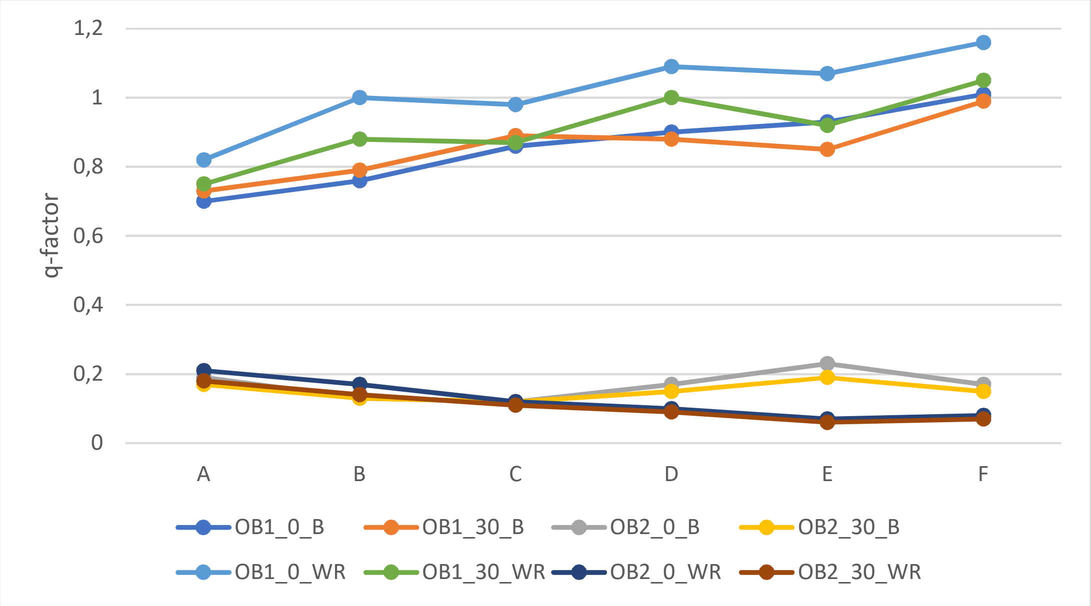

Figure 4.26 Q-factor for two different WEC devices, Bombora type (B) and WaveRoller type (WR), obtained from the simulation of case studies A to F, with SNL-SWAN OBCASE 1 and 2 and for a configuration perpendicular to waves coming from 315° (α=0°) and a configuration clockwise rotated of α=30°.

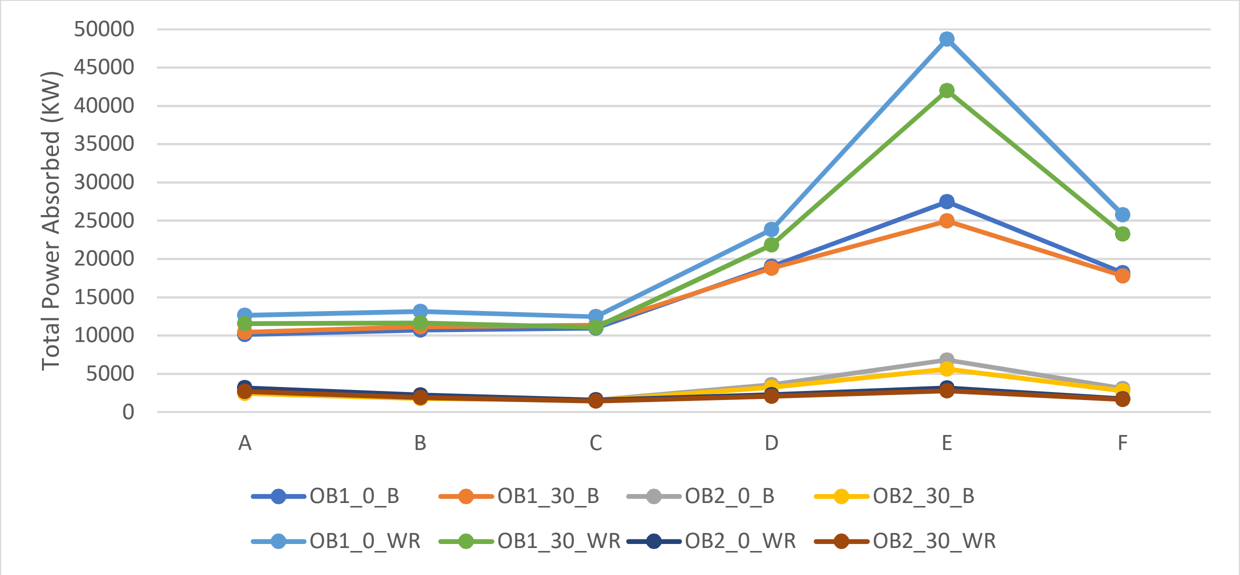

Figure 4.27 Total power absorbed (in kW) by a farm of 40 aligned WECs of Bombora type (B) and WaveRoller type (WR). The values are obtained from the simulation of case studies A to F, with SNL-SWAN OBCASE 1 and 2 and for a configuration perpendicular to waves coming from 315° (α=0°) and a configuration clockwise rotated of α=30°.

Ratio of power absorbed	OB1_0	OB1_30	OB2_0	OB2_30
A	1,24	1,11	1,17	1,10
B	1,23	1,05	1,23	1,08
C	1,14	0,98	1,00	0,94
D	1,25	1,16	0,63	0,63
E	1,77	1,68	0,46	0,50
F	1,41	1,31	0,57	0,59

Table 4.20 Ratio between the power absorbed by a single WaveRoller WEC and a single Bombora's mWave WEC. The values are obtained from the simulation of case studies A to F, with SNL-SWAN OBCASE 1 and 2 and for a configuration perpendicular to waves coming from 315° ($\alpha=0°$) and a configuration clockwise rotated of $\alpha=30°$.

Case study A and E have been analysed in more detail because they resulted to be respectively the case with minimum and maximum total power absorbed. The percentage change in significant wave height has been calculated for both kind of devices and OBCASEs (Figure 4.28, Figure 4.29, Figure 4.30 and Figure 4.31) and the following observations can be done:

- OBCASE 1 (Figure 4.28 and Figure 4.29) always gives higher significant wave height percentage decrease when compared to OBCASE 2 (Figure 4.30 and Figure 4.31) for both devices and initial conditions (note that OBCASE 2 has a different scale);
- The study case A with lower initial significant wave height (H_s = 2 m) resulted to have a higher percentage change in significant wave height in the lee of both the arrays (with a maximum of 52.37% change obtained with the WaveRoller type array with configuration α = 30° and OBCASE 1);
- The study case F with higher initial significant wave height (H_s = 4 m) resulted to have a higher percentage change in significant wave height (with a maximum of 29.92% change obtained with the WaveRoller type array with configuration α = 30° and OBCASE 1);
- Maximum changes in H_s are always found in the lee of the wave farm, while closer to the coastline (between 0 and 5 m of depth) they decrease to 0-10%;
- Changes in wave peak period are negligible: mostly equal to 0% with some cases of 10% decrease between the baseline scenario and simulated scenario, which corresponds to around 1 s difference;
- Changes in wave mean period are negligible: mostly equal to 0% with some cases of 5% decrease between the baseline scenario and simulated scenario, which corresponds to around 0.5 s difference;
- Changes in mean wave direction ranges between ±2% which corresponds to a difference raging between ±8°.

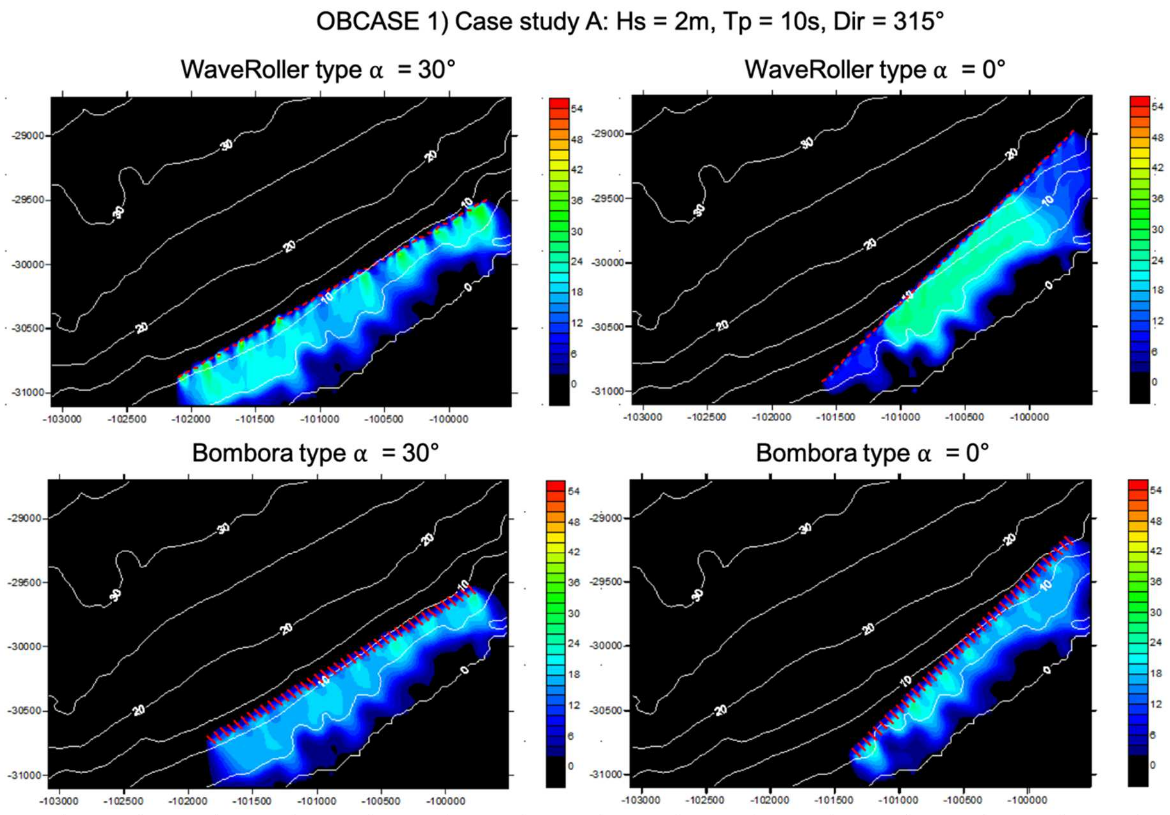
OBCASE 1) Case study A: Hs = 2m, Tp = 10s, Dir = 315°

WaveRoller type α = 30°

WaveRoller type α = 0°

Bombora type α = 30°

Bombora type α = 0°

Figure 4.28 Significant wave height percentage decrease (%) from the baseline scenario for a 40 WECs array (in red) of WaveRoller type (top) and Bombora type (bottom) located perpendicular to the incoming waves (right) or rotated of 30° (left). The bathymetric contours are also reported.

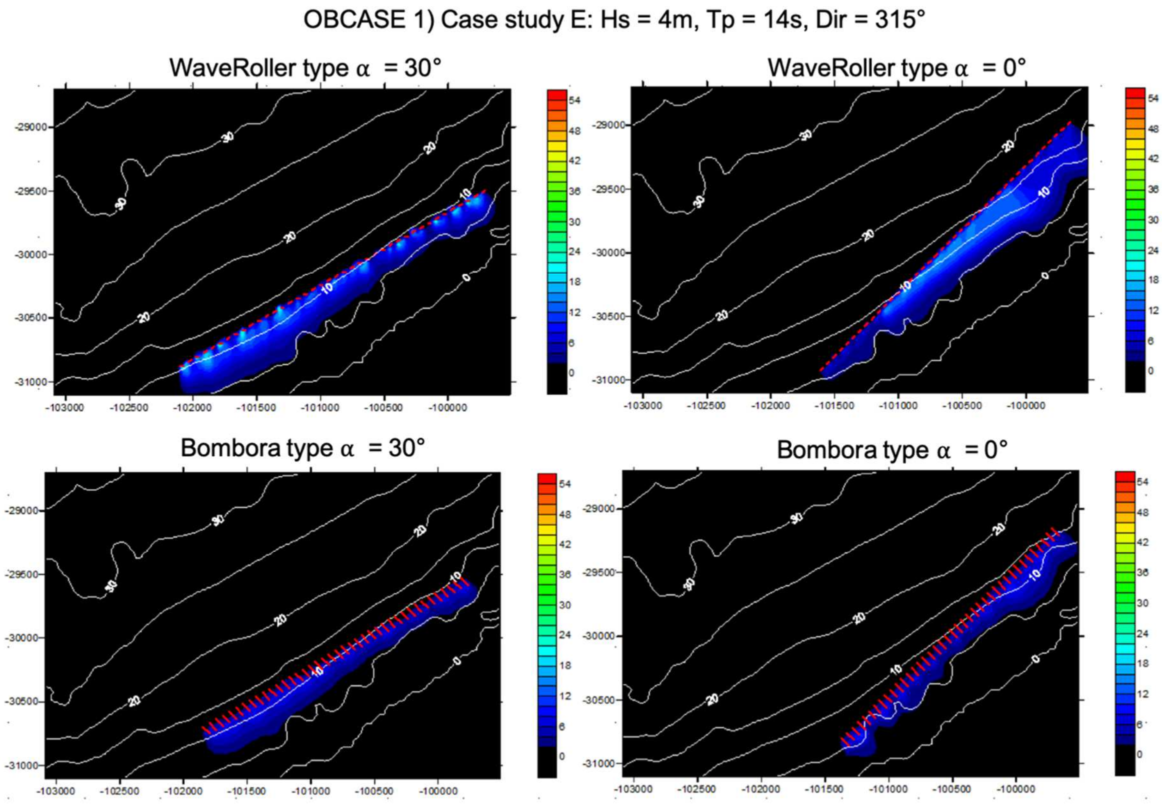
OBCASE 1) Case study E: Hs = 4m, Tp = 14s, Dir = 315°

WaveRoller type α = 30°

WaveRoller type α = 0°

Bombora type α = 30°

Bombora type α = 0°

Figure 4.29 Significant wave height percentage decrease (%) from the baseline scenario for a 40 WECs array (in red) of WaveRoller type (top) and Bombora type (bottom) located perpendicular to the incoming waves (right) or rotated of 30° (left). The bathymetric contours are also reported.

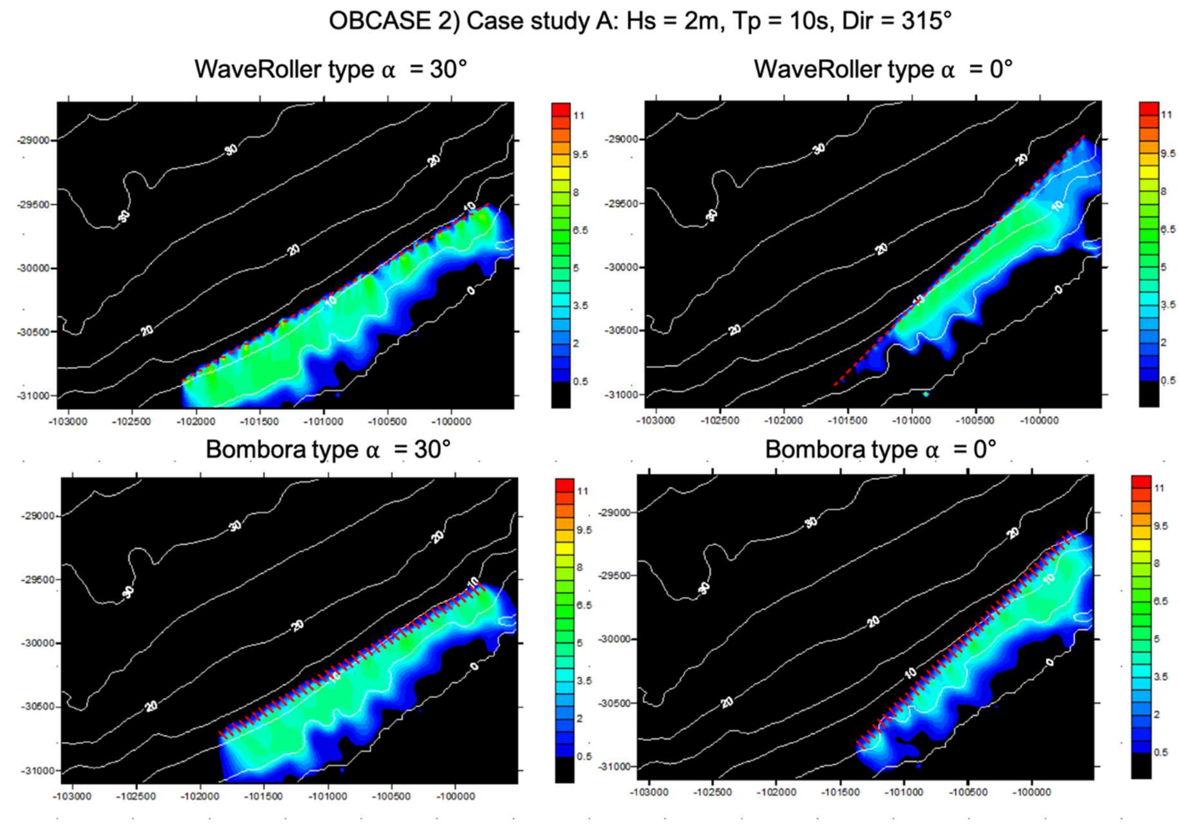

Figure 4.30 Significant wave height percentage decrease (%) from the baseline scenario for a 40 WECs array (in red) of WaveRoller type (top) and Bombora type (bottom) located perpendicular to the incoming waves (right) or rotated of 30° (left). The bathymetric contours are also reported.

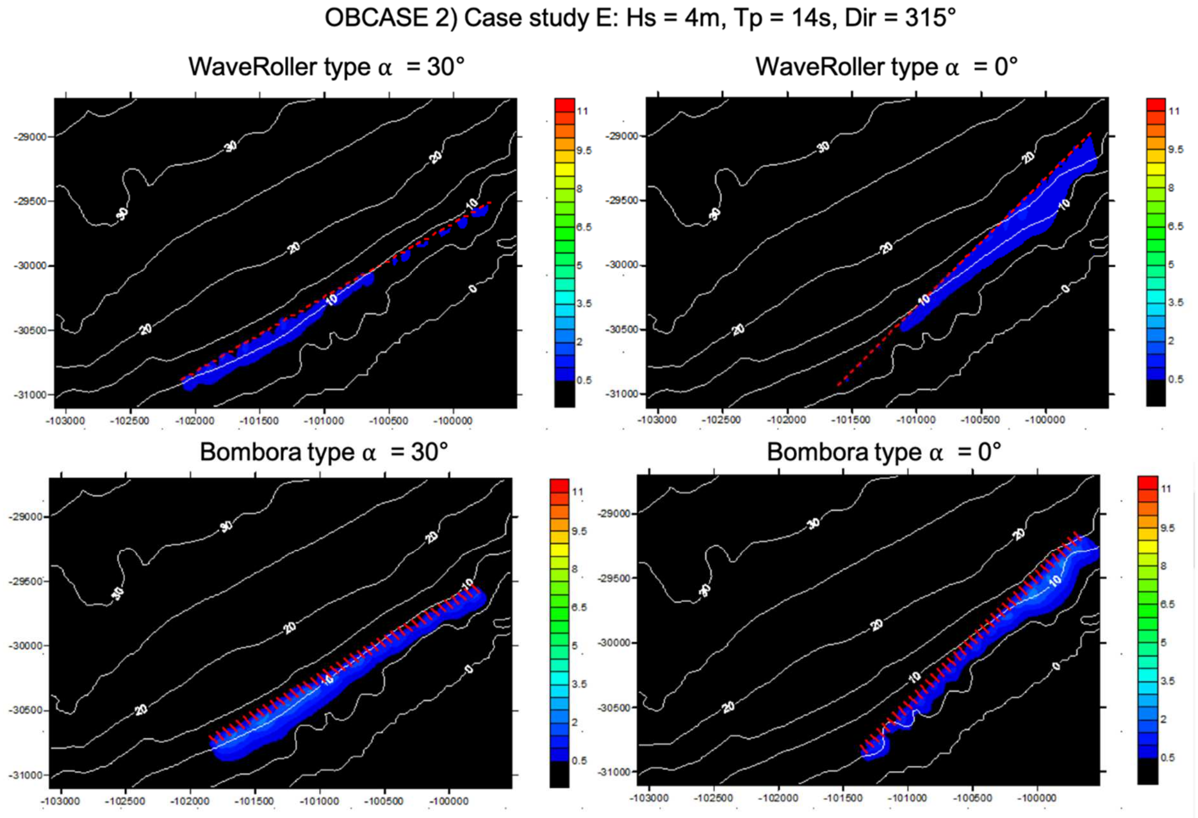

Figure 4.31 Significant wave height percentage decrease (%) from the baseline scenario for a 40 WECs array (in red) of WaveRoller type (top) and Bombora type (bottom) located perpendicular to the incoming waves (right) or rotated of 30° (left). The bathymetric contours are also reported.

5 | Discussion

The main objective of the present work was to study the impact of wave farms on the wave propagation near the coastline of Almagreira beach, north of Peniche. To accomplished that, the SNL-SWAN wave model was used and an overview of its application is here presented and discussed.

As a preliminary step, initial site-specific wave model validation was accomplished using the native SWAN model for a three nested-grid domain because it is equivalent to SNL-SWAN for cases without obstacles. The model domain boundary wave conditions were determined from the European Centre for Medium-Range Weather Forecasts (ECMWF) database for a period of 9 years (2010-2019). The results from SWAN model simulations have been validated against in-situ data from the Nazaré Costeira buoy, located at a depth of around 90 m. The model performance statistics computed showed agreement between modelled and measured data with a high level of confidence, therefore allowing to employ the SWAN model with high level of confidence for hindcasting of the wave parameters in the specific area of Almagreira beach.

Once validated the model, a wave and wave power characterization has been performed to characterize the sea states of interest. In particular, it is fundamental to characterize the local directional spread of sea states because wave energy converters (WECs) efficiency is directionally dependent and the direction of the incoming waves affects the wave shadow in the lee of the farm. There are already previous assessments of the wave power resource: the first for Portugal continental coast, based on thirty three years of wave hindcast (1979-2012) with two spectral models, WAVEWATCHIII and SWAN, by Silva *et al.* (2018); the second for the coastal area north of Peniche for an eight-year period (2005-2012) with SWAN by Silva *et al.* (2016).

In order to assess the wave regime at the exact location of Almagreira beach the SNL-SWAN model was run for 19 years of ECMWF data with a three nested-grid domain. By multiplying the average energy flux per wave front length, the average annual number of hours and the probability of occurrence of each sea state it was possible to obtain the average annual energy per unit wave crest length available in each sea state. From that, six most common and energetic sea states offshore Almagreira beach have been identified with the following characteristics: case A, with H_s = 2 m and T_p = 10 s; case B, with H_s = 2 m and T_p = 12 s; case C, with H_s = 2 m and T_p = 14 s; case D, with H_s = 3 m and T_p = 14 s; case E, with H_s = 4 m and T_p = 14 s; case F, with H_s = 3 m and T_p = 16 s. The main direction of incoming waves resulted to range between 290° and 340 °, which corresponds to the North-West.

Under those six wave regimes, a SNL-SWAN model sensitivity study was conducted in the presence of an array of 10 bottom-fixed oscillating wave surge device of the type WaveRoller. The model runs were conducted using a two-nested grid domain instead of three to save computational time. The most important outcome from the sensitivity analysis regards the computational spectral grid. The recommended frequency range by SWAN user manual (Ruehl *et al.*, 2014) in coastal areas is $0.04 \leq f \leq 1.00\ Hz$. However, it was found out that for the present study that, for boundary initial peak periods higher than 10 s, when WECs are introduced in the nested domain unreliable results are produced. Therefore, in the simulations was necessary to set different frequency ranges for the six case studies depending on the SNL-SWAN input peak period, calculated with the equations reported in subsection 4.2.3.

SNL-SWAN includes a frequency-dependent WEC module that, based on the WEC's power performance, calculates the transmission coefficients. It has been already demonstrated by Stokes & Conley (2018) that frequency-dependent modelling (i.e. with SNL-SWAN) can give a more precise representation of energy extraction than frequency-independent modelling (i.e. SWAN) with a single transmission coefficient applied for the entire WEC array. This is true for cases where the WEC absorption characteristics (power matrix or relative capture width curve) are defined and available. For the present study, the exact WaveRoller power matrix is not available, therefore the power matrix of a similar device was considered, a bottom-fixed oscillating flap with 26 m length (Babarit *et al.*, 2012).

With that power matrix, the SNL-SWAN five obstacle cases (OBCASEs) have been evaluated, with OBCASE 0 being equal to the native SWAN model, as expected from Chang *et al.* (2016); OBCASE 3 and 4 not working at all, due to a bug into the code of the SNL-SWAN version used for the present work; OBCASE 1 giving higher percentage decreases in significant wave height and more power absorption than OBCASE 2. However, since SNL-SWAN is a recent modification of SWAN (Ruehl *et al.*, 2013), it was possible to compare the results from the present study only with two previous studies, by Ruehl *et al.* (2015) and by Chang *et al.* (2016). They both found that OBCASE 2 simulated wave height reductions in the lee of the devices were consistently higher than those modelled using SNL-SWAN OBCASE 1. According to Chang *et al.* (2016), these differences are likely due to the data interpolation necessary for computing the RCW curve used in OBCASE 2. A plausible reason for this difference between the results by Ruehl *et al.* (2015) and by Chang *et al.* (2016) and the results from the present work was identified. This is that the relative capture width curve used in the present study as an input for the simulations with OBCASE 2 was not obtained from a company or from the literature. It was instead calculated from the power matrix values of power absorbed and the simulated incoming power. A better investigation of the differences between this study and previous applications of SNL-SWAN could help improving the WEC module.

In any case, being the aim of the present work to to examine the effects of WECs on near-field and far-field wave conditions in the lee of the farm, OBCASE 1 was preferred to perform all the following analysis because, in this specific case and according to the principle of precaution, it represents the worst-case scenario in terms of changes in significant wave height if compared to OBCASE 2.

With OBCASE 1 and the six selected sea states, SNL-SWAN simulations were performed to examine the effects of WEC variations (WEC farm configuration, spacing of the WEC devices within the array, number of WEC devices in an array) in the lee of the farm. The installation of a wave farm will affect the surrounding environment at various levels: it will alter patterns of wave propagation, circulation patterns and processes of the local ecosystem. Different configurations of the farm may, therefore, produce different impacts on this environment. In the literature, there have been several attempts to understand the dynamics and interactions of multiple WECs (Babarit, 2010; Borgarino *et al*. 2012; Child & Venugopal, 2010; Cruz *et al*., 2009; Renzi *et al*., 2014; Wolgamot *et al*., 2012). In particular, an interesting analysis of the interaction of waves with an array of oscillating wave surge converters (OWSCs) and the performance of such systems was performed by Sarkar *et al*. (2014).

According to Sarkar *et al*. (2014), to evaluate the interaction effects of an array configuration of multiple WECs on the extracted power, the interaction factor (q-factor) can be used. The wave farm configuration that gave them the best performance is with the devices alternated in two rows. Even though the same methodology has been used, for this case study the configuration with the WECs aligned along a single line resulted to have the highest q-factor, therefore is the best one in terms of performance. However, to have a larger number of devices in a confined area nearshore, a more compact configuration was chosen with the devices alternated in more rows. With the same methodology, the optimal spacing between two devices in the same row was found to be 50 m while between two devices in different rows was 20 m. To save computational time, both spacings have been tested only at 10, 20 and 50 m. However, a better method to define the optimal spacing, both between devices and between lines, would have been to define a tendency simulating more than just three spacing values, for instance: 10, 15, 20, 30, 40, 50 m.

With the alternated configuration, the wave propagation in the presence of a wave farm from 10 to 100 WECs was studied under the six study cases and waves coming from 315°. In Costa *et al*., (2001) it is verified that the three main wave directions in Figueira da Foz and Sines are: North (360°), Northwest (315°) and West (360°). Thus, since Peniche is located between those two sites, these three main directions were tested in the simulations. The direction of 315° was chosen since from the wave climate analysis it showed to be the most common wave direction in that area (about 60% of the waves from 200 to 2018 had a direction between 292.5° and 337.5°) and, from the simulations, a wave farm placed perpendicular to that direction gives the highest *q*-factor. This result is also in good agreement with a previous theoretical study by Tay & Venugopal (2016).

The wave farm impact on significant wave height, mean period and direction was evaluated in terms of percentage change from baseline, where baseline is the model results in the absence of WECs. In particular, the results illustrate that the significant wave heights decreased of up to 60% between baseline and modelled conditions for 10 WECs and up to 80% for 100 WECs. The maximum changes in significant wave height were observed downstream of the WEC array near the array centreline, where the largest wave shadowing effects are predicted given that the modelled incident wave direction is from North-West. Right in the lee of the WECs array the difference in significant wave height for an array of 100 devices reached more than 3 m. However, when analysing the impact of the farm on the nearshore area between 0 m and 5 m depth the average H_s change for a farm of 10 WECs was 0.01 m, with a maximum of 0.23 m and for a farm of 100 WECs was 0.03 m, with a maximum of 0.27 m. Therefore, it seems that when increasing the number of devices is mostly the area close to the farm to be affected in terms of percentage change of significant wave height, while closer to the coast the change ranges of few centimetres.

However, even though a change in significant wave height was found, at the present a generic threshold for “significant” WEC induced impacts does not exist and, anyway, it would be site-specific. Moreover, as stated by Stokes & Conley (2018), the impact of a WEC farm on surfing waves will depend on the wave preferences of local water-users as waves previously larger than the preferred range may be reduced to a surfable range. This can also be investigated as an interesting way of beach protection. The concept of using WECs also as a coastal defence is a win-win alternative because they can be used both as renewable energy source and for coastal protection (Mendoza et al., 2014).

Chang *et al*. (2016) simulated with SNL-SWAN in Santa Cruz a wave farm of 50 bottom-fixed oscillating flaps with 6 m spacing and 26 m diameter. For input waves of H_s=1.7 m, T_p=12.5 s and Dir_m=205 ° the significant wave height percentage change they obtained with OBCASE 1 ranges between 0-35% in the lee of the wave farm. The resulting percentage change in H_s for case study B (H_s=2 m, T_p=12 s and Dir_m=315 °) ranged between 0-70%, the double of that obtained by Chang *et al*. (2016). However, it is not possible to compare those results since even though the same power matrix and same device type have been used, the spacing between devices for the present study was 50 m and the depth of the wave farm ranged between 10 – 17 m.

The changes in peak period were negligible, as already assessed by Chang *et al*. (2016), due to the fact that with OBCASE 1 the obstacles absorb the same percentage of wave energy from all wave frequencies (i.e. because the transmission coefficient is frequency-independent), therefore there is no change in peak wave energy. The mean period resulted instead to increase in the lee of the wave farm and to decrease nearshore. However, the decrease was always lower than 0.6 s in the nearshore area between 0 m and 5 m depth for all the wave farms and case studies simulated, while in the lee of the devices the maximum increase in mean period was obtained for 100 WECs and case study A and resulted to be 2.79 s.

The changes in wave direction were negative on the top right corner of the wave farm, meaning that the waves are rotating clockwise, and positive on the bottom left corner, so the waves are rotating counter-clockwise around the wave farm. All percentage differences between the baseline scenario and all simulated WEC array are within ±4%, corresponding to ±10° change in mean wave direction, comparable with the results obtained by Chang *et al.* (2016): ±4.5% percentage difference corresponding to ±10° in mean wave direction. Zero wave direction change was observed in the central part of the lee of the array.

This study, along with previous studies (Abanades *et al*., 2015; Black, 2007; Dea & Haller, 2014; Li, 2010; Millar et al., 2007), demonstrated that the near-field and far-field attenuation of wave heights increases with increasing energy absorption (decreasing K_t) and decreases with increasing distance from the WEC array. What was also be observed is that when the number of WECs increases, the footprint area increases and the wave height in the lee of the wave farm decreases.

Moreover, to simulate the behaviour of a wave farm in real sea state conditions, 50 WaveRoller type of WECs have been studied under 19 years (from 2000 to 2019) of wave climate. The large hypothetical WEC array investigated did show significant alterations to the wave properties. It was observed a stronger variability in significant wave height on a monthly base rather than on an annual base. Locations in the lee centreline of the array showed the largest potential changes in wave height compared to those at the eastern and western fringes of the shadow zone.

As already demonstrated by Jones *et al.* (2014), WEC devices can also change the patterns of the sediments dynamics and the circulation and those changes in wave direction were identified but should be further investigated to assess whether they affect the circulation and sediment transport in the adjacent area. Where the waves are altered by the presence of a WEC farm knock-on effects to coastal sedimentation and beach morphology may occur (e.g., Abanades *et al*., 2015; Dea & Haller, 2014; Gonzalez-Santamaria *et al*., 2013; Li, 2010).

A limit of the study has to be mentioned, that might be overcome in future studies: to save computational time the baseline scenarios were not simulated for these 19 years and a quantification of the percentage change in significant wave height is therefore missing.

The results from the present study could be used to guide the selection of conditions with which to run full ocean circulation models that consider waves, currents, and winds. The ocean circulation model, coupled with sediment transport simulations, can indicate potential coastal geomorphological variability due to the presence of WEC arrays. In particular, to assess the effects of WECs not only on the hydrodynamics but on local sediment transport, the SNL-SWAN wave model could be coupled with the sediment transport model SNL-EFDC (Thanh *et al.*, 2008).

In the last step of this study, a WaveRoller farm was compared to a Bombora's mWave farm (Bombora Wavepower, 2016), which is a submerged pressure differential device. The WaveRoller device type resulted in greater reductions in wave heights in the lee of the WEC array due to its potential for capturing more power than the Bombora's mWave device type. This is due to the fact that the power matrix of the WaveRoller type of WEC has larger values than the Bombora's mWave power matrix, therefore the transmission coefficients are lower and more energy is absorbed from the incoming waves. However, the effect of Bombora's mWave farm extended over approximately the same spatial extent due to its size and spacing, thereby potentially having a similar impact on the shoreline than the WaveRoller. Again, both OBCASE 1 and 2 have been tested and compared to verify if with a different device, therefore a different power matrix, the results would change. It was found that for both devices with OBCASE 1 the wave height decrease in the lee of the wave farm is higher than with OBCASE 2, contrarily to what was found in previous studies (Ruehl *et al*., 2015; Chang *et al.*, 2016). Further investigations should be therefore performed to determine the reasons for this substantial difference. For the WaveRoller type of WECs the optimal wave farm configuration (which means higher q-factors) resulted to be with an angle of inclination $\alpha = 0°$, which means perpendicular to the incoming waves.

Previous model sensitivity studies revealed that the magnitude of wave height reduction is directly correlated to a WEC's power matrix values thus to the power absorbed, with larger values resulting in more reduction in wave height and vice versa (Chang *et al.*, 2014a). The main outcome from the comparison between the two kinds of device is that the power matrix is of fundamental importance when simulating the impact of an array of WECs on the wave propagation and transformation. The resulting percentage change in wave height is extremely sensitive to the input values of power absorbed.

6 | Conclusions

The presence of wave energy converters (WECs) farms can significantly alter wave propagation patterns and affect coastal circulation patterns, sediment transport patterns, and therefore alter ecosystem processes. Wave model simulations provide the means to investigate WEC effects on the nearshore physical environment and calculate the power produced from an array of WECs, over a range of anticipated wave conditions.

The present study aimed to examine potential WEC array deployment scenarios at Almagreira beach at the Portuguese coast and investigate the wave modifications caused by those WECs downstream of the wave farm, at nearshore locations. For this purpose a modified version of a standard wave modelling tool, named SNL-SWAN (Sandia National Laboratories - Simulating WAves Nearshore), was utilized. Note that the SNL-SWAN model can evaluate WEC farm effects on wave propagation by incorporating a WEC module in which the user can parameterize a device using a power matrix or relative capture width curve.

The WEC chosen is similar to the WaveRoller oscillating wave surge converter of 25 m, already tested in Praia de Almagreira north of Peniche since 2007. SNL-SWAN was first validated against the in-situ data from the “Nazaré Costeira” buoy and good agreement was found between the modelled and observed data. Then the wave climate in the study area was characterized and six most common and energetic sea states were chosen: from case A, with H_s = 2 m and T_p = 10 s to case F, with H_s = 3 m and T_p = 16 s. The North-West (315°) was decided as the most common wave direction to be used in the simulations and the arrays of WaveRoller type devices were placed perpendicular to this incoming direction.

SNL-SWAN includes a frequency-dependent WEC module that, based on the WEC’s power performance, calculates the transmission coefficients. The SNL-SWAN five obstacle cases (OBCASEs) have been evaluated: as expected OBCASE 0 resulted equal to the native SWAN model; OBCASE 3 and 4 were not working in the SNL-SWAN version used for the present work; OBCASE 1 gave higher percentage decreases in significant wave height and more power absorption than OBCASE 2 and was therefore chosen for precautionary reasons as it represents the worst-case scenario in terms of changes in significant wave height. As an indirect advancement and result of this study the bug into the code of the SNL-SWAN model has been fixed by the Sandia National Laboratories team.

The WEC spacing, general placement and absorption are important factors to consider when evaluating the effects of WEC arrays on nearshore processes. In this study was demonstrated that the overall performance of an array is largely influenced by the positions of each WEC. The general framework developed here can be used to design more efficient arrays while minimizing impacts on nearshore environments.

In this particular case, the model was run with an array of 10 to 100 WECs at a depth between 10 m and 17 m and the optimal spacing between two devices in the same row was found to be 50 m while between two devices in different rows was 20 m. The wave farm configuration that gave the best performance was with the devices aligned in one row. However, the configuration with WEC alternated in two or more rows was chosen to model a farm with 10 to 100 devices to limit the deployment area.

The results from the simulations were compared with model runs without WECs (baseline scenario) and generally the changes in significant wave height were the primary alteration resulting in the presence of a WECs array and larger numbers of WEC devices within an array absorb a larger amount of wave energy, resulting in a larger wave shadow in lee of the array (both in horizontal extent and in magnitude of wave decrease). Maximum changes in Hs were found for locations downstream of the WEC array, along the angles of incident wave direction. When analysing the impact of the farm on the nearshore area between 0 m and 5 m depth the average H_s change for a farm of 10 WECs was 0.01 m, with a maximum of 0.23 m and for a farm of 100 WECs was 0.03 m, with a maximum of 0.27 m.

From the simulations of real sea states for the period from 2000 to 2018, it was possible to observe that locations in the lee centreline of the array have largest potential changes in wave height compared to those at the eastern and western fringes of the shadow zone. Moreover, WEC devices can change the patterns of the sediment's dynamics and circulation. This work showed that a wave farm could alter the behaviour of Almagreira beach in its lee but this could not be a negative aspect: the wave farm could lead to beach accretion and thus serve to counter erosional trends. But the effects of wave energy extraction on beach morphology and water users could be better investigated through a validation of the model results with in-situ data but, at the moment, there is no available access to the prototype testing data.

Moreover, it was found that the decrease of significant wave height also depends on the WEC device type. A comparison was performed between a wave farm of 40 WaveRoller type of WECs and 40 Bombora's mWave type of WECs and the result is strictly related to the power matrix: the device with higher power absorption potential showed a greater decrease in significant wave height in the lee of the wave farm. Therefore, extreme attention must be played in getting the correct values from the specific company that is planning on deploying a certain device or from ongoing laboratory studies and field tests. What can be concluded is that, given a reliable power matrix or relative capture width curve and the length of the device, SNL-SWAN could be a good instrument to compare different kind of WEC devices.

With the present work, the potentiality of SNL-SWAN OBCASEs 1 and 2 model has been investigated and as a future work would be interesting to perform all the analysis with and without the WECs farm with SNL-SWAN OBCASEs 3 and 4 to compare them with OBCASEs 1 and 2. Future work might also include modelling of the WaveRoller type or other types of devices under extreme wave conditions and a coupling of that with a sediment transport model.

7 | References

Abanades, J., Greaves, D., & Iglesias, G. (2015). Wave farm impact on beach modal state. *Marine Geology*, *361*, 126–135. https://doi.org/10.1016/j.margeo.2015.01.008

Aderinto, T., & Li, H. (2018). Ocean Wave energy converters: Status and challenges. *Energies*, *11*(5), 1–26. https://doi.org/10.3390/en11051250

Akar, S., & Akdoğan, D. A. (2018). Environmental and Economic Impacts of Wave Energy: Some Public Policy Recommendations for Implementation in Turkey. *Sustainable Development: Concepts, Methodologies, Tools, and Applications*, (January 2016), 1187–1211. https://doi.org/10.4018/978-1-5225-0440-5.ch013

Algie, C., Ryan, S., & Fleming, A. (2017). Predicted power performance of a submerged membrane pressure-differential wave energy converter. *International Journal of Marine Energy*, *20*, 125–134. https://doi.org/10.1016/j.ijome.2017.09.005

Arinaga, R. A., & Cheung, K. F. (2012). Atlas of global wave energy from 10 years of reanalysis and hindcast data. *Renewable Energy*, *39*(1), 49–64. https://doi.org/10.1016/j.renene.2011.06.039

Babarit, A. (2010). Impact of long separating distances on the energy production of two interacting wave energy converters. *Ocean Engineering*, *37*, 718–729. https://doi.org/10.1016/j.oceaneng.2010.02.002

Babarit, A. (2015). A database of capture width ratio of wave energy converters. *Renewable Energy*, *80*, 610–628. https://doi.org/10.1016/j.renene.2015.02.049

Babarit, A., Hals, J., Muliawan, M. J., Kurniawan, A., Moan, T., & Krokstad, J. (2012). Numerical benchmarking study of a selection of wave energy converters. *Renewable Energy*, *41*, 44–63. https://doi.org/10.1016/j.renene.2011.10.002

Barstow, S., Mørk, G., Lønseth, L., & Mathisen, J. P. (2009). WorldWaves wave energy resource assessments from the deep ocean to the coast. In *8th European Wave and Tidal Energy Conference, Uppsala, Sweden* (pp. 149–159).

Battjes, J. A. (1994). Shallow water wave modelling. In M. Isaacson & M. Quick (Eds.), *Waves - Physical and Numerical Modelling* (pp. 1–23). Univ. of British Columbia, Vancouver.

Battjes, J. A., & Janssen, J. P. F. M. (1978). Energy loss and set-up due to breaking of random waves. *Coastal Engineering 1978*, 569–587.

Bento, A. R., Rusu, E., Martinho, P., & Soares, C. G. (2014). Assessment of the changes induced by a wave energy farm in the nearshore wave conditions. *Computers and Geosciences*. https://doi.org/10.1016/j.cageo.2014.03.006

Bergillos, R. J., López-Ruiz, A., Medina-López, E., Moñino, A., & Ortega-Sánchez, M. (2018). The role of wave energy converter farms on coastal protection in eroding deltas, Guadalfeo, southern Spain. *Journal of Cleaner Production*, *171*(2018), 356–367. https://doi.org/10.1016/j.jclepro.2017.10.018

Besio, G., Mentaschi, L., & Mazzino, A. (2016). Wave energy resource assessment in the Mediterranean Sea on the basis of a 35-year hindcast. *Energy*, *94*, 50–63. https://doi.org/10.1016/j.energy.2015.10.044

Black, K. (2007). *Review of Wave Hub Technical Studies: Impacts on inshore surfing beaches*. Retrieved from https://tethys.pnnl.gov/sites/default/files/publications/Impacts_on_Inshore_Surfing_Beaches.pdf

Bombora Wavepower. (2016). *Bombora prepares for Portugal Wave Farm after Strong LCOE Results*. Retrieved from bomborawavepower.com.au

Booij, N., R. R. and L. H. (1999). A third-generation wave model for coastal regions: 1. Model description and validation. *Journal of Geophysical Research*, *104*(C4), 7649–7666.

Borgarino, B., Babarit, A., & Ferrant, P. (2012). Impact of wave interactions effects on energy absorption in large arrays of wave energy converters. *Ocean Engineering*, *41*, 79–88. https://doi.org/10.1016/j.oceaneng.2011.12.025

Borthwick, A. G. L. (2016). Marine Renewable Energy Seascape. *Engineering*, *2*(1), 69–78. https://doi.org/10.1016/J.ENG.2016.01.011

Bosnic, I., Duarte, J., Taborda, R., Cascalho, J., Silva, A., & Oliveira, A. (2014). Modelling nearshore dynamics at Norte beach (Nazaré). In *Actas das 3as Jornadas de Engenharia Hidrográfica* (pp. 229–232). Lisboa, Portugal.

Brito e Melo, A., & Villate, J. L. (2016). *Ocean Energy Systems: Annual Report 2016*.

Budal, K., & Falnes, J. (1974). Proposals for conversion of the energy in ocean waves. Trondheim, Norway.

Budar, K., & Falnes, J. (1975). A resonant point absorber of ocean-wave power. *Nature*, *256*(5517), 478-479.

Caetano, E., & Innocentini, V. (2003). An improved second generation wave model. *Brazilian Journal of Oceanography*, *51*(unico), 1–21. https://doi.org/10.1590/S1679-87592003000100002

Castro-Santos, L., Silva, D., Bento, A. R., Salvação, N., & Soares, C. G. (2018). Economic Feasibility of Wave Energy Farms in Portugal. *Energies*, *11*(3149), 1–16. https://doi.org/10.3390/en11113149

Cavaleri, L., Alves, J. H. G. M., Ardhuin, F., Babanin, A., Banner, M., Belibassakis, K., … Young, I. (2007). Wave modelling - The state of the art. *Progress in Oceanography*, *75*(4), 603–674. https://doi.org/10.1016/j.pocean.2007.05.005

Chang, G., Magalen, J., Jones, C., & Roberts, J. (n.d.). Investigation of Wave Energy Converter Effects on the Nearshore Environment : A Month-Long Study in Monterey Bay , CA.

Chang, G., Magalen, J., Jones, C., & Roberts, J. (2014a). *Investigation of Wave Energy Converter Effects on the Nearshore Environment: A Month-Long Study in Monterey Bay, CA*. Retrieved from http://www.ntis.gov/help/ordermethods.asp?loc=7-4-0#online

Chang, G., Magalen, J., Jones, C., & Roberts, J. (2014b). *Wave Energy Converter Effects on Wave Fields: Evaluation of SNL-SWAN and Sensitivity Studies in Monterey Bay, CA.*

Chang, G., Ruehl, K., Jones, C. A., Roberts, J., & Chartrand, C. (2016). Numerical modeling of the effects of wave energy converter characteristics on nearshore wave conditions. *Renewable Energy*, *89*, 636–648. https://doi.org/10.1016/j.renene.2015.12.048

Chen, Z., Yu, H., Hu, M., Meng, G., & Wen, C. (2013). A review of offshore wave energy extraction system. *Advances in Mechanical Engineering*, *2013*. https://doi.org/10.1155/2013/623020

Child, B. F. M., & Venugopal, V. (2010). Optimal configurations of wave energy device arrays. *Ocean Engineering*, *37*(16), 1402–1417. https://doi.org/10.1016/j.oceaneng.2010.06.010

Clément, A., Mccullen, P., Fiorentino, A., Gardner, F., Hammarlund, K., Lemonis, G., … Thorpe, T. (2002). Wave energy in Europe current status and perspectives. *Renewable and Sustainable Energy Reviews*, *6*, 405–431.

Contardo, S., Hoeke, R., Hemer, M., Symonds, G., McInnes, K., & O'Grady, J. (2018). In situ observations and simulations of coastal wave field transformation by wave energy converters. *Coastal Engineering*, *140*(August 2017), 175–188. https://doi.org/10.1016/j.coastaleng.2018.07.008

Cornett, A. M. (2008). A global wave energy resource assessment. *Proceedings of the Eighteenth International Offshore and Polar Conference*, *1*(January), 1–9. https://doi.org/10.1016/j.jsg.2003.08.002

Cornett, A. M. (2014). A Global Wave Energy Resource Assessment, (July 2008).

Costa, M., & Esteves, R. (2010). Clima de agitação marítima na costa oeste de Portugal Continental. In *Proceedings of XI Jornadas Técnicas de Engenharia Naval-O Sector Marítimo Português.* (pp. 413–426). Lisboa, Portugal.

Costa, M., Silva, R., & Vitorino, J. (2001). Contribuição Para O Estudo Do Clima De Agitação

Marítima Na Costa Portuguesa. *Conference: 2^{a}s Jornadas Portuguesas de Engenharia Costeira e Portuária, AIPCN/PIANC*, 20.

Cruz, E., Simas, T., & Kasanen, E. (2015). Discussion of the effects of the underwater noise radiated by a wave energy device - Portugal. In *Proceedings of the 11th European Wave and Tidal Energy Conference* (p. 5).

Cruz, J. (2007). *Ocean Wave Energy: Current Status and Future Prepectives*. *Springer Science & Business Media*. https://doi.org/10.2174/97816080528511060101

Cruz, J., Sykes, R., Siddorn, P., & Taylor, R. E. (2009). Wave Farm Design: Preliminary Studies on the Influences of Wave Climate, Array Layout and Farm Control. In *Proceedings of the 8th European Wave and Tidal Energy Conference* (pp. 736–745). Uppsala, Sweden.

Dalton, G. J. (2009). *Non-technical barriers to wave energy in Europe. Input to the Waveplam Project*. Retrieved from https://www.ucc.ie/en/media/research/hmrc/publications/Nontechnicalbarrierstowaveenergy.pdf

De Chowdhury, S., Nader, J.-R., Sanchez, A. M., Fleming, A., Winship, B., Illesinghe, S., … Manasseh, R. (2015). A review of hydrodynamic investigations into arrays of ocean wave energy converters. *Fluid Dynamics*. Retrieved from http://arxiv.org/abs/1508.00866

de Melo Veloso, R. C., & Castro, R. M. G. (2014). *Technical Assessment of Wave Energy in Portugal*. *Department of Electrical and Computer Engineering, Instituto Superior Técnico, Lisbon-Portugal*.

de Sousa Prado, M. G., Gardner, F., Damen, M., & Polinder, H. (2006). Modelling and test results of the Archimedes wave swing. *Proceedings of the Institution of Mechanical Engineers, Part A: Journal of Power and Energy*, *220*(8), 855–868. https://doi.org/10.1243/09576509JPE284

Dea, A. M. O., & Haller, M. C. (2014). Analysis of the impacts of wave energy converter arrays on the nearshore wave climate. In *Proceedings of the 2nd Marine Energy Technology Symposium* (pp. 1–9). Seattle, WA.

Dodet, G., Bertin, X., & Taborda, R. (2010). Wave climate variability in the North-East Atlantic Ocean over the last six decades. *Ocean Modelling*, *31*(3–4), 120–131.

Drew, B., Plummer, A. R., & Sahinkaya, M. N. (2009). A review of wave energy converter technology. *Proceedings of the Institution of Mechanical Engineers, Part A: Journal of Power and Energy*, *223*(8), 887–902. https://doi.org/10.1243/09576509JPE782

Eldeberky, Y. (1996). *Nonlinear transformation of wave spectra in the nearshore zone*. *Ph.D. thesis*.

European Commission. (2012). Energy Roadmap 2050. *Policy*, 1–24. https://doi.org/10.2833/10759

Falcão, A. F. d. O. (2010). Wave energy utilization: A review of the technologies. *Renewable and Sustainable Energy Reviews*, *14*(3), 899–918. https://doi.org/10.1016/j.rser.2009.11.003

Falcão, Antonio. (2000). The shoreline OWC wave power plant at the Azores. *Proceedings of the Fourth European Wave Energy Conference*, (December), 42–48.

Falcão, Antonio. (2014). Modelling of Wave Energy Conversion. *Renewable Energy*, 1–38. https://doi.org/10.1002/ffj.2730070416

Falcão, António. (2010). Wave energy utilization: A review of the technologies. *Renewable and Sustainable Energy Reviews*, *14*(3), 899–918. https://doi.org/10.1016/j.rser.2009.11.003

Falnes, J. (2007). A review of wave-energy extraction. *Marine Structures*, *20*(7), 185–201. https://doi.org/10.1016/j.marstruc.2007.09.001

Folley, M., Elsaesser, B., & Whittaker, T. (2010). Analysis of the wave energy resource at the European Marine Energy Centre. In T. T. Ltd. (Ed.), *Proceedings of the 9th international conference organised by the Institution of Civil Engineers* (pp. 1–660). Edinburgh on 16 to 18 September 2009.

Folley, M., & Whittaker, T. J. T. (2009). Analysis of the nearshore wave energy resource. *Renewable Energy*, *34*(7), 1709–1715. https://doi.org/10.1016/j.renene.2009.01.003

Gleizon, P., Campuzano, F., Pablo, C., Martinez, A., Goggins, J., Atan, R., & Nash, S. (2017).

Wave Energy Resources Along the European Atlantic Coast. *Marine Renewable Energy*, 1–387. https://doi.org/10.1007/978-3-319-53536-4

Gonzalez-Santamaria, R., Zou, Q.-P., & Pan, S. (2011). The impact of a wave farm on large scale sediment transport. *Ewtec 2011*, 2–7.

Gonzalez-Santamaria, R., Zou, Q. P., & Pan, S. (2013). Impacts of a Wave Farm on Waves, Currents and Coastal Morphology in South West England. *Estuaries and Coasts*, *38*(1), 159–172. https://doi.org/10.1007/s12237-013-9634-z

Group, W. (1988). The WAM Model - A third Generation Ocean Wave Prediction Model. *Journal of Physical Oceanography*, *18*(12), 1775–1810.

Hasselmann, K. (1968). *Weak-Interaction Theory of Ocean Waves*. *Basic Developments in Fluid Dynamics*. Elsevier Ltd. https://doi.org/10.1016/B978-0-12-395520-3.50008-6

Hasselmann, K., Barnett, T. P., Bouws, E., Carlson, H., Cartwright, D. E., Enke, K., … Walden, H. (1973). Measurements of Wind-Wave Growth and Swell Decay during the Joint North Sea Wave Project (JONSWAP). *Erganzungsheft Zur Deutschen Hydrographischen Zeitschrift*, *12*(8).

Hasselmann, K., Sell, W., Ross, D. B., & Müller, P. (1976). A Parametric Wave Prediction Model. *Journal of Physical Oceanography*. https://doi.org/10.1175/1520-0485(1976)006<0200:APWPM>2.0.CO;2

Hasselmann, S., & Hasselmann, K. (1985). Computations and Parametrizations of the Nonlinear EnergyTransfer in a Gravity-Wave Spectrum. Part I: A New Method for Efficient Computations of the Exact Nonlinear Transfer Integral. *Journal of Physical Oceanography*. https://doi.org/10.1021/jo01155a013

Hasselmann, S., Hasselmann, K., Allender, J. H., & Barnett, T. P. (1985). Computations and Parameterizations of the Nonlinear Energy Transfer in a Gravity-Wave Specturm. Part II: Parameterizations of the Nonlinear Energy Transfer for Application in Wave Models. *Journal of Physical Oceanography*, *15*(11), 1378–1392. https://doi.org/10.1175/1520-0485(1985)015<1378:CAPOTN>2.0.CO;2

Heath, T. V. (2000). The Development and Installation of the Limpet Wave Energy Converter. *World Renewable Energy Congress VI*, 1619–1622. https://doi.org/10.1016/B978-008043865-8/50334-2

Heller, V., Chaplin, J. R., Farley, F., & Hann, M. (2010). Physical model tests of the anaconda wave energy converter. In *1st IAHR European Congress*. Edinburgh.

Henderson, R. (2006). Design, simulation, and testing of a novel hydraulic power take-off system for the Pelamis wave energy converter. *Renewable Energy*, *31*(2), 271–283. https://doi.org/10.1016/j.renene.2005.08.021

Henry, A., Doherty, K., Cameron, L., Whittaker, T., & Doherty, R. (2010). Advances in the Design of the Oyster Wave Energy Converter. In *Marine Renewables and Offshore Wind Conference, Royal Institute of Naval Architects*. London.

Holthuijsen, L. H., Herman, A., & Booij, N. (2003). Phase-decoupled refraction-diffraction for spectral wave models. *Coastal Engineering*, *49*(4), 291–305. https://doi.org/10.1016/S0378-3839(03)00065-6

Hussain, A., Arif, S. M., & Aslam, M. (2017). Emerging renewable and sustainable energy technologies: State of the art. *Renewable and Sustainable Energy Reviews*, *71*(January), 12–28. https://doi.org/10.1016/j.rser.2016.12.033

IEA. (2018). *Market Report Series: Renewables 2018*. https://doi.org/10.1787/coal_mar-2017-en

Iglesias, G., & Carballo, R. (2014). Wave farm impact: The role of farm-to-coast distance. *Renewable Energy*, *69*. https://doi.org/10.1016/j.renene.2014.03.059

INE, I. P. (2018). *Anuário Estatístico da Região Centro 2017*. Lisboa, Portugal.

International Energy Agency. (2017). *World Energy Outlook 2017. Together Secure Sustainable* (Vol. Executive). https://doi.org/10.1016/0301-4215(73)90024-4

Jones, C., Magalen, J., & Roberts, J. (2014). *Wave Energy Converter (WEC) Array Effects on*

Wave, Current, and Sediment Circulation: Monterey Bay , CA. Albuquerque, New Mexico 87185 and Livermore, California 94550.

Kofoed, J. P., Frigaard, P., Friis-Madsen, E., & Sørensen, H. C. (2006). Prototype testing of the wave energy converter wave dragon. *Renewable Energy*, *31*(2), 181–189. https://doi.org/10.1016/j.renene.2005.09.005

Komen, G. J., Hasselmann, K., & Hasselmann, K. (1984). On the existence of a fully developed wind-sea spectrum. *Journal of Physical Oceanography*, *14*(8), 1271–1285.

Kulia, P. B. G. G., Ringwood, J. V, & Molinas, M. (2017). Real-Time Passive Control of Passive Control of Wave Energy Converters Using the Hilbert-Huang Transform. *IFAC-PapersOnLine*, *50*(1), 14705–14710. https://doi.org/10.1016/j.ifacol.2017.08.2502

Langhamer, O., Wilhelmsson, D., & Engstro, J. (2009). Artificial reef effect and fouling impacts on offshore wave power foundations and buoys – a pilot study. *Estuarine, Coastal and Shelf Science*, *82*, 426–432. https://doi.org/10.1016/j.ecss.2009.02.009

Li, B. (2010). South West wave energy hub: coastal impact and wave energy, (February), 17–29. https://doi.org/10.1680/ener.2010.163.1.17

Lisboa, R. C., Teixeira, P. R. F., & Fortes, C. J. (2017). Numerical evaluation of wave energy potential in the south of Brazil. *Energy*, *121*, 176–184. https://doi.org/10.1016/j.energy.2017.01.001

López, I., Andreu, J., Ceballos, S., Alegría, I. M. De, & Kortabarria, I. (2013). Review of wave energy technologies and the necessary power-equipment. *Renewable and Sustainable Energy Reviews*, *27*, 413–434. https://doi.org/10.1016/j.rser.2013.07.009

López, I., Andreu, J., Ceballos, S., Martínez De Alegría, I., & Kortabarria, I. (2013). Review of wave energy technologies and the necessary power-equipment. *Renewable and Sustainable Energy Reviews*, *27*, 413–434. https://doi.org/10.1016/j.rser.2013.07.009

Luczko, E., Bailey, H., Robertson, B., Hiles, C., & Buckham, B. (2016). Assimilating a time-domain representation of a wave energy converter into a spectral wave model. In *ASME 2016 35th International Conference on Ocean, Offshore and Arctic Engineering. American Society of Mechanical Engineers.*

Madsen, O. S., Poon, Y. K., & Graber, H. C. (1989). Spectral wave attenuation by bottom friction: Theory. *Coastal Engineering 1988*, 492–504.

Magagna, D., & Uihlein, A. (2015). Ocean energy development in Europe: Current status and future perspectives. *International Journal of Marine Energy*, *11*, 84–104. https://doi.org/10.1016/j.ijome.2015.05.001

Marquis, L., Kramer, M. M., Kringelum, J., Chozas, J. F., & Helstrup, N. E. (2012). Introduction of Wavestar Wave Energy Converters at the Danish offshore wind power plant Horns Rev 2. *4th International Conference on Ocean Energy*, *2*(December), 2–7. https://doi.org/Doi 10.1080/15216540500305910

McCormick, M. E. (1981). *Ocean wave energy conversion.* (1st ed.). New York: Wiley-Interscience.

Melikoglu, M. (2018). Current status and future of ocean energy sources: A global review. *Ocean Engineering*, *148*(June 2017), 563–573. https://doi.org/10.1016/j.oceaneng.2017.11.045

Mendoza, E., Silva, R., Zanuttigh, B., Angelelli, E., Lykke, T., Martinelli, L., … Ruol, P. (2014). Beach response to wave energy converter farms acting as coastal defence. *Coastal Engineering*, *87*, 97–111. https://doi.org/10.1016/j.coastaleng.2013.10.018

Millar, D. L., Smith, H. C. M., & Reeve, D. E. (2007). Modelling analysis of the sensitivity of shoreline change to a wave farm. *Ocean Engineering*, *34*(5–6), 884–901. https://doi.org/10.1016/j.oceaneng.2005.12.014

Ministério do Mar, Ministério da Ciência Tecnologia e Ensino Superior, Ministério da Economia, Ministério do Ambiente, Defesa, M. da, WavEC, … Galp Energia. (2016). *Energia No Mar: Roteiro para uma Estratégia Industrial das Energias Renováveis Oceânicas.* Lisboa.

Monteiro, N. (2017). *Efeito da Extração da Energia das Ondas na Propagação da Agitação na*

Costa Portuguesa. Universidade do Porto.

Munk, W. H., & Traylor, M. A. (1947). Refraction of ocean waves: a process linking underwater topography to beach erosion. *The Journal of Geology*, *55*(1), 1–26.

Nader, J., Zhu, S., Cooper, P., & Stappenbelt, B. (2012). A finite-element study of the efficiency of arrays of oscillating water column wave energy converters. *Ocean Engineering*, *43*, 72–81. https://doi.org/10.1016/j.oceaneng.2012.01.022

Nunes, R., Silveira, L., & Brito, M. (2018). The Impacts of Rip Curl Pro, Surf Competition, in Peniche (Portugal), *44*(26), 129–141.

OES. (2014). *Annual Report: Implementing and Agreement on Ocean Energy Systems*. *Annual Report 2014*. https://doi.org/10.1017/S0001972000001765

OES. (2017). *Annual Report: an overview of ocean energy activities in 2017*. Retrieved from https://report2017.ocean-energy-systems.org/index.php

Oskamp, J. A., & Özkan-haller, H. T. (2012). Power calculations for a passively tuned point absorber wave energy converter on the Oregon coast. *Renewable Energy*, *45*, 72–77. https://doi.org/10.1016/j.renene.2012.02.004

Palha, A., Mendes, L., Fortes, C. J., Brito-Melo, A., & Sarmento, A. (2010). The impact of wave energy farms in the shoreline wave climate: Portuguese pilot zone case study using Pelamis energy wave devices. *Renewable Energy*, *35*(1), 62–77. https://doi.org/10.1016/j.renene.2009.05.025

Pearson, P. J. G., & Foxon, T. J. (2012). A low carbon industrial revolution? Insights and challenges from past technological and economic transformations. *Energy Policy*, *50*, 117–127. https://doi.org/10.1016/j.enpol.2012.07.061

Phillips, O. M. (1958). The equilibrium range in the spectrum of wind-generated waves. *Transactions American Geophysical Union*, *33*(6), 834–844.

Pierson, W. J., & Marks, W. (1952). The power spectrum analysis of ocean-wave records. *Eos, Transactions American Geophysical Union*, *33*(6), 834–844. https://doi.org/10.1029/TR033i006p00834

Pontes, M. T., Aguiar, R., & Oliveira Pires, H. (2005). A Nearshore Wave Energy Atlas for Portugal. *Journal of Offshore Mechanics and Arctic Engineering*, *127*(3), 249. https://doi.org/10.1115/1.1951779

Quadrelli, R., & Peterson, S. (2007). The energy-climate challenge: Recent trends in CO2 emissions from fuel combustion. *Energy Policy*, *35*, 5938–5952. https://doi.org/10.1016/j.enpol.2007.07.001

Reguero, B. G., Vidal, C., Menéndez, M., Méndez, F. J., Minguez, R., & Losada, I. (2011). Evaluation of global wave energy resource. In *OCEANS 2011 IEEE - Spain*. https://doi.org/10.1109/Oceans-Spain.2011.6003523

Reikard, G., Robertson, B., & Bidlot, J. R. (2017). Wave energy worldwide: Simulating wave farms, forecasting, and calculating reserves. *International Journal of Marine Energy*, *17*, 156–185. https://doi.org/10.1016/j.ijome.2017.01.004

Renzi, E., Abdolali, A., Bellotti, G., & Dias, F. (2014). Wave-power absorption from a finite array of oscillating wave surge converters. *Renewable Energy*, *63*, 55–68. https://doi.org/10.1016/j.renene.2013.08.046

Renzi, E., & Dias, F. (2012). Relations for a periodic array of flap-type wave energy converters. *Applied Ocean Research*, *39*, 31–39. https://doi.org/10.1016/j.apor.2012.09.002

Rocha, A. A. S. (2016). *Underwater noise propagation models and its application in renewable energy parks: WaveRoller Case Study*. Universidade Nova de Lisboa.

Ruehl, K. M., Chartrand, C., & Porter, A. (2014). SNL-SWAN User' s Manual, 0–12. Retrieved from http://prod.sandia.gov/techlib/access-control.cgi/2014/1420185r.pdf

Ruehl, K., Porter, A., Chartrand, C., Smith, H. C. M., Chang, G., & Roberts, J. (2015). Development, Verification and Application of the SNL-SWAN Open Source Wave Farm Code. *Proceedings of the 11th European Wave and Tidal Energy Conference*, 1–8.

Ruehl, K., Porter, A., Posner, A., & Roberts, J. (2013). Development of SNL-SWAN , a Validated Wave Energy Converter Array Modeling Tool. *EWTEC 2013 Proceedings*.

Ruol, P., Zanuttigh, B., Martinelli, L., Kofoed, P., & Frigaard, P. (2011). Near-Shore Floating Wave Energy Converters: Applications for Coastal Protection. *Coastal Engineering Proceedings*, *1*(32), 61. https://doi.org/10.9753/icce.v32.structures.61

Rusu, E., & Onea, F. (2018). A review of the technologies for wave energy extraction, *2*(1), 10–19. https://doi.org/10.1093/ce/zky003

Rusu, E., Silva, D., & Soares, C. G. (2016). Evaluation of the shoreline dynamics in a coastal sector of the Portuguese nearshore. *Maritime Technology and Engineering*, (July), 1079–1086.

Rusu, E., & Soares, C. G. (2009). Numerical modelling to estimate the spatial distribution of the wave energy in the Portuguese nearshore. *Renewable Energy*, *34*(6), 1501–1516. https://doi.org/10.1016/j.renene.2008.10.027

Rusu, E., & Soares, C. G. (2013). Coastal impact induced by a Pelamis wave farm operating in the Portuguese nearshore. *Renewable Energy*, *58*, 34–49. https://doi.org/10.1016/j.renene.2013.03.001

Rusu, L., & Onea, F. (2017). The performance of some state-of-the-art wave energy converters in locations with the worldwide highest wave power. *Renewable and Sustainable Energy Reviews*, *75*(May), 1348–1362. https://doi.org/10.1016/j.rser.2016.11.123

Salter, S. H. (1974). Wave power. *Nature*, *249*, 720–724.

Sandberg, A. B., Klementsen, E., Muller, G., de Andres, A., & Maillet, J. (2016). Critical factors influencing viability ofwave energy converters in off-grid luxury resorts and small utilities. *Sustainability (Switzerland)*, *8*(12), 1–22. https://doi.org/10.3390/su8121274

Sarkar, D., Renzi, E., & Dias, F. (2014). Wave farm modelling of oscillating wave surge converters. In *Proceedings of the Royal Society A: Mathematical, Physical and Engineering Sciences* (pp. 470(2167), 20140118). Retrieved from http://dx.doi.org/10.1098/rspa.2014.0118

SI Ocean. (2014). Wave and Tidal Energy Market Deployment Strategy for Europe, Strategic Initiative for Ocean Energy, (June), 47. Retrieved from http://www.si-ocean.eu/en/Market-Deployment/Market-Deployment-Strategy/

Silva, D., Martinho, P., & Soares, C. G. (2018). Wave energy distribution along the Portuguese continental coast based on a thirty three years hindcast. *Renewable Energy*, *127*, 1064–1075. https://doi.org/10.1016/j.renene.2018.05.037

Silva, D., Rusu, E., & Soares, C. G. (2016). High-resolution wave energy assessment in shallow water accounting for tides. *Energies*, *9*(9). https://doi.org/10.3390/en9090761

Small, C., & Nicholls, R. J. (2003). A Global Analysis of Human Settlement in Coastal Zones. *Journal of Coastal Research*, *19*(3), 584–599.

Smith, H. C. M., Pearce, C., & Millar, D. L. (2012). Further analysis of change in nearshore wave climate due to an offshore wave farm: An enhanced case study for the Wave Hub site. *Renewable Energy*, *40*(1), 51–64. https://doi.org/10.1016/j.renene.2011.09.003

Soares, C. G., Bento, A. R., Gonçalves, M., Silva, D., & Martinho, P. (2014). Numerical evaluation of the wave energy resource along the Atlantic European coast. *Computers and Geosciences*, 1–13. https://doi.org/10.1016/j.cageo.2014.03.008

Sørensen, O. R., Kofoed-hansen, H., Rugbjerg, M., & Sørensen, L. S. (2004). A third-generation spectral wave model using an unstructured finite volume technique. *Coastal Engineering, 4*, 894–906.

Stewart, R. H. (2008). *Introduction to Physical Oceanography* (September). Department of Oceanography, Texas A&M University.

Stokes, C., & Conley, D. (2018). Modelling Offshore Wave farms for Coastal Process Impact Assessment: Waves, Beach Morphology, and Water Users. *Energies*, *11*(10), 2517. https://doi.org/10.3390/en11102517

Sverdrup, H. U., & Munk, W. H. (1946). Empirical and theoretical relations between wind, sea, and swell. *Eos, Transactions American Geophysical Union*, *27*(6), 823–827.

https://doi.org/10.1029/TR027i006p00823

SWAN, T. (2018). *Scientific and tehcnical documentation, SWAN Cycle III version 41.20AB*. Delft, The Netherlands. https://doi.org/10.1007/s13398-014-0173-7.2

Tay, Z. Y., & Venugopal, V. (2016). Optimization of Spacing for Oscillating Wave Surge Converter Arrays Using Genetic Algorithm. *Journal of Waterway, Port, Coastal, and Ocean Engineering*, *143*(2), 04016019-1–22.

Thanh, P. H. X., Grace, M. D., & James, S. C. (2008). *Sandia National Laboratories Environmental Fluid Dynamics Code: Sediment Transport User Manual*.

Thomas, T. J., & Dwarakish, G. S. (2015). Numerical Wave Modelling – A Review. *Aquatic Procedia*, *4*(Icwrcoe), 443–448. https://doi.org/10.1016/j.aqpro.2015.02.059

Tiron, R., Mallon, F., Dias, F., & Reynaud, E. G. (2015). The challenging life of wave energy devices at sea: A few points to consider. *Renewable and Sustainable Energy Reviews*, *43*, 1263–1272. https://doi.org/10.1016/j.rser.2014.11.105

Tolman, H. L. (1989). *The numerical model WAVEWATCH: a third generation model for hindcasting of wind waves on tides in shelf seas. Communications on hydraulic and geotechnical engineering* (Vol. 89–2).

Tolman, Hendrik L., & Chalikov, D. (1996). Source Terms in a Third-Generation Wind Wave Model. *Journal of Physical Oceanographyt*, *26*(11), 2497–2518. https://doi.org/10.1175/1520-0485(1996)026<2497:STIATG>2.0.CO;2

Uihlein, A., & Magagna, D. (2016). Wave and tidal current energy - A review of the current state of research beyond technology. *Renewable and Sustainable Energy Reviews*, *58*, 1070–1081. https://doi.org/10.1016/j.rser.2015.12.284

Venugopal, V., Nemalidinne, R., & Vögler, A. (2017). Numerical modelling of wave energy resources and assessment of wave energy extraction by large scale wave farms. *Ocean and Coastal Management*, *147*, 37–48. https://doi.org/10.1016/j.ocecoaman.2017.03.012

Vicinanza, D., Margheritini, L., Kofoed, J. P., & Buccino, M. (2012). The SSG wave energy converter: Performance, status and recent developments. *Energies*, *5*(2), 193–226. https://doi.org/10.3390/en5020193

Whittaker, T., Collier, D., Folley, M., Osterried, M., Henry, A., & Crowley, M. (2007). The development of Oyster–A shallow water surging wave energy converter. *Proceedings of the 7th European Wave and Tidal Energy Conference, EWTEC*, 11–14. Retrieved from http://www.aquamarinepower.com

Wilkinson, L., Whittaker, T. J. T., Thies, P. R., Day, A., & Ingram, D. (2017). The power-capture of a nearshore, modular, flap-type wave energy converter in regular waves. *Ocean Engineering*, *137*(January), 394–403. https://doi.org/10.1016/j.oceaneng.2017.04.016

Witt, M. J., Sheehan, E. V., Bearhop, S., Broderick, A. C., Conley, D. C., Cotterell, S. P., … Godley, B. J. (2012). Assessing wave energy effects on biodiversity: the Wave Hub experience. *Philosophical Transactions of the Royal Society*, *370*, 502–529. https://doi.org/10.1098/rsta.2011.0265

Wolgamot, H. A., Taylor, P. H., & Taylor, R. E. (2012). The interaction factor and directionality in wave energy arrays. *Ocean Engineering*, *47*, 65–73. https://doi.org/10.1016/j.oceaneng.2012.03.017

Zanuttigh, B., & Angelelli, E. (2013). Experimental investigation of floating wave energy converters for coastal protection purpose. *Coastal Engineering*, *80*, 148–159. https://doi.org/10.1016/j.coastaleng.2012.11.007